

Interacting Non-Hermitian Edge and Cluster Bursts on a Digital Quantum Processor

Jin Ming Koh ^{1,2} Wen-Tan Xue ³ Tommy Tai ⁴ Dax Enshan Koh ^{2,5,6} and Ching Hua Lee ^{3,*}

¹*Department of Physics, Harvard University, Cambridge, Massachusetts 02138, USA*

²*Quantum Innovation Centre (Q.InC), Agency for Science, Technology and Research (A*STAR),*

2 Fusionopolis Way, Innovis #08-03, Singapore 138634, Republic of Singapore

³*Department of Physics, National University of Singapore, Singapore 117542, Republic of Singapore*

⁴*Department of Physics, Massachusetts Institute of Technology, Cambridge, Massachusetts 02142, USA*

⁵*Institute of High Performance Computing (IHPC), Agency for Science, Technology and Research (A*STAR),*

1 Fusionopolis Way, #16-16 Connexis, Singapore 138632, Republic of Singapore

⁶*Science, Mathematics and Technology Cluster, Singapore University of Technology and Design,*

8 Somapah Road, Singapore 487372, Republic of Singapore

A lossy quantum system harboring the non-Hermitian skin effect can in certain conditions exhibit anomalously high loss at the boundaries of the system compared to the bulk, a phenomenon termed the non-Hermitian edge burst. We uncover interacting many-body extensions of the edge burst that are spatially extended and patterned, as well as cluster bursts that occur away from boundaries. Owing to the methodological difficulty and overhead of accurately realizing non-Hermitian dynamical evolution, much less tunable interactions, few experimental avenues in studying the single-particle edge burst have been reported to date and none for many-body variants. We overcome these roadblocks in this study, and present a realization of edge and cluster bursts in an interacting quantum ladder model on a superconducting quantum processor. We utilize a time-stepping algorithm, which implements time-evolution by non-Hermitian Hamiltonians by composing a linear combination of unitaries scheme and product formulae, to assess long-time behavior of the system. We observe signatures of the non-Hermitian edge burst on up to 64 unit cells, and detect the closing of the dissipative gap, a necessary condition for the edge burst, by probing the imaginary spectrum of the system. In suitable interacting regimes, we identify the emergence of spatial patterning and cluster bursts. Beyond establishing these generalized forms of edge burst phenomena, our study paves the way for digital quantum processors to be harnessed as a versatile platform for non-Hermitian condensed-matter physics.

I. INTRODUCTION

While closed quantum-mechanical systems conserve energy and are described by Hermitian Hamiltonians, open quantum systems lead to the possibility of non-Hermitian physical descriptions [1–4]. Such non-Hermitian systems typically feature effective gain or loss coupled to an external environment. Canonical examples of this broader category of quantum systems span lossy optics [5], quantum electrodynamics circuits [6], and electronic response in certain materials [7]. Amongst other applications, the properties endowed by non-Hermiticity have been harnessed to great effect in the engineering of ultra-sensitive sensors and detectors [8–10].

Indeed, non-Hermiticity enables unique physics with no Hermitian analog. A paradigmatic example is the emergence of the non-Hermitian skin effect (NHSE) [11–15], wherein a quantum system exhibits an asymmetric probability current flow in its bulk, an extensive number of eigenstates localized at a boundary, and profound differences in spectrum and dynamics dependent on boundary conditions—properties that are in contrast to conventional Hermitian systems. While the NHSE and generalizations [16–20] are well-studied, recent discoveries uncovered a new phenomenon labeled the non-Hermitian

edge burst [21–25] occurring in settings with dissipative (*i.e.* imaginary energy) gap closure. In non-Hermitian lossy quantum systems, the edge burst is characterized by anomalously high particle leakage near a boundary, supported by novel algebraic long-ranged decay of wavefunction amplitudes in the bulk. Beyond the canonical single-particle setting [26, 27], the interplay of the edge burst with interacting many-body physics is uncharted terrain in both theory and experiments.

Here, we report physical realizations of both single-body and novel many-body interacting generalizations of the edge burst on superconducting transmon-based quantum devices. We develop an efficient digital quantum simulation methodology for general non-Hermitian Hamiltonians, which leverages a linear combination of unitaries circuit construction technique in a time-stepping algorithm for dynamical evolution, and apply our method to probe a minimal quantum ladder system supporting the edge burst. Beyond observing signatures of the conventional single-body non-interacting edge burst on up to 64 unit cells, we show on quantum hardware that introducing sequences of density-density interactions lead to the formation of spatially extended and ordered (*i.e.* patterned) versions of the edge burst, and in certain regimes can also lead to bursts occurring in the bulk of the system far from boundaries, which we dub cluster bursts.

Our use of a quantum simulator enabled versatile accommodation of interactions of tunable strength and

* phylch@nus.edu.sg

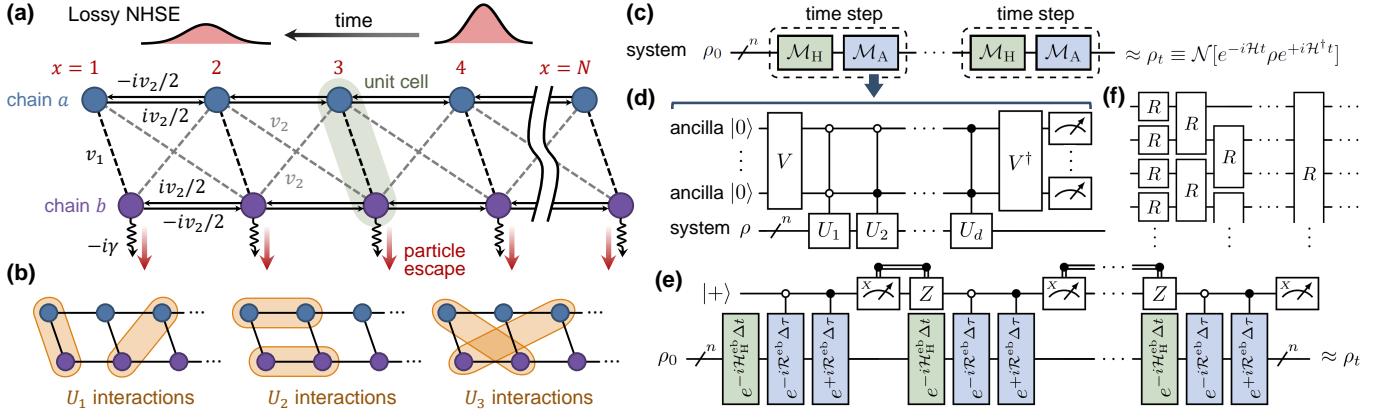


FIG. 1. **Non-Hermitian interacting quantum ladder model and quantum simulation methodology.** (a) Schematic of quantum ladder built from sublattice chains a and b , with reciprocal hopping v_1, v_2 between sites and on-site loss γ on the b chain. Leftward drift of a wavepacket is induced by the non-Hermitian skin effect (NHSE), accompanied by dampening of wavepacket amplitude by the non-Hermitian loss. (b) A sequence of range- r density-density interactions $\{U_r\}_r$ between sites on the ladder, giving rise to many-body effects enriching the non-Hermitian edge burst. (c) Structure of time-stepping quantum algorithm simulating time-evolution by a general non-Hermitian Hamiltonian on a quantum processor. The quantum maps \mathcal{M}_H and \mathcal{M}_A perform time-evolution by the Hermitian and anti-Hermitian parts of the Hamiltonian respectively. (d) The non-unitary \mathcal{M}_A is implemented through a linear combination of unitaries (LCU) circuit primitive, with the aid of a small ancillary register. (e) Structure of time-evolution circuits executed on the quantum processor. The LCU implementing \mathcal{M}_A superposes forward and backward time-evolution, coherently controlled by a single ancillary qubit that is re-used through mid-circuit qubit reset. Observables such as site-resolved occupancies are measured on the time-evolved state at the end of the circuit. (f) Time-evolution by Hermitian Hamiltonian components by trotterization. The R gates denote varying multi-qubit Pauli rotations.

range in a model hosting multiple particles, an important advantage over alternative effectively single-body platforms such as waveguide photonics [28] and analog circuits [29]. While quantum processors are increasingly utilized for quantum dynamics [30–36] and various areas of (Hermitian) condensed-matter applications [37–45], their use in studying non-Hermitian physics has remained nascent owing to difficulties in scalably realizing non-Hermitian time-evolution on near-term noisy intermediate-scale quantum (NISQ) devices of the present. Demonstrations to-date are restricted to small system sizes or rely on resource intensive protocols [46–51]. In addition to unveiling novel forms of the edge burst induced by interactions, the methods we develop in this work, which do not require expensive classical pre-processing of Hamiltonian matrices nor large numbers of intermediary measurements or variational iterations, bring us significantly closer to meaningfully utilizing quantum processors as a platform for studying generic non-Hermitian systems.

II. RESULTS

A. Minimal interacting non-Hermitian quantum ladder

While the quantum simulation methods we utilize are general, we focus on investigating the phenomenology of the non-Hermitian edge burst in the present work. To set

a clear physical picture, we first establish the theoretical setting underlying our study. The model we investigate is built atop a minimal bosonic one-dimensional quantum ladder exhibiting the edge burst [21], characterized by a two-band Bloch Hamiltonian

$$\mathcal{H}_0^{\text{eb}}(k) = (v_1 + v_2 \cos k) \sigma^x + \left(v_2 \sin k + \frac{i\gamma}{2} \right) \sigma^z - \frac{i\gamma}{2} \mathbb{I}, \quad (1)$$

where $v_1, v_2 \geq 0$ are tight-binding hopping coefficients, $\gamma > 0$ is an on-site loss rate and is responsible for the non-Hermiticity of the system, and σ^x, σ^z are Pauli operators acting on two pseudospin degrees of freedom which we associate with a and b sublattices within a unit cell.

We illustrate $\mathcal{H}_0^{\text{eb}}$, which is interpretable as a lossy quantum walk Hamiltonian, in real space in Figure 1a. The γ loss corresponds physically to leakage or escape [21] of the quantum walker into the environment. As long as $v_1 \neq 0$, the $\pi/2$ fluxes in the triangles between the a - and b -sublattice chains generate rotational motion such that they favor opposing directions of travel along the ladder; but the γ loss on b sublattices dampens dynamics on that chain, thereby producing a preferential leftward chiral motion (in the $-\hat{x}$ direction). This mechanism gives rise to the NHSE along the ladder, which localizes an extensive number of bulk-band eigenstates on the left boundary ($x = 1$) of the system. Alternatively, the NHSE can be understood as a consequence of an equivalence [21, 25] of $\mathcal{H}_0^{\text{eb}}$ to the non-Hermitian

Su-Schrieffer-Heeger (SSH) model with asymmetric left-right particle hoppings [11].

Here, we extend the edge burst phenomenon from the canonical non-interacting single-particle context to a many-body interacting setting. In addition to $\mathcal{H}_0^{\text{eb}}$, we consider also a natural sequence of density-density interactions (see Figure 1b). In real space over N unit cells, the model we examine is $\mathcal{H}^{\text{eb}} = \mathcal{H}_0^{\text{eb}} + \mathcal{H}_{\text{int}}^{\text{eb}}$, where

$$\mathcal{H}_{\text{int}}^{\text{eb}} = \sum_{r \geq 1} U_r \sum_{z=1}^{2N} n_z n_{z+r}, \quad (2)$$

where $U_r \in \mathbb{R}$ are range- r interaction strengths and n_z is the number operator on site z on the flattened ladder, that is, $n_z = n_{x\ell} = c_{x\ell}^\dagger c_{x\ell}$ for flattened index $z = 2x - \delta_{\ell a}$ and particle operator $c_{x\ell}$ acting on unit cell $x \in [N]$ and sublattice $\ell \in \{a, b\}$. Physically, U_r introduces an interaction potential dependent on the occupation of sites on the ladder separated by distance r . We consider hardcore bosons on the ladder, which emerge in a regime of strong on-site repulsive interactions on top of $\mathcal{H}_{\text{int}}^{\text{eb}}$ (see Methods).

The Schrödinger equation $i(d/dt)\omega_t = [\mathcal{H}^{\text{eb}}, \omega_t]$ prescribes that from an initial normalized quantum state (density matrix) ω_0 of the ladder, the state at time t is given by $\omega_t = V_t^{\text{eb}} \omega_0 (V_t^{\text{eb}})^\dagger$ where $V_t^{\text{eb}} = \exp(-i\mathcal{H}^{\text{eb}}t)$ is the time-evolution propagator. As \mathcal{H}^{eb} is non-Hermitian, the propagator V_t^{eb} is non-unitary and state normalization is not generically preserved. In particular, the quantum state norm decays as

$$\frac{d}{dt} \text{tr}(\omega_t) = i \left\langle \mathcal{H}^{\text{eb}\dagger} - \mathcal{H}^{\text{eb}} \right\rangle_{\omega_t} = -2\gamma \sum_{x=1}^N \langle n_{xb} \rangle_{\omega_t} \leq 0. \quad (3)$$

The norm of the quantum state describes the probability of the walker (*i.e.* boson) remaining on the ladder. Accordingly, the escape probability of the walker at unit cell x by time t is given by the time integral

$$P_x(t) = 2\gamma \int_0^t \langle n_{xb} \rangle_{\omega_\tau} d\tau, \quad (4)$$

and the final cell-resolved escape probabilities are given by the long-time limit $\mathcal{P}_x = \lim_{t \rightarrow \infty} P_x(t)$. Restricted to pure single-particle quantum states, Eqs. (3) and (4) reduce to be consistent with expressions in Ref. [21].

Our central quantities of interest are the final escape probabilities \mathcal{P}_x which enable direct probing of the presence and properties of the non-Hermitian edge burst. Accordingly, we seek to measure the site-resolved occupancy densities $\langle n_{x\ell} \rangle_{\omega_t}$ in our realizations, from which the escape probabilities $P_x(t)$ and \mathcal{P}_x can be recovered.

B. Realizing non-Hermitian quantum dynamics on quantum hardware

Any attempt to realize time-evolution under a (arbitrary) non-Hermitian Hamiltonian \mathcal{H} on a quantum

platform runs invariably into a problem—that quantum states on a quantum device are by nature normalized, whereas \mathcal{H} generates evolution that does not preserve normalization. Our approach is to realize the normalized evolution

$$\rho_t = \frac{V_t \rho_0 V_t^\dagger}{\text{tr}(V_t \rho_0 V_t^\dagger)}, \quad \rho_0 = \omega_0, \quad (5)$$

where $V_t = e^{-i\mathcal{H}t}$ is the (non-unitary) time-evolution propagator over time t . Then the non-normalized physical state ω_t and ρ_t are related by the rescaling $\omega_t = A_t^2 \rho_t$ for $A_t^2 = \text{tr}(\omega_t)$, and accordingly $\langle O \rangle_{\omega_t} = A_t^2 \langle O \rangle_{\rho_t}$ for any observable O . Thus, in addition to implementing the normalized time-evolution, we develop a method to recover the normalization factor A_t from measurements.

We employ a time-stepping algorithm to perform time-evolution from ρ_0 to ρ_t (see Figure 1c) that splits the evolution into m steps, each approximately realizing time-evolution over an interval $\Delta t = t/m$ to an error $\mathcal{O}(\Delta t^2)$. Thus, the error accumulated over all steps scales as $\mathcal{O}(1/m)$ and arbitrarily high simulation precision can be reached by increasing m . Writing $\mathcal{H} = \mathcal{H}_H - i\mathcal{H}_A$ where \mathcal{H}_H and $-i\mathcal{H}_A$ are the Hermitian and anti-Hermitian parts of \mathcal{H} respectively, each time step comprises the quantum maps \mathcal{M}_H and \mathcal{M}_A in sequence, designed to perform normalized time-evolution on arbitrary incident states by \mathcal{H}_H and $-i\mathcal{H}_A$ respectively over time Δt to error $\mathcal{O}(\Delta t^2)$.

The unitary channel \mathcal{M}_H can be implemented by standard methods. In the present work we use the first-order Trotter-Lie product formula [52], which rewrites \mathcal{H}_H in the Pauli basis and performs time-evolution through a sequence of multi-qubit Pauli rotations (see Figure 1f). In general, higher-order product formulae or alternative unitary time-evolution circuit construction methods [53, 54] can also be used. More details on the implementation of trotterized circuits on hardware are given in Methods.

In contrast the map \mathcal{M}_A , realizing action $\rho \mapsto V_{\Delta t}^A \rho V_{\Delta t}^{A\dagger} + \mathcal{O}(\Delta t^2)$ up to normalization for time-evolution propagator $V_{\Delta t}^A = e^{-\mathcal{H}_A \Delta t}$ and arbitrary incident states ρ , is non-unitary and is a source of difficulty. To perform \mathcal{M}_A , we make use of the linear combination of unitaries (LCU) circuit primitive, which enables an effective action defined by sums of unitaries rather than products on a system register. In general, to effect an action $(\mu_1 U_1 + \dots + \mu_d U_d)$ for coefficients $\{\mu_k > 0\}_k$ and unitaries $\{U_k\}_k$ up to normalization, a register of $\lceil \log_2 d \rceil$ ancillary qubits and the ability to perform U_k coherently controlled by the $|k\rangle$ state of the ancillary register suffice (see Figure 1d). For our purpose, we approximate $V_{\Delta t}^A$ by a linear combination of forward and backward unitary time-evolution to error $\mathcal{O}(\Delta t^2)$. In fact, in general, for any $d \geq 2$, applicable mixtures of time-evolution operations can be efficiently found through power series expansions in Δt , and solutions of higher order error are available (see Methods).

To minimize the hardware resources required, we used

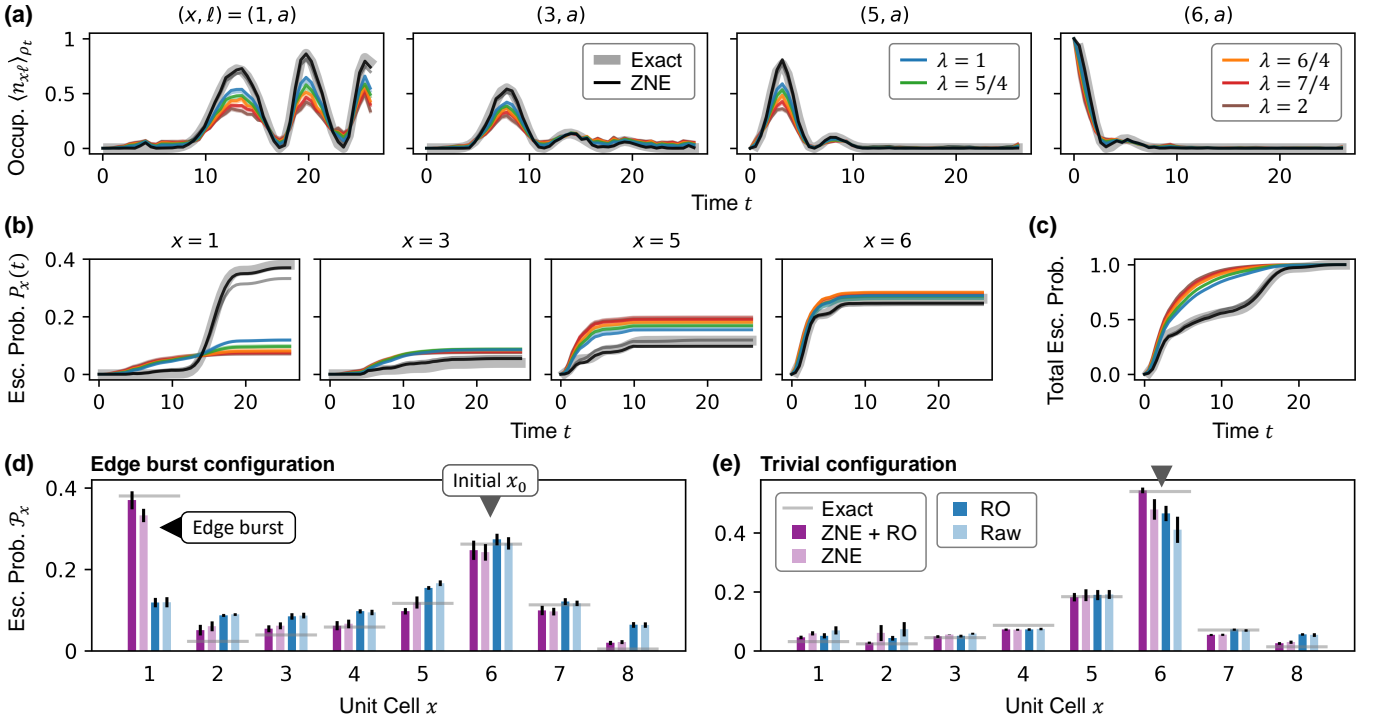


FIG. 2. **Observing signatures of the non-Hermitian edge burst on a quantum processor.** (a) Site-resolved occupancy densities after normalized time-evolution on a 8-unit cell quantum ladder, comparing data measured on quantum hardware at various noise amplification factors λ , after post-processing with zero-noise extrapolation (ZNE), and exact numerics. Solid thin lines are with readout error mitigation (RO) applied; translucent thin lines behind are without. To avoid clutter, only the a sublattice of unit cells $x \in \{1, 3, 5, 6\}$ are shown. (b) Unit-cell-resolved escape probabilities $P_x(t)$ obtained from the data in (a). Time-integration of the occupancy densities first recovers proper wavefunction norm, and a second time-integration produces $P_x(t)$. (c) Total escape probability $P(t)$ summed over all unit cells, which approaches unity as time progresses. (d) Final unit-cell-resolved escape probabilities \mathcal{P}_x in the long-time limit. Data obtained on quantum hardware with and without ZNE and RO, and from exact numerics, are shown. In a parameter regime supporting the edge burst, anomalously high escape probability on the $x = 1$ edge of the ladder is detected; whereas in the trivial regime escape probability is concentrated only near the initial location of the particle (at $x_0 = 6$). Error bars are standard deviations across 8 experiment runs. See Supplementary Tables S2 and S3 for Hamiltonian parameter values and superconducting quantum devices used.

$d = 2$ which necessitated only a single ancillary qubit. The pair of forward and backward time-evolution slices in the LCU are then defined by $\mu_+ = \mu_-$ and $U_{\pm} = e^{\pm i\mathcal{R}\Delta\tau}$, for a rescaled time step $\Delta\tau = \sqrt{2}\Delta t$ and an auxiliary Hermitian Hamiltonian satisfying $\mathcal{R}^2 = \mathcal{H}_A$. In the present edge burst setting, while choices of \mathcal{R}^{eb} satisfying $(\mathcal{R}^{\text{eb}})^2 = \mathcal{H}_A^{\text{eb}}$ are readily found, further leveraging the structure of $\mathcal{H}_A^{\text{eb}}$ allowed refinements to \mathcal{R}^{eb} such that the LCU achieves the $V_{\Delta t}^A$ time-evolution exactly instead of to $\mathcal{O}(\Delta t^2)$ error (see Methods). We implemented the U_{\pm} unitary time-evolution slices via first-order trotterization, with a low-overhead scheme in effecting the coherent controls by the ancillary qubit (see Methods).

The structure of the overall circuit we executed in experiments is shown in Figure 1e. Through mid-circuit qubit reset, we re-initialized the ancillary qubit used for the LCU primitive between time steps—thus a single ancilla sufficed for the entire evolution from ρ_0 to ρ_t . Unlike other methods that can be adapted for non-Hermitian dynamical evolution [55–58], this protocol does not assume an ansatz for the time-evolved state, nor does it require

iterative variational optimization or step-wise circuit construction based on intermediate measurements, which are often large in number. In Methods, we provide a generalized description of the time-stepping quantum simulation procedure outlined here. For cases where \mathcal{R}_A is difficult to obtain, we describe also a method based on a similar LCU expansion but requiring only access to terms in \mathcal{H}_A .

Upon completion of evolution to ρ_t , we simultaneously measured site-resolved occupancies $\langle n_{x\ell} \rangle_{\rho_t}$ for all unit cells $x \in [N]$ and sublattices $\ell \in \{a, b\}$ on the quantum ladder. We then recovered the quantum state normalization factor A_t via Eq. (3) as the time integral

$$A_t = \exp\left(-\gamma \int_0^t \sum_{x=1}^N \langle n_{xb} \rangle_{\rho_{\tau}} d\tau\right), \quad (6)$$

which then enabled the rescaling of the measured $\langle n_{x\ell} \rangle_{\rho_t}$ to $\langle n_{x\ell} \rangle_{\omega_t}$. Lastly, a second time integration produces the escape probabilities $P_x(t)$ as in Eq. (4). We run experiments to large times t to access the long-time escape behavior \mathcal{P}_x (see Methods).

We utilized IBM superconducting quantum processors in our experiments, which host up to 133 transmon qubits connected in a heavy-hexagon topology with decoherence times T_1, T_2 up to $\sim 200 \mu\text{s}$. These devices support mid-circuit qubit readout used in our quantum circuits. Further details on the quantum hardware are provided in [Methods](#), and device specifications such as gate and readout error rates are summarized in Supplementary Table S4. To address noise, which is non-negligible on present-day quantum hardware, we integrate several error suppression and mitigation methods such as dynamical decoupling, zero noise extrapolation with randomized gate twirling, and readout error mitigation (see [Methods](#)).

C. Observing signatures of the non-Hermitian edge burst

To start, we realized the non-Hermitian quantum ladder \mathcal{H}^{eb} with $N = 8$ unit cells without interactions ($U_r = 0$ uniformly) and with open boundary conditions—natural on an open chain of qubits on the quantum processor—such that the ladder terminated in spatial boundaries past $x = 1$ and $x = 8$. The ladder is initialized with a particle on the a -sublattice of the $x = 6$ unit cell. We constructed our time-evolution circuits via trotterization as described earlier with standard transpilation onto hardware (see [Methods](#)), without employing more sophisticated circuit optimization techniques.

We present a breakdown of experiment results in [Figure 2](#), illustrating the major steps in the measurement and data processing pipeline in addition to the final results. First, we show in [Figure 2a](#) site-resolved occupancy densities $\langle n_{x\ell} \rangle_{\rho_t}$ on the normalized time-evolved quantum state ρ_t as measured on the hardware. These occupancy densities were acquired at several noise amplification factors $\lambda \geq 1$, where $\lambda = 1$ corresponds to the circuits without modification and $\lambda > 1$ are on folded circuits of artificially increased gate count and depth (see [Methods](#)) but achieving, in the absence of noise, the same evolution. The increased circuit size amplifies noise suffered during time-evolution, arising from gate errors that are averaged by randomized gate twirling (see [Methods](#)) and decoherence of the qubits over time. The impact of the amplified noise is clear in the measured data: at higher λ , the amplitude of oscillations in $\langle n_{x\ell} \rangle_{\rho_t}$ are suppressed and small-scale fluctuations become more prominent.

Employing a form of zero noise extrapolation (ZNE), we regressed the acquired data into the $\lambda = 0$ noiseless limit, taking into account physicality constraints such as particle number conservation and non-negativity of occupancy densities. As evident in [Figure 2a](#), the $\langle n_{x\ell} \rangle_{\rho_t}$ data after ZNE closely matched theoretical expectations calculated via exact diagonalization (ED) and presented a marked improvement over the $\lambda = 1$ data before ZNE. In addition to ZNE, we also employed readout error miti-

gation (RO), which approximately corrects bit-flip errors in measurement outcomes on the quantum processor (see [Methods](#)). Results without RO are inferior in accuracy and are shown in [Figure 2a](#) as translucent lines.

By performing time-integration on the $\langle n_{x\ell} \rangle_{\rho_t}$ data, as described in [Eq. \(6\)](#), we recovered the normalization factor of the quantum state and thereby rescaled $\langle n_{x\ell} \rangle_{\rho_t}$ into occupancy densities $\langle n_{x\ell} \rangle_{\omega_t}$ on the physical state ω_t , the norm of which decreases over time (as \mathcal{H}^{eb} is lossy). A second time-integration on $\langle n_{x\ell} \rangle_{\omega_t}$ yielded the escape probabilities $P_x(t)$ on unit cells x . We present these cell-resolved $P_x(t)$ in [Figure 2b](#). The short-time increase of $P_x(t)$ at $x = 6$ expectedly arises from the initial localization of the particle on that unit cell, but as time progresses and the particle diffuses asymmetrically leftward under the NHSE, accumulation of $P_x(t)$ at cells of smaller x occurs. We observe the impact of ZNE on the accuracy of the data, which brought the experiment $P_x(t)$ into close agreement with ED predictions. In [Figure 2c](#), we report the total escape probability summed over all cells of the ladder, $P(t) = \sum_{x=1}^N P_x(t)$, which monotonically approached unity; the experiment was terminated when $P(t)$ reached sufficiently close to unity.

Finally in [Figure 2d](#) we present cell-resolved final escape probabilities \mathcal{P}_x along the ladder, showing raw experiment data, data with RO only, with ZNE only, and with both ZNE and RO applied. We had tuned \mathcal{H}^{eb} to be in a regime supporting the edge burst, here clearly manifesting as a prominent spike in \mathcal{P}_x at the $x = 1$ boundary—larger, in fact, than at the $x_0 = 6$ initial localization of the particle. These results highlight the relevance of error mitigation: the signature of the edge burst is washed out without ZNE and RO, whereas with mitigation the escape probabilities closely agree with theory. Indeed, we emphasize the inherent sensitivity of the experimental measurements of \mathcal{P}_x : small inaccuracies in the $\langle n_{x\ell} \rangle_{\rho_t}$ data, such as the suppressed oscillations in [Figure 2a](#), can accumulate over the time-integration into large deviations in $P_x(t)$ and \mathcal{P}_x at long times. This sensitivity places considerable demand on the robustness of the quantum simulation methodology and hardware, and underscores the difficulty of all experiments in our study.

In [Figure 2e](#) we report the counterpart of [Figure 2d](#) on \mathcal{H}^{eb} in the trivial regime, which does not exhibit the edge burst. The only peak in \mathcal{P}_x occurs at the initial location of the particle, reflecting the decay of the particle in-situ with no physically significant dynamics over time.

We describe additional experiments on the same $N = 8$ ladder but with initial particle localization at $x_0 = 4$, and on a smaller $N = 4$ ladder, in [Supplementary Note 4A](#). The conclusions from those results are qualitatively identical to those drawn here, and the real-space signature of the edge burst in \mathcal{P}_x were likewise clearly observed.

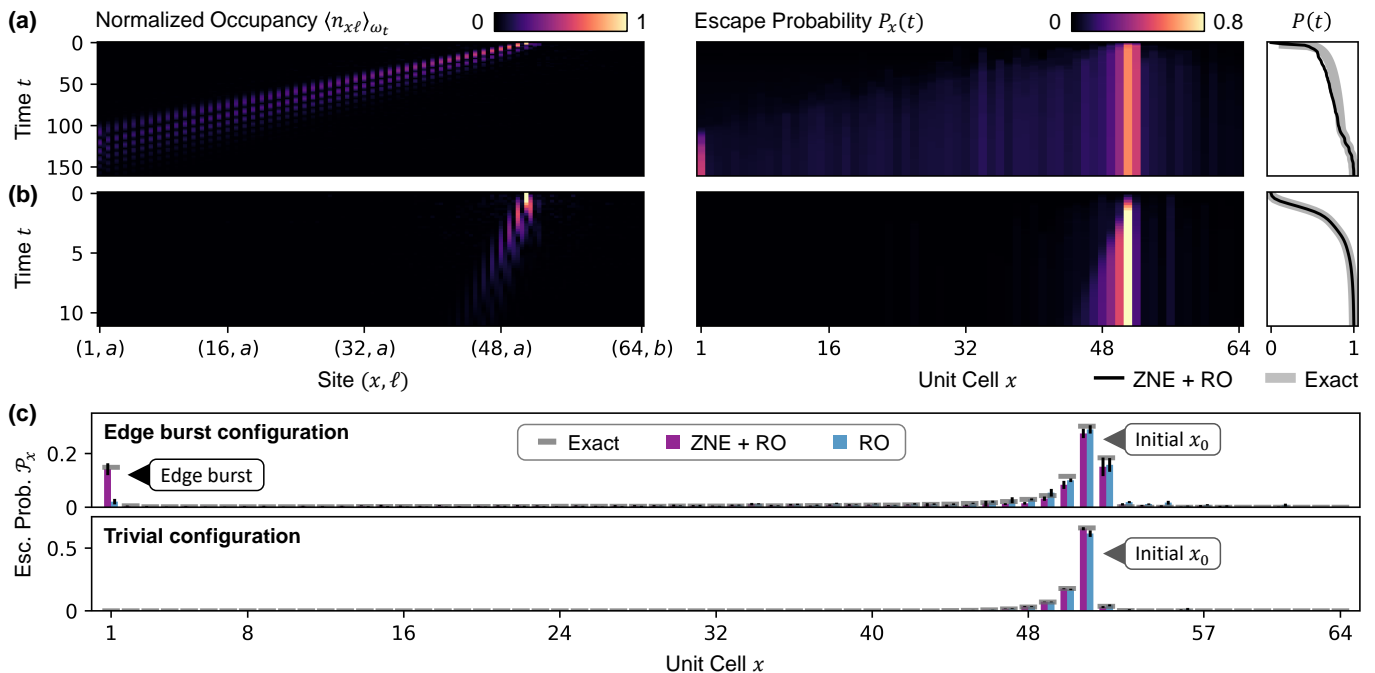


FIG. 3. **Physical demonstration of edge burst at large system size.** (a) Site-resolved occupancy densities and unit-cell-resolved escape probabilities $P_x(t)$ over time on a 64-unit cell quantum ladder in the edge burst regime measured on quantum hardware, with zero-noise extrapolation (ZNE) and readout error mitigation (RO) applied. The particle was initially localized at $x_0 = 51$. Proper quantum state normalization was recovered via time-integration of measured occupancy densities and applied to both panels. The total escape probability $P(t)$ approaches unity as time progresses. (b) Same as (a) but in the trivial regime. (c) Final unit-cell-resolved escape probabilities \mathcal{P}_x in the long-time limit, comparing results in the edge burst regime and in the trivial regime. Data obtained on quantum hardware with ZNE and RO applied, RO only, and exact numerics are shown. Error bars are standard deviations across 16 experiment runs. See Supplementary Tables S2 and S3 for Hamiltonian parameter values and superconducting quantum devices used.

D. Edge burst on larger system sizes

We next investigated larger system sizes. Aside from demonstrating the versatility of our quantum simulation approach, experiments on larger ladders also minimize finite-size effects and produce clearer evidence of the non-Hermitian edge burst. Here we realize an $N = 64$ unit cell (128-site) ladder, which is 8 times the system size examined in the previous section.

At such large system sizes, trotterization and standard circuit transpilation produce circuits far too deep for present NISQ hardware to feasibly accommodate—naïve execution of these circuits would result in near-complete decoherence of the quantum state and vanishing signal-to-noise ratios when measuring observables. To overcome this present limitation, we employed an additional tensor-network aided circuit recompilation technique [43–45, 56] for circuit compression, which replaces components of the circuits with approximate lower-depth parametrized ansatzes that are variationally optimized (see Methods). In this process, we exploited symmetries of \mathcal{H}^{eb} , such as number conservation, to enhance circuit construction performance and quality.

In the left panel of Figure 3a, we report site-resolved occupancy densities $\langle n_{x\ell} \rangle_{\omega_t}$ on the $N = 64$ ladder in

the edge burst regime, as obtained on hardware with ZNE and RO error mitigation applied. Underlying this data were $\langle n_{x\ell} \rangle_{\rho_t}$ measurements that had been time-integrated. As \mathcal{H}^{eb} is lossy, the occupancy densities $\langle n_{x\ell} \rangle_{\omega_t}$ decay with time, reflecting particle escape from the ladder. In the right panel we report the cell-resolved escape probabilities $P_x(t)$ time-integrated from $\langle n_{x\ell} \rangle_{\omega_t}$.

For comparison, we show in Figure 3b the counterpart to Figure 3a for \mathcal{H}^{eb} in the trivial regime. In both setups, asymmetrical leftwards drift of the particle along the ladder driven by the NHSE is clearly observed; but in the edge burst regime the decay of the particle is significantly slower, allowing the particle to reach the $x = 1$ boundary with non-negligible amplitude (*i.e.* survival probability). Both experiments were terminated when the total escape probability $P(t)$ reached close to unity.

Finally, we present the final escape probabilities \mathcal{P}_x in Figure 3c for both regimes. As before, the edge burst manifests as a prominent spike in escape probability at the $x = 1$ boundary, which is absent in the trivial regime. This demanding setting at large system size reinforces the relevance of a robust quantum simulation methodology integrated with effective error mitigation: the experimental \mathcal{P}_x data closely agrees with theory with mitigation fully employed.

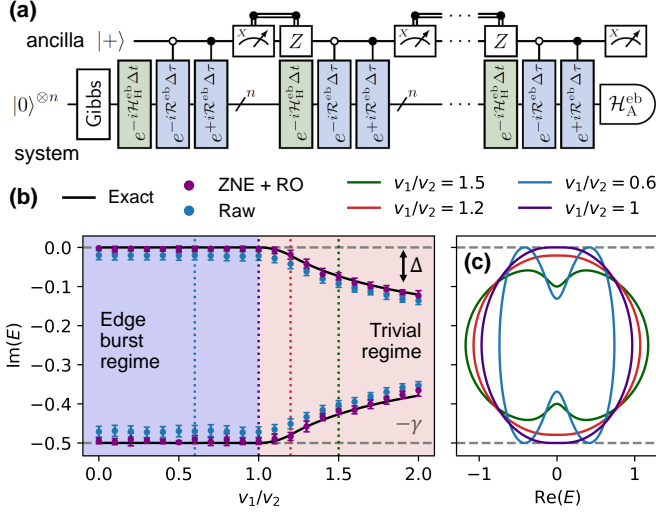


FIG. 4. **Probing spectral properties of the edge burst system.** (a) Schematic of the circuits used to measure extremal imaginary energy. The system is prepared in a Gibbs state and time-evolved under the non-Hermitian \mathcal{H}^{eb} for long times. The expectation value of the anti-Hermitian component of the Hamiltonian $-i\mathcal{H}_A^{\text{eb}}$ is measured on the time-evolved state. (b) Maximum and minimum imaginary energy versus hopping amplitudes v_1/v_2 , showing hardware data measured on an $N = 16$ quantum ladder with and without ZNE and RO, and exact numerics. The $v_1/v_2 \leq 1$ regime, wherein the dissipative gap Δ closes, supports the edge burst; the $v_1 > v_2$ regime is trivial. Error bars are standard deviations across 25 experiment runs. See Supplementary Tables S2 and S3 for Hamiltonian parameter values and superconducting quantum devices used. (c) Complex energy spectra of \mathcal{H}^{eb} along indicated values of v_1/v_2 from numerics. The maxima and minima of these spectra are traced in (b). The horizontal and vertical reflection symmetries of the spectra are protected by symmetries of the Hamiltonian.

E. Spectral information of the edge burst

Time-evolution on the non-Hermitian quantum ladder Hamiltonian \mathcal{H}^{eb} comprises conceptually of two intermixed components—real time-evolution on the Hermitian part of the Hamiltonian $\mathcal{H}_H^{\text{eb}}$ and imaginary time-evolution on $\mathcal{H}_A^{\text{eb}}$. Unlike real-time evolution, imaginary time-evolution on a Hermitian Hamiltonian is not energy-conserving and, in fact, yields quantum states of extremal energy at long times. Thus, by evolving to long times under \mathcal{H}^{eb} , we can purify a starting state into an eigenstate of extremal imaginary eigenenergy.

An illustration of this type of quantum circuits we executed is shown in Figure 4a. To ensure nonzero overlap with the extremal eigenstates, we initiated time-evolution with the infinite-temperature Gibbs state (*i.e.* maximally mixed state). This is prepared through a completely depolarizing channel implemented in constant depth through a single round of mid-circuit measure-

ments whose outcomes are discarded (see Methods). The time-evolution quantum algorithm for non-Hermitian Hamiltonians, as described earlier (drawn in Figure 1c), is invoked following state preparation. After evolution for a sufficiently long time, we measured the imaginary energy of the quantum state through Hamiltonian averaging on $\mathcal{H}_A^{\text{eb}}$ (see Methods).

We report the extremal imaginary eigenenergies $\text{Im } E$ measured on hardware as a function of hopping amplitudes v_1/v_2 in Figure 4b. Of particular relevance is the largest imaginary eigenenergy $\max \text{Im } E$, which is zero for $v_1 \leq v_2$ but strictly negative for $v_1 > v_2$. That is, the imaginary gap $\Delta = -\max \text{Im } E$, also known as the dissipative gap, of \mathcal{H}^{eb} closes for $v_1 \leq v_2$. In Figure 4c we illustrate the complex energy spectrum of \mathcal{H}^{eb} at various v_1/v_2 , which makes clear the recession of the spectrum into the negative imaginary half-plane as v_1 exceeds v_2 . We remark that the horizontal and vertical reflection symmetries of the complex spectra, about $\text{Re } E = 0$ and $\text{Im } E = -\gamma/2$, are consequent of chiral and time-reversal symmetries of the quantum ladder model (see Supplementary Note 1A).

Prior theoretical analysis [21] indicated that the closing of the dissipative gap Δ is a necessary condition for the edge burst to occur in addition to the presence of the NHSE. Intuitively, the zero imaginary eigenenergy modes suffer no decay during time-evolution and are long-lived, thus enabling an initial wavepacket driven by the NHSE to reach the boundary of the system. The particle is then trapped against the boundary by the NHSE and decays, giving rise to the edge burst. In contrast, upon opening of the dissipative gap, any wavepacket suffers exponential loss during propagation and cannot reach the boundary before decay. This qualitative difference was clearly observed, for example, in our experiment results in Figure 3. Indeed, in all our experiments the edge burst regime—where edge burst signatures are present—occur when $v_1 \leq v_2$, and the trivial regimes occur when $v_1 > v_2$.

F. Spatially extended and ordered edge bursts with multiple interacting particles

We now turn to our key set of results: novel edge burst phenomena observed with multiple interacting particles. Systems hosting strongly interacting quantum particles are difficult to realize on classical or effectively single-body quantum simulators, such as electrical (*i.e.* topolectrical) circuits [29, 59–61] or waveguide photonic systems [28, 62, 63], that have thus far been used to study non-Hermitian physics—let alone achieving tunability of interaction strengths, ranges and types. In this respect digital quantum simulation on quantum hardware, making use of the full many-body Hilbert space hosted by the device and programmable quantum operations in that space, presents a clear versatility advantage. The quantum simulation approach we developed accommodates arbitrary interactions in the Hamiltonian (see Meth-

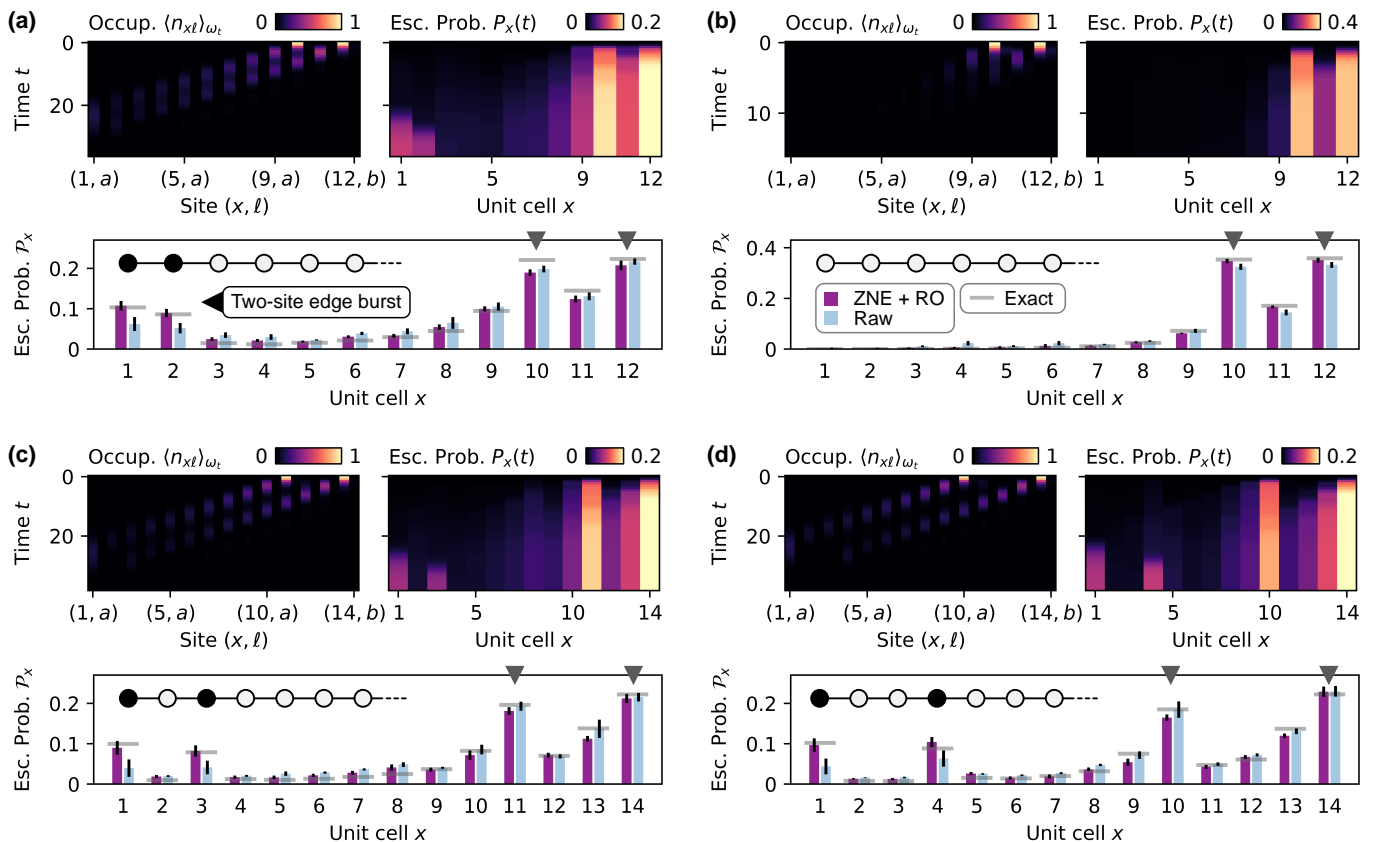


FIG. 5. **Spatially extended edge bursts with multiple interacting particles.** (a) Site-resolved occupancy densities and unit-cell-resolved escape probabilities $P_x(t)$ measured on a 12-unit cell quantum ladder in the edge burst regime hosting two interacting particles. Final escape probabilities \mathcal{P}_x obtained on hardware with and without zero-noise extrapolation (ZNE) and readout error mitigation (RO), and exact numerics, are shown. An edge burst spatially extended across two unit cells is observed, highlighted as black shading in the cartoon inset. (b) Same as (a) but in the trivial regime, which does not give rise to an edge burst. (c)–(d) By increasing the range of interactions on the quantum ladder, spatially extended edge bursts separated by one or more unit cells arise. Gray arrows denote the initial localization of the particles. Error bars are standard deviations across 10 experiment runs. See Supplementary Tables S2 and S3 for Hamiltonian parameter values and superconducting quantum devices used.

ods), and here we exploit this versatility to explore non-Hermitian edge burst phenomenology enriched by interactions.

To start, we examined two particles (hardcore bosons) on an $N = 12$ ladder in the edge burst regime with $U_1 > 0$ interactions switched on—that is, repulsive density-density interactions acting between sites on the ladder a range $r = 1$ apart (see Figure 1b for illustration). The energy scale of the interaction was comparable to those of the non-interacting parts of the Hamiltonian (hoppings v_1, v_2 and loss γ). We present experiment results in Figure 5a, showing the measured site-resolved occupancy densities $\langle n_{x\ell} \rangle_{\omega_t}$, recovered cell-resolved escape probabilities $P_x(t)$, and final escape probabilities \mathcal{P}_x . As in our prior experiment on the vanilla edge burst at large system size, we employed circuit recompilation to compress circuit depth and utilized ZNE and RO error mitigation to address hardware noise.

Here, interestingly, from \mathcal{P}_x we observe the manifes-

tation of a spatially extended version of the edge burst, spanning two unit cells ($x \in \{1, 2\}$) instead of the typical single unit cell in vanilla edge bursts. The mechanism underlying this spatial extension stems from a Pauli exclusion-like effect arising from the interactions. At short times both particles expectedly diffuse to the left under the NHSE, but as the first impacts on the $x = 1$ boundary, the hardcore nature of the bosons and the U_1 interactions inhibit the second from also occupying the first unit cell—effectively, the second boson encounters a virtual boundary at $x = 2$. This is akin to the formation of the so-called Fermi skin in fermionic non-Hermitian systems [64, 65], wherein fermions are pushed up against a boundary by the NHSE and thereby exhibit a Fermi surface in real-space. Here, the second boson is trapped at the $x = 2$ unit cell and decays, giving rise to a spatially extended edge burst occurring over two unit cells. In the trivial regime the edge burst does not manifest, as shown in Figure 5b.

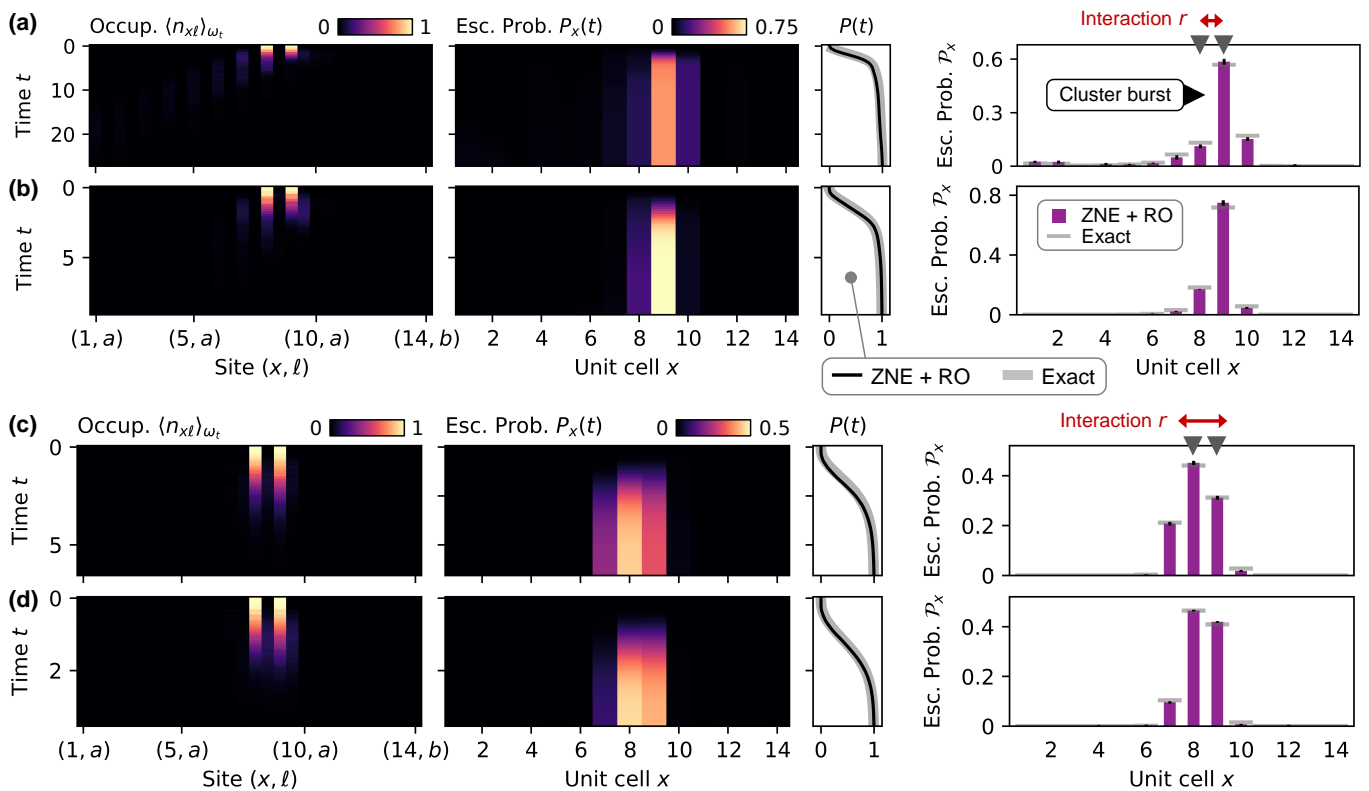


FIG. 6. **Cluster bursts away from boundaries induced by interactions.** (a) Site-resolved occupancy densities, unit-cell-resolved escape probabilities $P_x(t)$, and total escape probability $P(t)$ summed over all unit cells, measured on a 14-unit cell quantum ladder in the edge burst regime hosting two interacting particles. Final escape probabilities \mathcal{P}_x obtained on hardware with zero-noise extrapolation (ZNE) and readout error mitigation (RO), and exact numerics, are shown. Initial localizations of the two particles (gray triangles) are barely outside the range of interactions (red arrow). (b) Same as (a) but with the quantum ladder in the trivial regime. (c)–(d) Measurements on the same quantum ladder as (a)–(b) but with the initial localizations of the particles (gray triangles) inside the range of interactions (red arrow), with the ladder in (c) the edge burst regime and (d) the trivial regime. In all cases, a cluster burst is observed in the vicinity of the initial locations of the particles, far from boundaries. Error bars are standard deviations across 10 experiment runs. See Supplementary Tables S2 and S3 for Hamiltonian parameter values and superconducting quantum devices used.

Moreover, we observed that by tuning the range of interactions, spatially “ordered” manifestations of the edge burst can arise. In Figure 5c we present experiment results on an $N = 14$ ladder hosting two bosons with $U_r > 0$ switched on for $r \leq 3$, and in Figure 5d we present results with $U_r > 0$ for $r \leq 5$. In the former we witness a spatially extended edge burst occupying alternate unit cells, and in the latter the edge burst is separated by two unit cells of small escape probability. The cartoon insets in Figures 5c and 5d highlight these patterns. In analogy to spatial ordering induced by interactions in conventional (Hermitian) spin and atomic systems, we refer to these as \mathbb{Z}_2 and \mathbb{Z}_3 orders respectively. The mechanism underlying their formation is similar to the U_1 setting, but here the longer-ranged interactions induce virtual boundaries located farther from the first boson at $x = 1$.

The same phenomenon occurs when $p > 2$ particles are present, which gives rise to spatially extended edge bursts occurring over p unit cells. Generally, the pres-

ence of $U_r > 0$ interactions for $r \leq 2d - 1$ can produce \mathbb{Z}_d edge burst orderings; with p bosons, the same \mathbb{Z}_d pattern occurs p times starting from the left boundary of the ladder (the drive direction of the NHSE). In Supplementary Note 4C, we describe additional experiments conducted with three bosons yielding a three-unit-cell spatially extended edge burst. We also observed qualitatively similar \mathbb{Z}_2 and \mathbb{Z}_3 orderings under longer-range interactions on the three-boson setup. Likewise we verified that the edge bursts do not arise in the trivial regime.

In the settings examined here (in Figure 5), the initial conditions were such that the bosons do not significantly infringe into the spatial ranges of U_r interactions under the dynamics of the system—*i.e.* they do not approach too closely to one another—until they impact on the left boundary. This allows the discussed physical mechanism to carry through unimpeded. As the leftward drift induced by the NHSE is approximately uniform, this condition is simple to achieve and boils down to the initial localization of the bosons. Indeed, in Figures 5a, 5c

and 5d, with $U_r > 0$ for $r \leq 2d - 1$, the bosons were initially separated by at least $2d + 1$ sites on the ladder or equivalently $\sim d$ unit cells. When this condition is not satisfied, a different type of interaction-driven edge burst phenomenology can occur, as we describe next.

G. Interaction-induced cluster bursts

Finally, we demonstrate that with appropriately configured interactions, anomalously high escape probabilities can be induced at chosen locations on the quantum ladder away from boundaries, in fact regardless of whether the Hamiltonian is in the (canonical) edge burst or trivial regimes. We term this phenomenon as cluster bursts. Unlike the canonical edge burst, cluster bursts need not occur at the edges of the system and arise intrinsically from interactions; there is no analogous single-body non-interacting counterpart known at present.

We show in Figure 6a experiment results on an $N = 14$ ladder in the canonical edge burst regime ($v_1 \leq v_2$) hosting two bosons. The bosons were initially localized on the a -sublattices of unit cells $x_0 = 8, 9$, and we enable density-density interaction U_1 of energy scale comparable to the non-interacting parts of the Hamiltonian (v_1, v_2, γ). Thus, the initial conditions are such that the particle separation condition discussed in the previous section is not clearly satisfied—in particular a single hop of either boson toward the other, via either v_1 or v_2 channels, places them within the range of interactions and causes a significant energy change. Strikingly we observe in experimentally measured \mathcal{P}_x that both bosons decay essentially *in-situ*, with an overwhelming proportion of escape probability concentrated precisely at $x = 8, 9$. The same cluster burst arises when the Hamiltonian is tuned into the trivial regime, as we show in Figure 6b, with qualitatively similar features in \mathcal{P}_x .

This same phenomenon can also arise when the initial localizations of the bosons are inside the range of interactions, such that outward hopping puts them outside their interaction range and causes an energy change. In this case, the bosons decay and a cluster burst emerges within the spatial confines of the interaction range. We show an example on the same $N = 14$ ladder in Figures 6c and 6d tuned into the edge burst and trivial regimes respectively. As before the bosons were initialized on unit cells $x_0 = 8, 9$, but here interactions $U_r > 0$ were switched on for $r \leq 3$. In both edge burst and trivial regimes, we observe clearly a cluster burst in the vicinity of the initial boson locations, far from boundaries.

The mechanism underlying these cluster bursts stem from energetically (partially) forbidden transitions caused by the interactions. We remind that energy is conserved in time translation-symmetric closed quantum systems—*i.e.* throughout time-evolution under a Hermitian Hamiltonian \mathcal{H} , the energy $\text{tr}(\omega_t \mathcal{H})$ of a quantum state ω_t is fixed. It is then a well-established effect that strong interactions can cause energy differences between

states connected by the Hamiltonian so large as to essentially forbid transitions out of or from a quantum state, as there is no available linear combination of accessible states after the transition that maintains the conserved energy. Indeed, this mechanism underlies a doublon decay phenomenon observed on Hubbard models [66, 67], where pairs of excitations in proximity exhibit exponentially long lifetimes, and is responsible also for the well-studied Stark many-body localization [68, 69].

A similar understanding holds in a non-Hermitian context, with the modification that energy is not exactly conserved but there exists nonetheless a speed limit on how fast energy can change in the system, imposed by the Hamiltonian (see Supplementary Note 1B). On the quantum ladder, this slow-down in dynamics freezes the bosons long enough that they decay largely in their initial locations, generating the cluster burst observed. In the scenarios demonstrated in Figure 6, for example, two simultaneous hoppings of the bosons must occur for them to move along the NHSE drive direction without changing their interaction energy, which is a second-order process and happens with low amplitude (probability). In the unlikely event that these higher-order hoppings occur and the bosons reach the boundary of the system, spatially extended edge bursts of small amplitude can additionally manifest, as can also be observed in Figure 6a.

III. DISCUSSION

While the experimental frontier of non-Hermitian condensed-matter physics has to-date enjoyed a spectacular period of progress utilizing broad palettes of custom-designed analog optical, metamaterial, and classical simulator platforms, the direct realization of important classes of non-Hermitian systems on near-term (*i.e.* NISQ) quantum platforms has remained very limited. The advantages offered by digital quantum simulation are clear and tantalizing: the natural ability to access the many-body Hilbert space of arbitrary Hamiltonians, and in association, liberal versatility in tuning interactions of different ranges, strengths and types.

But leveraging quantum simulators to probe non-Hermitian systems is challenging, as quantum operations on quantum devices are unitary and thus sophisticated methods must be developed to achieve the non-unitary evolution associated with non-Hermitian Hamiltonians. Moreover, the overhead incurred in doing so invariably runs up against qubit error and lifetime limitations. Nevertheless, recent studies of various condensed-matter phenomena on digital quantum computers, ranging from discrete time crystals [37, 70, 71] to topological phases [37, 41–45, 72–74], illustrate promising capabilities despite hardware constraints. It is therefore timely to investigate the prospects of studying non-Hermitian quantum physics on quantum hardware.

Here, we probed the recently discovered phenomenon of non-Hermitian edge bursts on transmon-based super-

conducting quantum processors, and observed at high fidelity the signatures of the edge burst on up to 64 unit cells of a lossy quantum ladder model. Furthermore, by incorporating sequences of density-density interactions, we unveiled the possibility of engineering spatially extended and ordered variants of the edge burst, as well as bursts occurring away from boundaries, which we dubbed cluster bursts. This marks the first time the non-Hermitian edge burst has been realized on an intrinsically quantum platform, as well as the first experimental study of interacting variants of the edge burst, complementing a prior experimental effort on the canonical non-interacting version of the edge burst [26, 27]. To enable this advance, we developed a general methodology for efficient non-Hermitian Hamiltonian simulation on digital quantum processors, leveraging a linear combination of unitaries circuit construction technique with ancillary qubit re-use, which is applicable to generic non-Hermitian models far beyond the scope of the edge burst.

Our work opens the door for future experimental investigation of quantum non-Hermitian condensed-matter. As quantum hardware continues to advance, we anticipate that our methods will enable the direct study of more sophisticated systems exhibiting rich intertwined physics, such as critical versions of non-Hermitian pumping [18] and the interplay between non-Hermiticity and

entanglement phase transitions [75].

IV. ACKNOWLEDGEMENTS

J.M.K. thanks Jayne Thompson, Jun Ye, and Jian Feng Kong of the Quantum Innovation Center (Q.Inc) and Institute of High Performance Computing (IHPC), Agency for Science, Technology and Research (A*STAR), Tianqi Chen of the National University of Singapore, and Mincheol Park of Harvard University, for helpful discussions. The authors acknowledge the use of IBM Quantum services for this work. The views expressed are those of the authors, and do not reflect the official policy or position of IBM or the IBM Quantum team. J.M.K. and T.T. are grateful for support from the A*STAR Graduate Academy. D.E.K. is supported by the National Research Foundation, Singapore, and the Agency for Science, Technology and Research (A*STAR), Singapore, under its Quantum Engineering Programme (NRF2021-QEP2-02-P03); A*STAR C230917003; and A*STAR under the Central Research Fund (CRF) Award for Use-Inspired Basic Research (UIBR) and the Quantum Innovation Centre (Q.InC) Strategic Research and Translational Thrust. We acknowledge support from the Ministry of Education, Singapore Tier-II grant (MOE award number: MOE-T2EP50222-0003).

-
- [1] Y. Ashida, Z. Gong, and M. Ueda, Non-Hermitian physics, *Adv. Phys.* **69**, 249 (2020).
 - [2] N. Okuma and M. Sato, Non-Hermitian topological phenomena: A review, *Annu. Rev. Condens. Matter Phys.* **14**, 83 (2023).
 - [3] R. Lin, T. Tai, L. Li, and C. H. Lee, Topological non-Hermitian skin effect, *Front. Phys.* **18**, 53605 (2023).
 - [4] X. Zhang, T. Zhang, M.-H. Lu, and Y.-F. Chen, A review on non-Hermitian skin effect, *Adv. Phys. X* **7**, 2109431 (2022).
 - [5] R. El-Ganainy, M. Khajavikhan, D. N. Christodoulides, and S. K. Ozdemir, The dawn of non-Hermitian optics, *Commun. Phys.* **2**, 37 (2019).
 - [6] A. Blais, A. L. Grimsmo, S. M. Girvin, and A. Wallraff, Circuit quantum electrodynamics, *Reviews of Modern Physics* **93**, 025005 (2021).
 - [7] K. Ding, C. Fang, and G. Ma, Non-Hermitian topology and exceptional-point geometries, *Nature Reviews Physics* **4**, 745 (2022).
 - [8] J. C. Budich and E. J. Bergholtz, Non-hermitian topological sensors, *Phys. Rev. Lett.* **125**, 180403 (2020).
 - [9] J. Wiersig, Prospects and fundamental limits in exceptional point-based sensing, *Nat. Commun.* **11**, 2454 (2020).
 - [10] E. Edvardsson and E. Ardonne, Sensitivity of non-Hermitian systems, *Phys. Rev. B* **106**, 115107 (2022).
 - [11] S. Yao and Z. Wang, Edge states and topological invariants of non-Hermitian systems, *Phys. Rev. Lett.* **121**, 086803 (2018).
 - [12] C. H. Lee and R. Thomale, Anatomy of skin modes and topology in non-Hermitian systems, *Phys. Rev. B* **99**, 201103 (2019).
 - [13] K. Yokomizo and S. Murakami, Non-Bloch band theory of non-Hermitian systems, *Phys. Rev. Lett.* **123**, 066404 (2019).
 - [14] S. Longhi, Probing non-Hermitian skin effect and non-Bloch phase transitions, *Phys. Rev. Res.* **1**, 023013 (2019).
 - [15] N. Okuma, K. Kawabata, K. Shiozaki, and M. Sato, Topological origin of non-Hermitian skin effects, *Phys. Rev. Lett.* **124**, 086801 (2020).
 - [16] K. Zhang, Z. Yang, and C. Fang, Universal non-Hermitian skin effect in two and higher dimensions, *Nat. Commun.* **13**, 2496 (2022).
 - [17] R. Shen and C. H. Lee, Non-Hermitian skin clusters from strong interactions, *Commun. Phys.* **5**, 238 (2022).
 - [18] L. Li, C. H. Lee, S. Mu, and J. Gong, Critical non-Hermitian skin effect, *Nat. Commun.* **11**, 5491 (2020).
 - [19] S. Mu, C. H. Lee, L. Li, and J. Gong, Emergent Fermi surface in a many-body non-Hermitian fermionic chain, *Phys. Rev. B* **102**, 081115 (2020).
 - [20] R. Yang, J. W. Tan, T. Tai, J. M. Koh, L. Li, S. Longhi, and C. H. Lee, Designing non-Hermitian real spectra through electrostatics, *Sci. Bull.* **67**, 1865 (2022).
 - [21] W.-T. Xue, Y.-M. Hu, F. Song, and Z. Wang, Non-Hermitian edge burst, *Phys. Rev. Lett.* **128**, 120401 (2022).

- [22] Y.-M. Hu, W.-T. Xue, F. Song, and Z. Wang, Steady-state edge burst: From free-particle systems to interaction-induced phenomena, *Phys. Rev. B* **108**, 235422 (2023).
- [23] L. Wang, Q. Liu, and Y. Zhang, Quantum dynamics on a lossy non-Hermitian lattice, *Chin. Phys. B* **30**, 020506 (2021).
- [24] C. Yuce and H. Ramezani, Non-Hermitian edge burst without skin localization, *Phys. Rev. B* **107**, L140302 (2023).
- [25] P. Wen, J. Pi, and G.-L. Long, Investigation of a non-Hermitian edge burst with time-dependent perturbation theory, *Phys. Rev. A* **109**, 022236 (2024).
- [26] L. Xiao, W.-T. Xue, F. Song, Y.-M. Hu, W. Yi, Z. Wang, and P. Xue, Observation of non-hermitian edge burst in quantum dynamics, *Phys. Rev. Lett.* **133**, 070801 (2024).
- [27] J. Zhu, Y.-L. Mao, H. Chen, K.-X. Yang, L. Li, B. Yang, Z.-D. Li, and J. Fan, Observation of non-Hermitian edge burst effect in one-dimensional photonic quantum walk, *Phys. Rev. Lett.* **132**, 203801 (2024).
- [28] A. Li, H. Wei, M. Cotrufo, W. Chen, S. Mann, X. Ni, B. Xu, J. Chen, J. Wang, S. Fan, C.-W. Qiu, A. Alù, and L. Chen, Exceptional points and non-Hermitian photonics at the nanoscale, *Nat. Nanotechnol.* **18**, 706 (2023).
- [29] T. Helbig, T. Hofmann, S. Imhof, M. Abdelghany, T. Kiessling, L. W. Molenkamp, C. H. Lee, A. Szameit, M. Greiter, and R. Thomale, Generalized bulk-boundary correspondence in non-Hermitian topoelectrical circuits, *Nat. Phys.* **16**, 747 (2020).
- [30] N. C. Rubin, D. W. Berry, A. Kononov, F. D. Malone, T. Khattar, A. White, J. Lee, H. Neven, R. Babbush, and A. D. Baczewski, Quantum computation of stopping power for inertial fusion target design, *Proc. Natl. Acad. Sci. U.S.A.* **121**, e2317772121 (2024).
- [31] Google Quantum AI and collaborators, Measurement-induced entanglement and teleportation on a noisy quantum processor, *Nature* **622**, 481 (2023).
- [32] J. M. Koh, S.-N. Sun, M. Motta, and A. J. Minnich, Measurement-induced entanglement phase transition on a superconducting quantum processor with mid-circuit readout, *Nat. Phys.* **19**, 1314 (2023).
- [33] D. Jafferis, A. Zlokapa, J. D. Lykken, D. K. Kolchmeyer, S. I. Davis, N. Lauk, H. Neven, and M. Spiropulu, Traversable wormhole dynamics on a quantum processor, *Nature* **612**, 51 (2022).
- [34] A. J. Daley, I. Bloch, C. Kokail, S. Flannigan, N. Pearson, M. Troyer, and P. Zoller, Practical quantum advantage in quantum simulation, *Nature* **607**, 667 (2022).
- [35] W. L. Tan, P. Becker, F. Liu, G. Pagano, K. Collins, A. De, L. Feng, H. Kaplan, A. Kyprianidis, R. Lundgren, *et al.*, Domain-wall confinement and dynamics in a quantum simulator, *Nat. Phys.* **17**, 742 (2021).
- [36] S.-N. Sun, B. Marinelli, J. M. Koh, Y. Kim, L. B. Nguyen, L. Chen, J. M. Kreikebaum, D. I. Santiago, I. Siddiqi, and A. J. Minnich, Quantum computation of frequency-domain molecular response properties using a three-qubit itoffoli gate, *npj Quantum Inf.* **10**, 55 (2024).
- [37] X. Mi, M. Ippoliti, C. Quintana, A. Greene, Z. Chen, J. Gross, F. Arute, K. Arya, J. Atalaya, R. Babbush, *et al.*, Time-crystalline eigenstate order on a quantum processor, *Nature* **601**, 531 (2022).
- [38] L. Clinton, T. Cubitt, B. Flynn, F. M. Gambetta, J. Klassen, A. Montanaro, S. Piddock, R. A. Santos, and E. Sheridan, Towards near-term quantum simulation of materials, *Nat. Commun.* **15**, 211 (2024).
- [39] S. Ebadi, T. T. Wang, H. Levine, A. Keesling, G. Semeghini, A. Omran, D. Bluvstein, R. Samajdar, H. Pichler, W. W. Ho, *et al.*, Quantum phases of matter on a 256-atom programmable quantum simulator, *Nature* **595**, 227 (2021).
- [40] Y. Kim, A. Eddins, S. Anand, K. X. Wei, E. Van Den Berg, S. Rosenblatt, H. Nayfeh, Y. Wu, M. Zaletel, K. Temme, *et al.*, Evidence for the utility of quantum computing before fault tolerance, *Nature* **618**, 500 (2023).
- [41] K. Satzinger, Y.-J. Liu, A. Smith, C. Knapp, M. Newman, C. Jones, Z. Chen, C. Quintana, X. Mi, A. Dunsworth, *et al.*, Realizing topologically ordered states on a quantum processor, *Science* **374**, 1237 (2021).
- [42] Google Quantum AI and Collaborators, Non-abelian braiding of graph vertices in a superconducting processor, *Nature* **618**, 264 (2023).
- [43] J. M. Koh, T. Tai, and C. H. Lee, Realization of higher-order topological lattices on a quantum computer, *Nat. Commun.* **15**, 5807 (2024).
- [44] J. M. Koh, T. Tai, and C. H. Lee, Simulation of interaction-induced chiral topological dynamics on a digital quantum computer, *Phys. Rev. Lett.* **129**, 140502 (2022).
- [45] J. M. Koh, T. Tai, Y. H. Phee, W. E. Ng, and C. H. Lee, Stabilizing multiple topological fermions on a quantum computer, *npj Quantum Inf.* **8**, 16 (2022).
- [46] A. Jebraeilli and M. R. Geller, *Quantum simulation of a qubit with non-Hermitian Hamiltonian* (2025), arXiv:2502.13910 [quant-ph].
- [47] J. Bian, P. Lu, T. Liu, H. Wu, X. Rao, K. Wang, Q. Lao, Y. Liu, F. Zhu, and L. Luo, Quantum simulation of a general anti-PT-symmetric Hamiltonian with a trapped ion qubit, *Fundam. Res.* **3**, 904 (2023).
- [48] J. Wen, C. Zheng, X. Kong, S. Wei, T. Xin, and G. Long, Experimental demonstration of a digital quantum simulation of a general \mathcal{PT} -symmetric system, *Phys. Rev. A* **99**, 062122 (2019).
- [49] R. Shen, T. Chen, B. Yang, and C. H. Lee, Observation of the non-Hermitian skin effect and Fermi skin on a digital quantum computer, *Nat. Commun.* **16**, 1340 (2025).
- [50] R. Shen, F. Qin, J.-Y. Desautels, Z. Papić, and C. H. Lee, Enhanced many-body quantum scars from the non-Hermitian fock skin effect, *Phys. Rev. Lett.* **133**, 216601 (2024).
- [51] H. Liu, X. Yang, K. Tang, L. Che, X. Nie, T. Xin, J. Li, and D. Lu, Practical quantum simulation of small-scale non-Hermitian dynamics, *Phys. Rev. A* **107**, 062608 (2023).
- [52] N. Hatano and M. Suzuki, Finding exponential product formulas of higher orders, in *Quantum Annealing and Other Optimization Methods*, edited by A. Das and B. K. Chakrabarti (Springer Berlin Heidelberg, Berlin, Heidelberg, 2005) pp. 37–68.
- [53] J. Ostmeyer, Optimised Trotter decompositions for classical and quantum computing, *J. Phys. A: Mathematical and Theoretical* **56**, 285303 (2023).

- [54] T. N. Ikeda, H. Kono, and K. Fujii, Measuring Trotter error and its application to precision-guaranteed Hamiltonian simulations, *Phys. Rev. Res.* **6**, 033285 (2024).
- [55] M. Motta, C. Sun, A. T. Tan, M. J. O’Rourke, E. Ye, A. J. Minnich, F. G. Brandao, and G. K.-L. Chan, Determining eigenstates and thermal states on a quantum computer using quantum imaginary time evolution, *Nat. Phys.* **16**, 205 (2020).
- [56] S.-N. Sun, M. Motta, R. N. Tazhigulov, A. T. Tan, G. K.-L. Chan, and A. J. Minnich, Quantum computation of finite-temperature static and dynamical properties of spin systems using quantum imaginary time evolution, *PRX Quantum* **2**, 010317 (2021).
- [57] S. McArdle, T. Jones, S. Endo, Y. Li, S. C. Benjamin, and X. Yuan, Variational ansatz-based quantum simulation of imaginary time evolution, *npj Quantum Inf.* **5**, 75 (2019).
- [58] H. Nishi, T. Kosugi, and Y.-i. Matsushita, Implementation of quantum imaginary-time evolution method on NISQ devices by introducing nonlocal approximation, *npj Quantum Inf.* **7**, 85 (2021).
- [59] C. H. Lee, S. Imhof, C. Berger, F. Bayer, J. Brehm, L. W. Molenkamp, T. Kiessling, and R. Thomale, Topolectrical circuits, *Commun. Phys.* **1**, 39 (2018).
- [60] D. Zou, T. Chen, W. He, J. Bao, C. H. Lee, H. Sun, and X. Zhang, Observation of hybrid higher-order skin-topological effect in non-Hermitian topolectrical circuits, *Nat. Commun.* **12**, 7201 (2021).
- [61] H. Zhang, T. Chen, L. Li, C. H. Lee, and X. Zhang, Electrical circuit realization of topological switching for the non-Hermitian skin effect, *Phys. Rev. B* **107**, 085426 (2023).
- [62] H. Alaeian and J. A. Dionne, Non-Hermitian nanophotonic and plasmonic waveguides, *Phys. Rev. B* **89**, 075136 (2014).
- [63] H. Nasari, G. G. Pyrialakos, D. N. Christodoulides, and M. Khajavikhan, Non-Hermitian topological photonics, *Opt. Mater. Express* **13**, 870 (2023).
- [64] C. H. Lee, Many-body topological and skin states without open boundaries, *Phys. Rev. B* **104**, 195102 (2021).
- [65] R. Shen and C. H. Lee, Non-Hermitian skin clusters from strong interactions, *Commun. Phys.* **5**, 238 (2022).
- [66] C. Yin and A. Lucas, Prethermalization and the local robustness of gapped systems, *Phys. Rev. Lett.* **131**, 050402 (2023).
- [67] R. Sensarma, D. Pekker, E. Altman, E. Demler, N. Strohmaier, D. Greif, R. Jördens, L. Tarruell, H. Moritz, and T. Esslinger, Lifetime of double occupancies in the Fermi-Hubbard model, *Phys. Rev. B* **82**, 224302 (2010).
- [68] M. Schulz, C. A. Hooley, R. Moessner, and F. Pollmann, Stark many-body localization, *Phys. Rev. Lett.* **122**, 040606 (2019).
- [69] W. Morong, F. Liu, P. Becker, K. Collins, L. Feng, A. Kyprianidis, G. Pagano, T. You, A. Gorshkov, and C. Monroe, Observation of stark many-body localization without disorder, *Nature* **599**, 393 (2021).
- [70] P. Frey and S. Rachel, Realization of a discrete time crystal on 57 qubits of a quantum computer, *Science advances* **8**, eabm7652 (2022).
- [71] T. Chen, R. Shen, C. H. Lee, B. Yang, and R. W. Bomantara, A robust large-period discrete time crystal and its signature in a digital quantum computer (2023), arXiv:2309.11560 [quant-ph].
- [72] D. Azses, R. Haenel, Y. Naveh, R. Raussendorf, E. Sela, and E. G. Dalla Torre, Identification of symmetry-protected topological states on noisy quantum computers, *Phys. Rev. Lett.* **125**, 120502 (2020).
- [73] F. Mei, Q. Guo, Y.-F. Yu, L. Xiao, S.-L. Zhu, and S. Jia, Digital simulation of topological matter on programmable quantum processors, *Phys. Rev. Lett.* **125**, 160503 (2020).
- [74] M. Iqbal, N. Tantivasadakarn, T. M. Gatterman, J. A. Gerber, K. Gilmore, D. Gresh, A. Hankin, N. Hewitt, C. V. Horst, M. Matheny, *et al.*, Topological order from measurements and feed-forward on a trapped ion quantum computer, *Commun. Phys.* **7**, 205 (2024).
- [75] K. Kawabata, T. Numasawa, and S. Ryu, Entanglement phase transition induced by the non-hermitian skin effect, *Phys. Rev. X* **13**, 021007 (2023).
- [76] D. C. McKay, C. J. Wood, S. Sheldon, J. M. Chow, and J. M. Gambetta, Efficient z gates for quantum computing, *Phys. Rev. A* **96**, 022330 (2017).
- [77] N. Sundaresan, I. Lauer, E. Pritchett, E. Magesan, P. Jurcevic, and J. M. Gambetta, Reducing unitary and spectator errors in cross resonance with optimized rotary echoes, *PRX Quantum* **1**, 020318 (2020).
- [78] M. Kormos, M. Collura, and P. Calabrese, Analytic results for a quantum quench from free to hard-core one-dimensional bosons, *Phys. Rev. A* **89**, 013609 (2014).
- [79] I. Kassal, S. P. Jordan, P. J. Love, M. Mohseni, and A. Aspuru-Guzik, Polynomial-time quantum algorithm for the simulation of chemical dynamics, *Proc. Natl. Acad. Sci. U.S.A.* **105**, 18681 (2008).
- [80] D. W. Berry, M. Kieferová, A. Scherer, Y. R. Sanders, G. H. Low, N. Wiebe, C. Gidney, and R. Babbush, Improved techniques for preparing eigenstates of fermionic Hamiltonians, *npj Quantum Inf.* **4**, 22 (2018).
- [81] R. Babbush, D. W. Berry, J. R. McClean, and H. Neven, Quantum simulation of chemistry with sublinear scaling in basis size, *npj Quantum Inf.* **5**, 92 (2019).
- [82] R. Babbush, N. Wiebe, J. McClean, J. McClain, H. Neven, and G. K.-L. Chan, Low-depth quantum simulation of materials, *Phys. Rev. X* **8**, 011044 (2018).
- [83] R. R. Tucci, An Introduction to Cartan’s KAK Decomposition for QC Programmers (2005), arXiv:quant-ph/0507171 [quant-ph].
- [84] M. G. Davis, E. Smith, A. Tudor, K. Sen, I. Siddiqi, and C. Iancu, Towards optimal topology aware quantum circuit synthesis, in *2020 IEEE International Conference on Quantum Computing and Engineering (QCE)* (IEEE, 2020) pp. 223–234.
- [85] E. Younis, C. C. Iancu, W. Lavrijsen, M. Davis, and E. Smith, *Berkeley quantum synthesis toolkit (bqskit) v1*, Tech. Rep. (Lawrence Berkeley National Lab, Berkeley, CA, United States, 2021).
- [86] E. Van Den Berg and K. Temme, Circuit optimization of Hamiltonian simulation by simultaneous diagonalization of Pauli clusters, *Quantum* **4**, 322 (2020).
- [87] P. Gokhale, O. Angiuli, Y. Ding, K. Gui, T. Tomesh, M. Suchara, M. Martonosi, and F. T. Chong, *Minimizing state preparations in variational quantum eigensolver by partitioning into commuting families* (2019), arXiv:1907.13623 [quant-ph].
- [88] A. M. Childs and N. Wiebe, Hamiltonian simulation using linear combinations of unitary operations, *Quantum Info. Comput.* **12**, 901–924 (2012).

- [89] D. W. Berry, A. M. Childs, R. Cleve, R. Kothari, and R. D. Somma, Simulating Hamiltonian dynamics with a truncated Taylor series, *Phys. Rev. Lett.* **114**, 090502 (2015).
- [90] M. Ezawa, Systematic construction of square-root topological insulators and superconductors, *Phys. Rev. Res.* **2**, 033397 (2020).
- [91] A. M. Marques, L. Madaïl, and R. G. Dias, One-dimensional 2^n -root topological insulators and superconductors, *Phys. Rev. B* **103**, 235425 (2021).
- [92] M. Kremer, I. Petrides, E. Meyer, M. Heinrich, O. Zilberberg, and A. Szameit, A square-root topological insulator with non-quantized indices realized with photonic Aharonov-Bohm cages, *Nat. Commun.* **11**, 907 (2020).
- [93] H. Wu, G. Wei, Z. Liu, and J.-J. Xiao, Square-root topological state of coupled plasmonic nanoparticles in a decorated Su-Schrieffer-Heeger lattice, *Opt. Lett.* **46**, 4256 (2021).
- [94] W. Deng, T. Chen, and X. Zhang, n th power root topological phases in Hermitian and non-Hermitian systems, *Phys. Rev. Res.* **4**, 033109 (2022).
- [95] L. Song, H. Yang, Y. Cao, and P. Yan, Square-root higher-order Weyl semimetals, *Nat. Commun.* **13**, 5601 (2022).
- [96] A. M. Marques and R. G. Dias, 2^n -root weak, chern, and higher-order topological insulators, and 2^n -root topological semimetals, *Phys. Rev. B* **104**, 165410 (2021).
- [97] Z. Lin, S. Ke, X. Zhu, and X. Li, Square-root non-Bloch topological insulators in non-Hermitian ring resonators, *Opt. Express* **29**, 8462 (2021).
- [98] S. Guo, G. Pan, J. Huang, R. Huang, F. Zhuang, S. Su, Z. Lin, W. Qiu, and Q. Kan, Realization of the square-root higher-order topology in decorated Su-Schrieffer-Heeger electric circuits, *Appl. Phys. Lett.* **123**, 043102 (2023).
- [99] Z.-G. Geng, Y.-X. Shen, Z. Xiong, L. Duan, Z. Chen, and X.-F. Zhu, Quartic-root higher-order topological insulators on decorated three-dimensional sonic crystals, *APL Mater.* **12**, 021108 (2024).
- [100] E. Bäumer, V. Tripathi, A. Seif, D. Lidar, and D. S. Wang, Quantum Fourier transform using dynamic circuits, *Phys. Rev. Lett.* **133**, 150602 (2024).
- [101] E. Bäumer, V. Tripathi, D. S. Wang, P. Rall, E. H. Chen, S. Majumder, A. Seif, and Z. K. Mineev, Efficient long-range entanglement using dynamic circuits, *PRX Quantum* **5**, 030339 (2024).
- [102] A. D. Córcoles, M. Takita, K. Inoue, S. Lekuch, Z. K. Mineev, J. M. Chow, and J. M. Gambetta, Exploiting dynamic quantum circuits in a quantum algorithm with superconducting qubits, *Phys. Rev. Lett.* **127**, 100501 (2021).
- [103] J. R. McClean, J. Romero, R. Babbush, and A. Aspuru-Guzik, The theory of variational hybrid quantum-classical algorithms, *New J. Phys.* **18**, 023023 (2016).
- [104] J. R. McClean, R. Babbush, P. J. Love, and A. Aspuru-Guzik, Exploiting locality in quantum computation for quantum chemistry, *J. Phys. Chem. Lett.* **5**, 4368 (2014).
- [105] A. Peruzzo, J. McClean, P. Shadbolt, M.-H. Yung, X.-Q. Zhou, P. J. Love, A. Aspuru-Guzik, and J. L. O'Brien, A variational eigenvalue solver on a photonic quantum processor, *Nat. Commun.* **5**, 4213 (2014).
- [106] S. Khatri, R. LaRose, A. Poremba, L. Cincio, A. T. Sornborger, and P. J. Coles, Quantum-assisted quantum compiling, *Quantum* **3**, 140 (2019).
- [107] K. Heya, Y. Suzuki, Y. Nakamura, and K. Fujii, Variational quantum gate optimization (2018), [arXiv:1810.12745 \[quant-ph\]](https://arxiv.org/abs/1810.12745).
- [108] L. O. Conlon, J. M. Koh, B. Shajilal, J. Sidhu, P. K. Lam, and S. M. Assad, Attainability of quantum state discrimination bounds with collective measurements on finite copies, *Phys. Rev. A* **111**, 022438 (2025).
- [109] J. Gray, quimb: A python package for quantum information and many-body calculations, *J. Open Source Softw.* **3**, 819 (2018).
- [110] G. Andrew and J. Gao, Scalable training of L1-regularized log-linear models, in *Proceedings of the 24th International Conference on Machine Learning*, ICML '07 (Association for Computing Machinery, New York, NY, USA, 2007) p. 33–40.
- [111] A. Kandala, A. Mezzacapo, K. Temme, M. Takita, M. Brink, J. M. Chow, and J. M. Gambetta, Hardware-efficient variational quantum eigensolver for small molecules and quantum magnets, *Nature* **549**, 242 (2017).
- [112] A. Kandala, K. Temme, A. D. Córcoles, A. Mezzacapo, J. M. Chow, and J. M. Gambetta, Error mitigation extends the computational reach of a noisy quantum processor, *Nature* **567**, 491 (2019).
- [113] P. Jurcevic, A. Javadi-Abhari, L. S. Bishop, I. Lauer, D. F. Bogorin, M. Brink, L. Capelluto, O. Günlük, T. Itoko, N. Kanazawa, *et al.*, Demonstration of quantum volume 64 on a superconducting quantum computing system, *Quantum Sci. Technol.* **6**, 025020 (2021).
- [114] D. Suter and G. A. Álvarez, Colloquium: Protecting quantum information against environmental noise, *Rev. Mod. Phys.* **88**, 041001 (2016).
- [115] A. A. Clerk, M. H. Devoret, S. M. Girvin, F. Marquardt, and R. J. Schoelkopf, Introduction to quantum noise, measurement, and amplification, *Rev. Mod. Phys.* **82**, 1155 (2010).
- [116] J. A. Smolin, J. M. Gambetta, and G. Smith, Efficient method for computing the maximum-likelihood quantum state from measurements with additive gaussian noise, *Phys. Rev. Lett.* **108**, 070502 (2012).
- [117] J. M. Koh, D. E. Koh, and J. Thompson, Readout error mitigation for mid-circuit measurements and feed-forward (2024), [arXiv:2406.07611 \[quant-ph\]](https://arxiv.org/abs/2406.07611).
- [118] L. Viola, E. Knill, and S. Lloyd, Dynamical decoupling of open quantum systems, *Phys. Rev. Lett.* **82**, 2417 (1999).
- [119] B. Pokharel, N. Anand, B. Fortman, and D. A. Lidar, Demonstration of fidelity improvement using dynamical decoupling with superconducting qubits, *Phys. Rev. Lett.* **121**, 220502 (2018).
- [120] K. Khodjasteh and D. A. Lidar, Fault-tolerant quantum dynamical decoupling, *Phys. Rev. Lett.* **95**, 180501 (2005).
- [121] G. S. Uhrig, Keeping a quantum bit alive by optimized π -pulse sequences, *Phys. Rev. Lett.* **98**, 100504 (2007).
- [122] N. Ezzell, B. Pokharel, L. Tewala, G. Quiroz, and D. A. Lidar, Dynamical decoupling for superconducting qubits: A performance survey, *Phys. Rev. Appl.* **20**, 064027 (2023).
- [123] A. Hashim, R. K. Naik, A. Morvan, J.-L. Ville, B. Mitchell, J. M. Kreikebaum, M. Davis, E. Smith, C. Iancu, K. P. O'Brien, I. Hincks, J. J. Wallman, J. Emerson, and I. Siddiqi, Randomized compiling for

- scalable quantum computing on a noisy superconducting quantum processor, *Phys. Rev. X* **11**, 041039 (2021).
- [124] J. J. Wallman and J. Emerson, Noise tailoring for scalable quantum computation via randomized compiling, *Phys. Rev. A* **94**, 052325 (2016).
- [125] Y. Kim, C. J. Wood, T. J. Yoder, S. T. Merkel, J. M. Gambetta, K. Temme, and A. Kandala, Scalable error mitigation for noisy quantum circuits produces competitive expectation values, *Nat. Phys.* **19**, 752 (2023).
- [126] R. Majumdar, P. Rivero, F. Metz, A. Hasan, and D. S. Wang, Best practices for quantum error mitigation with digital zero-noise extrapolation, in *2023 IEEE International Conference on Quantum Computing and Engineering (QCE)*, Vol. 1 (IEEE, 2023) pp. 881–887.
- [127] T. Giurgica-Tiron, Y. Hindy, R. LaRose, A. Mari, and W. J. Zeng, Digital zero noise extrapolation for quantum error mitigation, in *2020 IEEE International Conference on Quantum Computing and Engineering (QCE)* (IEEE, 2020) pp. 306–316.
- [128] K. Temme, S. Bravyi, and J. M. Gambetta, Error mitigation for short-depth quantum circuits, *Phys. Rev. Lett.* **119**, 180509 (2017).
- [129] J. W. O. Garmon, R. C. Pooser, and E. F. Dumitrescu, Benchmarking noise extrapolation with the openpulse control framework, *Phys. Rev. A* **101**, 042308 (2020).
- [130] S. Diamond and S. Boyd, CVXPY: a python-embedded modeling language for convex optimization, *J. Mach. Learn. Res.* **17**, 2909–2913 (2016).
- [131] B. Stellato, G. Banjac, P. Goulart, A. Bemporad, and S. Boyd, OSQP: an operator splitting solver for quadratic programs, *Math. Program. Comput.* **12**, 637 (2020).
- [132] P. D. Nation and M. Treinish, Suppressing quantum circuit errors due to system variability, *PRX Quantum* **4**, 010327 (2023).
- [133] S. Niu, A. Suau, G. Staffelbach, and A. Todri-Sanial, A hardware-aware heuristic for the qubit mapping problem in the NISQ era, *IEEE Trans. Quantum Eng.* **1**, 1 (2020).

METHODS

Quantum hardware. We used IBM transmon-based superconducting quantum devices in our experiments. These included 27-qubit devices *ibm_hanoi* and *ibm_mumbai* hosting the Falcon processor, 127-qubit devices *ibm_sherbrooke*, *ibm_osaka*, *ibm_kyoto* and *ibm_nazca* hosting the Eagle processor, and a 133-qubit device *ibm_torino* hosting the Heron processor. The basis gate sets of all devices comprise 1-qubit gates $\{X, \sqrt{X}, \text{RZ}\}$, with RZ implemented virtually via framechanges [76], and 2-qubit gate CX for Falcon processors, echoed cross resonance (ECR) for Eagle processors [77], and CZ for the Heron processor. The CX, ECR and CZ gates are equivalent up to 1-qubit rotations. We construct all experiment circuits using CX gates, including the application of protocols for error suppression and mitigation such as Pauli twirling and randomized gate folding for zero-noise extrapolation (see below), and transpile to the native 2-qubit gate of each device before execution. Typical performance metrics of the devices, such as relaxation T_1 and dephasing T_2 times, gate and readout error rates, and gate times are provided in Supplementary Table S4.

Model. We examined the bosonic quantum ladder Hamiltonian $\mathcal{H}^{\text{eb}} = \mathcal{H}_0^{\text{eb}} + \mathcal{H}_{\text{int}}^{\text{eb}}$, where $\mathcal{H}_0^{\text{eb}}$ and $\mathcal{H}_{\text{int}}^{\text{eb}}$ comprise non-interacting and interacting terms respectively, given by

$$\mathcal{H}_0^{\text{eb}} = \sum_{x=1}^N \left\{ -i\gamma c_{x,b}^\dagger c_{x,b} + \left(v_1 c_{x,a}^\dagger c_{x,a} + \frac{v_2}{2} \left[c_{(x+1),a}^\dagger c_{x,b} + c_{(x+1),b}^\dagger c_{x,a} \right] + \frac{iv_2}{2} \left[c_{(x+1),a}^\dagger c_{x,a} - c_{(x+1),b}^\dagger c_{x,b} \right] + \text{h.c.} \right) \right\}, \quad (7)$$

$$\mathcal{H}_{\text{int}}^{\text{eb}} = U_0 \sum_{z=1}^{2N} n_z (n_z - 1) + \sum_{r \geq 1} U_r \left(\sum_{z=1}^{2N} n_z n_{z+r} \right),$$

over N unit cells. Above, $v_1, v_2 \geq 0$ are intra- and inter-cell hopping coefficients, $\gamma > 0$ is a loss rate on b -sublattices, $U_0 \in \mathbb{R}$ is an on-site interaction strength, and $U_r \in \mathbb{R}$ are range- r density-density interaction strengths between sites on the flattened ladder. The operator $c_{x,\ell}$ annihilates a particle at sublattice $\ell \in \{a, b\}$ of unit cell $x \in [N]$, and $n_z = c_{x,\ell}^\dagger c_{x,\ell}$ is the number operator with index $z = 2x - \delta_{\ell a} \in [2N]$ labeling sites on the ladder with sublattice structure flattened. Open boundary conditions (OBC) are imposed by zeroing $c_{x,\ell} = 0$ for $x \notin [N]$; periodic boundary conditions (PBC) correspond to setting $c_{x,\ell} = c_{(x+N),\ell}$. The Hamiltonian is manifestly non-Hermitian (as $\gamma > 0$). Writing $\mathcal{H}^{\text{eb}} = \mathcal{H}_{\text{H}}^{\text{eb}} - i\mathcal{H}_{\text{A}}^{\text{eb}}$ for Hermitian and anti-Hermitian components $\mathcal{H}_{\text{H}}^{\text{eb}}$ and $-i\mathcal{H}_{\text{A}}^{\text{eb}}$, we have

$$\mathcal{H}_{\text{A}}^{\text{eb}} = \gamma \sum_{x=1}^N c_{x,b}^\dagger c_{x,b}, \quad (8)$$

containing the non-Hermitian loss.

The non-interacting $\mathcal{H}_0^{\text{eb}}$ is identical to the paradigmatic lossy quantum walk Hamiltonian studied in Refs. [21, 24]. Notably, the non-Hermitian skin effect (NHSE) is present for all $v_1 \neq 0$, as implied by an equivalence of $\mathcal{H}_0^{\text{eb}}$ to the non-Hermitian Su-Schrieffer-Heeger (SSH) model [11] with left-right asymmetric hoppings under a unitary basis transformation. Alternatively, the NHSE can be understood as arising from the suppression of the $+\hat{x}$ -direction portion of flux-induced rotational motion by the γ loss, as mentioned in the

main text. The imaginary (*i.e.* dissipative) gap closes [21] for $v_1 \leq v_2$, which is the canonical regime where the non-Hermitian edge burst manifests.

In $\mathcal{H}_{\text{int}}^{\text{eb}}$, we take the $U_0 \rightarrow \infty$ limit for simplicity, such that hardcore bosonic statistics arise [78]. We allow U_r to be independently tuned for each r to access a variety of multi-particle interacting edge burst phenomena. Note that \mathcal{H}^{eb} possesses a $U(1)$ number conservation symmetry in the c bosons.

Qubit encoding. To perform simulation of \mathcal{H}^{eb} on quantum hardware, a mapping between basis states of the system and qubit states must be fixed, which also induces a mapping between the operators of the system ($c_{x,\ell}$) and qubit operators. As \mathcal{H}^{eb} is number-conserving, its Hilbert (Fock) space is the direct sum of disconnected Fock sectors identified by particle numbers. We leverage this structure in state encoding. In the single-particle sector, we identified

$$|(x, \ell)\rangle_{\text{sys}} = |2x - \delta_{\ell a} - 1\rangle_{\text{q}}, \quad (9)$$

where $|(x, \ell)\rangle_{\text{sys}}$ is the system state with a particle at unit cell $x \in [1, N]$ and sublattice $\ell \in \{a, b\}$, and $|2x - \delta_{\ell a} - 1\rangle_{\text{q}}$ is the associated computational basis state on the qubits¹. Thus $N_{\text{q}} = \lceil \log_2 2N \rceil$ system qubits are required to represent the \mathcal{H}^{eb} quantum ladder in this Fock sector.

More generally, in the p -particle sector, we used a bijection between system states $|\{(x_1, \ell_1), \dots, (x_p, \ell_p)\}\rangle_{\text{sys}}$, which denote particle occupation at distinct sites $\{(x_1, \ell_1), \dots, (x_p, \ell_p)\}$ for $x_k \in [1, N]$, $\ell_k \in \{a, b\}$, and qubit states in lexicographic ascending order. Thus minimally $N_{\text{q}} = \lceil \log_2(2N)! / (2N - p)! \rceil \in \mathcal{O}(p \log_2 N)$ qubits are required to represent the quantum ladder. This mapping is similar to first-quantization encoding used in quantum chemistry [79–81] as opposed to second-quantization mapping [82], which requires a number of qubits independent of p but linear in N .

Fock-sector error detection. In our experiments, the number of available qubit states may exceed the number of system states—therefore some qubit states may be unused in state encoding (see above). These qubit states have no physical meaning and should not be involved in time-evolution of any physical system state. Nonetheless, hardware noise may cause these states to be erroneously populated. We discard circuit shots that measured occupation of these states, as these results are unphysical and indicate hardware error.

Time-evolution on non-Hermitian Hamiltonians. Given a local Hamiltonian \mathcal{H} , which need not be Hermitian, an initial state ρ_0 , and an evolution time $t \geq 0$, we describe an algorithm to perform normalized time-evolution,

$$\rho_0 \rightarrow \rho_t = \mathcal{N} \left[e^{-i\mathcal{H}t} \rho_0 e^{+i\mathcal{H}^\dagger t} \right], \quad (10)$$

where $\mathcal{N}[\rho] = \rho / \text{tr}(\rho)$ normalizes a quantum state. Writing $\mathcal{H} = \mathcal{H}_{\text{H}} - i\mathcal{H}_{\text{A}}$ such that \mathcal{H}_{H} and $-i\mathcal{H}_{\text{A}}$ are respectively the Hermitian and anti-Hermitian components of \mathcal{H} , we split (*i.e.* trotterize) the evolution into m time steps, such that

$$(\mathcal{M}_{\text{A}} \circ \mathcal{M}_{\text{H}})^m (\rho_0) = \rho_t + \mathcal{O}\left(\frac{1}{m}\right), \quad (11)$$

¹ Throughout our work an implicit conversion of integer labels for qubit states to binary representation is assumed, that is, $|z\rangle = |\bar{z}\rangle = |\bar{z}_1\rangle \otimes |\bar{z}_2\rangle \otimes \dots$ for $z \in \mathbb{N}$ and \bar{z} the binary representation (*i.e.* bitstring) of z , and $\bar{z}_1, \bar{z}_2, \dots$ are its digits (bits).

where \mathcal{M}_H and \mathcal{M}_A are quantum maps that we seek to implement, satisfying

$$\begin{aligned}\mathcal{M}_H(\rho) &= e^{-i\mathcal{H}_H\Delta t}\rho e^{+i\mathcal{H}_H\Delta t} + \mathcal{O}\left(\frac{1}{m^2}\right), \\ \mathcal{M}_A(\rho) &= \mathcal{N}\left[e^{-\mathcal{H}_A\Delta t}\rho e^{-\mathcal{H}_A\Delta t}\right] + \mathcal{O}\left(\frac{1}{m^2}\right),\end{aligned}\quad (12)$$

for the time interval $\Delta t = t/m$ and any arbitrary ρ . The error scaling in Eq. (11) implies that arbitrary precision in time-evolution can be achieved by increasing m .

The main difficulty is in realizing \mathcal{M}_A as the transformation is non-unitary. The core idea is to utilize a dilated Hilbert space with an ancillary register, which can be as small as a single qubit, and to implement a joint unitary such that the desired transformation is applied on the system register upon measurement of the ancillae. We detail a systematic non-variational approach for constructing such a circuit with classical processing costs polynomial in the size of the system (see [below](#)). For future use, we denote the Pauli decompositions

$$\mathcal{H}_H = \sum_{k=1}^{K_H} \alpha_k \sigma^k, \quad \mathcal{H}_A = \sum_{k=1}^{K_A} \beta_k \chi^k, \quad (13)$$

for $\alpha_k, \beta_k \in \mathbb{R}$ and Pauli strings σ^k, χ^k assumed to be known from the given \mathcal{H} . As \mathcal{H} is local, the number of Pauli terms $K_H, K_A \in \text{poly}(N)$.

Implementation of \mathcal{M}_H . The unitary channel \mathcal{M}_H performs time-evolution by the Hermitian Hamiltonian \mathcal{H}_H and can be implemented through any product formula. In our work, we used the first-order Lie-Trotter formula to set

$$\mathcal{M}_H(\rho) = U_H \rho U_H^\dagger, \quad U_H = \prod_{k=1}^{K_H} e^{-i\alpha_k \sigma^k \Delta t}, \quad (14)$$

where $\{(\alpha_k, \sigma^k)\}_k$ is the Pauli decomposition of \mathcal{H}_H as in Eq. (13). Thus, the circuit for \mathcal{M}_H consists of consecutive layers of exponentiated Pauli strings, each implementable with a standard construction of an R^z rotation on a single qubit sandwiched by CX gates and single-qubit basis changes spanning the support of the Pauli string (see Supplementary Note 2A for further details). On n qubits with nearest-neighbor qubit connectivity, this standard implementation of an exponentiated Pauli string is $\mathcal{O}(n)$ depth in the worst case.

We utilized several techniques to achieve circuits with fewer CX gates and lower depth than naïve construction. For isolated subsets of Pauli strings of weight ≤ 2 sharing the same support, we invoked KAK decomposition [83], which produces circuit components for $U(4)$ unitaries comprising 1-qubit rotations and at most 3 CX gates. For subsets of Pauli strings of weight ≤ 3 sharing the same support, we used the QSEARCH algorithm [84] in the public BQSKit toolkit [85] to produce circuit components, which promises optimal-depth synthesis for unitaries up to 4 qubits.

For remaining Pauli strings of larger weight, we used a circuit construction procedure that takes advantage of simultaneous diagonalization [86]. We partitioned the Pauli strings into commuting groups by finding a clique cover on their commutation graph². Let $\{P_k\}_k$ be one such commuting group

on n qubits; then there exists a Clifford unitary C that simultaneously diagonalizes the group, that is, $CP_kC^\dagger = Q_k$ for $Q_k \in \{\mathbb{I}, \sigma^z\}^{\otimes n}$, for all k . We solved for C and its circuit implementation, and the diagonal $\{Q_k\}_k$, through a classically efficient stabilizer-based method [86, 87]. The circuit for the exponentiated $\{P_k\}_k$ then follows the structure $C^\dagger [\prod_k \exp(-iQ_k\theta)] C$, and suitable orderings of the Q_k terms according to their support allow cascading cancellation of CX gates between neighboring terms [86]. This approach provides reductions in circuit depth and number of CX gates compared to the naïve concatenation of $\exp(-iP_k\theta)$ circuit components in practice.

Implementation of \mathcal{M}_A . We devised a scheme based on the linear combination of unitaries (LCU) circuit pattern to implement the non-unitary $e^{-\mathcal{H}_A\Delta t}$, which is equivalent to imaginary-time evolution under \mathcal{H}_A . In general, equipped with unitaries U_0, \dots, U_{d-1} controlled respectively by the $|0\rangle, \dots, |d-1\rangle$ states of an ancillary qubit register, a compact circuit primitive is known [88, 89] that probabilistically implements the action $(\gamma_0 U_0 + \dots + \gamma_{d-1} U_{d-1})$ for coefficients $\gamma_k > 0$ on a system register up to normalization of the resultant quantum state (see Figure 1d). This LCU primitive requires $\lceil \log_2 d \rceil$ ancillary qubits, and comprises an initialization unitary V on the ancillary register dependent on the coefficients, application of the controlled U_k unitaries, and V^\dagger followed by measurements on the ancillary register. The primitive succeeds when the ancillae report $|0\rangle$ upon measurement and fails otherwise.

We first establish a general method for an arbitrary Hamiltonian \mathcal{H}_A . The central idea is to approximate $e^{-\mathcal{H}_A\Delta t}$ using a linear combination of forward and backward real time-evolution. Specifically, we examine expansions of the type

$$A_0 \mathbb{I} + \sum_{b=1}^B A_b \left(e^{+i\mathcal{R}\Delta\tau_b} + e^{-i\mathcal{R}\Delta\tau_b} \right) = e^{-\mathcal{H}_A\Delta t} + \mathcal{O}\left(\frac{1}{m^\kappa}\right), \quad (15)$$

for coefficients $A_0, \dots, A_B \geq 0$, rescaled simulation times $\{\Delta\tau_b\}_b$, and a Hermitian auxiliary Hamiltonian \mathcal{R} satisfying $\mathcal{R}^2 = \mathcal{H}_A$. To satisfy error requirements of \mathcal{M}_A as declared in Eq. (12), we require an approximation order $\kappa \geq 2$. The identity \mathbb{I} and time-evolution propagators $e^{\pm i\mathcal{R}\Delta\tau_b}$ are unitary, thus their linear combination can be implemented by the LCU primitive above. In particular, the time-evolution propagators $e^{\pm i\mathcal{R}\Delta\tau_b}$ can be implemented via Lie-Trotter product formulae, in the same way as \mathcal{M}_H , and the ancillae controls for the LCU need only be added to the central R^z rotation for each exponentiated Pauli string. We refer readers to Supplementary Note 2 for elaboration on the lower-level implementation details.

For any $\kappa \geq 2$, solutions for the expansion can be identified by matching Taylor expansion terms by order on both sides of Eq. (15). In broad families of condensed-matter lattice models, either choices of Hermitian roots \mathcal{R} are known or analytical properties of the Hamiltonians enable \mathcal{R} to be efficiently computed. For example, the roots of topological insulators and superconductors in one and higher dimensions [90–93], and generalized classes of symmetry-protected topological

problem in the worst case, is not necessary for this method to work, though generally the fewer the number of cliques the smaller the resultant circuit.

² Determining the *minimum* clique cover, which is an NP-complete

or topologically ordered systems [94–99] are well-studied. In cases where \mathcal{R} is difficult or inefficient to determine, we provide also an alternative method relying only on knowledge of \mathcal{H}_A —see Supplementary Note 2B.

Minimally, choosing $d = 2$ terms in the LCU necessitates only a single ancillary qubit. This corresponds to a cosine approximation to $e^{-\mathcal{H}_A \Delta t}$ with a single pair $B = 1$ in Eq. (15), with coefficients $A_0 = 0$ and $A_1 = 1/2$, and rescaled simulation times $\Delta\tau = \sqrt{2}\Delta t$, achieving approximation order $\kappa = 2$. Solutions with larger number of terms d achieving higher approximation order κ can readily be found—see Supplementary Table S6 for examples.

In the present edge burst context, Hermitian auxiliary Hamiltonians \mathcal{R}^{eb} satisfying $(\mathcal{R}^{\text{eb}})^2 = \mathcal{H}_A$ can be found analytically. However, more carefully exploiting the structure of $\mathcal{H}_A^{\text{eb}}$ in fact allows a solution to Eq. (15) with zero approximation error (effectively $\kappa \rightarrow \infty$). As $\mathcal{H}_A^{\text{eb}}$ comprises only on-site terms, we find

$$e^{-\mathcal{H}_A^{\text{eb}} \Delta t} = \sum_{x=1}^N (n_{xa} + e^{-\gamma \Delta t} n_{xb}) = \frac{1}{2\eta} (U_+^{\text{eb}} + U_-^{\text{eb}}), \quad (16)$$

for forward and backward time-evolution unitaries $U_{\pm}^{\text{eb}} = e^{\pm i \mathcal{H}_{\text{aux}}^{\text{eb}}}$ on the effective Hermitian Hamiltonian

$$\mathcal{H}_{\text{aux}}^{\text{eb}} = \arccos\left(e^{-\gamma|\Delta t|}\right) \begin{cases} \sum_{x=1}^N n_{xb} & \Delta t \geq 0, \\ \sum_{x=1}^N n_{xa} & \Delta t < 0, \end{cases} \quad (17)$$

and scaling factor $\eta = \min(1, e^{\gamma \Delta t})$. Here we present solutions for both $\Delta t \geq 0$ and $\Delta t < 0$ cases for completeness. Thus an exact LCU construction to implement $e^{-\mathcal{H}_A^{\text{eb}} \Delta t}$ is a priori known. We use this solution in our experiments, with U_{\pm}^{eb} implemented via first-order Trotter-Lie product formula.

Qubit reset and re-use. We performed mid-circuit reset of the ancillary qubit, used in the LCU circuit implementation of the \mathcal{M}_A map (see above), to the $|0\rangle$ state after each time step such that the same qubit is re-used over the entire time-evolution experiment. Each reset is performed by executing an X gate on the qubit conditioned on the outcome of the measurement in the preceding \mathcal{M}_A circuit component. The mid-circuit readout and feedforward capability of the quantum processors [100–102] enable this resource-saving measure.

Quantum state normalization. Quantum states on a quantum computer are normalized by nature of the platform. Above, we described the implementation of normalized time-evolution of an initial state [Eq. (10)]. However, in some simulation settings, as in the present edge burst context, the process of interest is time-evolution without normalization,

$$\omega_0 \rightarrow \omega_t = e^{-i\mathcal{H}t} \omega_0 e^{+i\mathcal{H}^\dagger t}, \quad (18)$$

where $\omega_0 = \rho_0$ is a normalized initial state but ω_t is not normalized, $\text{tr}(\omega_t) \neq 1$. Enforcing normalization $\mathcal{N}(\omega_t) = \rho_t$ produces the normalized time-evolution in Eq. (10), which is realized on the quantum platform. Here we examine the recovery of ω_t from ρ_t . In particular, we describe two methods of recovering the quantum state normalization factor $A_t = \sqrt{\text{tr}(\omega_t)} > 0$ such that $\omega_t = A_t^2 \rho_t$.

The first method is general for any lossy \mathcal{H} and $t \geq 0$ such that $\|e^{-i\mathcal{H}t}\| \leq 1$, and works by examining the success probability S_t of the normalized time-evolution algorithm (as

detailed above). In each time step, failure of the algorithm can occur, which is detected by a $|1\rangle$ measurement outcome on the ancillary qubit, and indicates an incorrect projection of the quantum state that realizes a complementary action $\mathbb{I} - e^{-\mathcal{H}_A \Delta t}$ instead of the desired $e^{-\mathcal{H}_A \Delta t}$. The decrease of quantum state norm over time directly manifests in the probability of success, in particular, $A_t^2 \approx S_t$. Thus S_t measured in experiments directly allow recovery of A_t , up to errors in circuit construction (*e.g.* trotterization and LCU approximation) and hardware noise that distort the observed S_t . See Supplementary Note 4C for technical elaboration and experimental investigation.

The second method is through time-integration of site-resolved occupancy data, as described in the main text. As \mathcal{H}^{eb} is lossy on b -sublattices, we obtain

$$\frac{d}{dt} \text{tr}(\omega_t) = -2 \left\langle \mathcal{H}_A^{\text{eb}} \right\rangle_{\omega_t} = -2\gamma A_t^2 \sum_{x=1}^N \langle n_{xb} \rangle_{\rho_t}, \quad (19)$$

where $\langle n_{xb} \rangle_{\rho_t} = \text{tr}(\rho_t n_{xb})$ is the occupancy of sublattice b of unit cell x as measured on the ρ_t state on the quantum platform. This is a restatement of Eq. (3) of the main text. At the same time, by definition of A_t , $(d/dt) \text{tr}(\omega_t) = (d/dt) A_t^2 \text{tr}(\rho_t) = 2A_t (dA_t/dt)$. Thus we have

$$\frac{dA_t}{dt} = -\gamma A_t \sum_{x=1}^N \langle n_{xb} \rangle_{\rho_t}, \quad (20)$$

with the solution for A_t reported in Eq. (6). Thus A_t can be recovered through numerical integration of b -sublattice occupancies measured on normalized time-evolved states in experiments, sampled over the time domain $[0, t]$. This is the method used in all our experiments discussed in the main text (Figures 2 to 6) as well as Supplementary Figures S2 to S5.

Escape probabilities. As \mathcal{H}^{eb} is lossy on b -sublattices, as reported in Eq. (4), the probability of escape from unit cell x by time t is given by

$$P_x(t) = 2\gamma \int_0^t \langle n_{xb} \rangle_{\omega_\tau} d\tau = 2\gamma \int_0^t A_\tau^2 \langle n_{xb} \rangle_{\rho_\tau} d\tau, \quad (21)$$

where A_τ are quantum state normalization factors recovered from experiment data and $\langle n_{xb} \rangle_{\rho_\tau}$ are b -sublattice occupancies on normalized time-evolved states measured in experiments. The total escape probability across all unit cells is $P(t) = \sum_{x=1}^N P_x(t)$ accordingly. Note $P_x(0) = P(0) = 0$, and that $P_x(t)$ and $P(t)$ are non-decreasing with t . In the long-time limit, each $P_x(t)$ approaches an asymptotic (*i.e.* steady-state) value $\mathcal{P}_x = \lim_{t \rightarrow \infty} P_x(t)$, and $P(\infty) = 1$ as expected of a properly normalized probability distribution, consistent with Ref. [21].

The dynamics of the system tends to completion as $P(t) \rightarrow 1$, and there is no further purpose in assessing dynamics at larger times which contribute negligibly to escape probabilities. We terminate time-evolution at t sufficiently large to achieve $P(t) \gtrsim 0.995$ in our experiments, more than sufficient to clearly observe edge burst phenomenology as demonstrated.

Measuring imaginary energy gap. Time-evolution by \mathcal{H} as written in Eq. (10) encodes an effective imaginary-time evolution with respect to the anti-Hermitian component of \mathcal{H} in the following sense. Suppose $|\phi\rangle$ is a (right) eigenstate of

\mathcal{H} with eigenenergy $E \in \mathbb{C}$, that is, $\mathcal{H}|\phi\rangle = E|\phi\rangle$. Then

$$\begin{aligned} e^{-i\mathcal{H}t}|\phi\rangle &= e^{-iEt}|\phi\rangle = e^{-i\operatorname{Re}(E)t}e^{i\operatorname{Im}(E)t}|\phi\rangle, \\ \frac{\|e^{-i\mathcal{H}t}|\phi\rangle\|}{\|\phi\|} &= e^{\operatorname{Im}(E)t}. \end{aligned} \quad (22)$$

Let us consider the time-evolution of an initial state ρ_0 which comprises a mixture of eigenstates of \mathcal{H} . Then for $t > 0$ ($t < 0$), the amplitudes of all other eigenstates become exponentially damped compared to the eigenstate with the largest (smallest) $\operatorname{Im}(E)$. Thus, for sufficiently large $|t|$, the time-evolved state ρ_t purifies to an eigenstate of extremal $\operatorname{Im}(E)$; the required $|t|$ can be estimated by demanding that $P(t)$ converges close to unity (see [above](#)). After time-evolution, the eigenenergy E can be measured through standard techniques. We used Hamiltonian averaging [[103–105](#)] in our experiments,

$$\operatorname{Im}(E) = -\langle \mathcal{H}_A \rangle_{\rho_t} = -\sum_{k=1}^{K_A} \beta_k \langle \chi^{(k)} \rangle_{\rho_t}, \quad (23)$$

where as before $\langle O \rangle_{\rho_t} = \operatorname{tr}(\rho_t O)$ is the measured expectation value of an observable O on ρ_t on the quantum device. As $\chi^{(k)}$ are Pauli strings, measuring their expectation values on a quantum processor involves only Clifford basis changes before computational-basis readouts. To reduce the number of circuits required, commuting subsets of $\{\chi^{(k)}\}_k$ can be measured simultaneously on the same circuit, with the joint Clifford basis change given by an efficient stabilizer-based method [[87](#)].

We are interested in the imaginary energy (*i.e.* dissipative) gap in the present work, which is open when the largest $\operatorname{Im}(E) < 0$ and closed otherwise. We took the initial state $\rho_0 = \mathcal{N}(\mathbb{I})$ to be the maximally mixed state, equivalently the infinite-temperature Gibbs state, prepared through a single round of mid-circuit computational-basis measurements on system qubits initialized in $|+\rangle$ states, whose outcomes are discarded (see Supplementary Figure [S1](#) for circuit schematic).

Circuit recompilation. We follow the formulation established in prior works, in particular Refs. [[43–45](#), [56](#), [106–108](#)]. Circuit recompilation is performed using a circuit ansatz whose parameters are dynamically optimized. We use an ansatz comprising an initial layer of single-qubit rotations (U_3 gates) on all qubits followed by $K \leq 20$ ansatz layers, each comprising a layer of CX gates entangling adjacent qubits and a layer of U_3 rotations (see Supplementary Figure [S1](#)). Each U_3 gate in the ansatz is associated with rotation angles (θ, ϕ, λ) ; we collate them into a parameter vector ϑ . Then, given a target circuit component unitary V and an initial state $|\psi_0\rangle$, the optimization problem

$$\operatorname{argmax}_{\vartheta} \mathcal{F}(V_{\vartheta}|\psi_0, V|\psi_0) = \operatorname{argmax}_{\vartheta} \left| \langle \psi_0 | V_{\vartheta}^{\dagger} V | \psi_0 \rangle \right|^2, \quad (24)$$

is numerically treated, where V_{ϑ} is the circuit ansatz unitary with parameters ϑ . The recompiled circuit component is then the ansatz with optimal parameters fixed. As \mathcal{H}^{eb} is number-conserving, to enhance recompilation performance and the quality of recompiled circuits, we focus optimization on the Fock sectors relevant to the time-evolution simulation [[43](#)]. In our implementation, we estimate V_{ϑ} through auto-differentiable tensor network-based ansatz simulation [[109](#)], and use L-BFGS-B with basin-hopping to perform the optimization [[110](#)]. Recompilation is set to never exceed a few minutes per circuit.

Readout error mitigation. The quantum devices used in our experiments present non-negligible probabilities ($\sim 1\text{--}3\%$) of reporting a $|1\rangle$ outcome when the measured qubit is in $|0\rangle$ and vice versa, typical for current-era quantum hardware. This is referred to as readout error and is caused, for example, by ambiguity in microwave signal characteristics (*i.e.* IQ data) that inhibit classification of measurement outcomes. We mitigated the effect of these errors by characterizing the measurement bit-flip probabilities of the qubits used, then performing linear inversion to approximately recover the true measurement counts from observed measurement counts [[111–113](#)]. Unlike prior works [[43–45](#), [111–113](#)], our experiment circuits contain mid-circuit measurements—in particular a qubit can be measured multiple times throughout the circuit. We thus employed a modified scheme as described below.

Consider an experiment circuit containing measurements on n qubits, labeled by $[n]$, containing L layers of measurements. The set of qubits measured in layer l is $\mathcal{I}_l \subseteq [n]$, of size $p_l = |\mathcal{I}_l|$, and the total number of measurements over all layers is $p \geq n$. The measurement outcomes of each shot of the circuit form a bitstring $x \in \{0, 1\}^p$, where entry x_j records the outcome of the j^{th} measurement in the circuit. Upon completion of a specified number of shots, a raw counts vector \mathbf{c} is returned, where entry c_x records the number of times the bitstring x was observed.

We assume that there are no correlations in readout errors for measurements in different layers as these measurements are separated in time, consistent with standard Markovian assumptions on noise channels [[114](#), [115](#)]; but within the same layer we accommodate arbitrary correlations. Let M be the readout calibration matrix on the n qubits, where each entry M_{st} records the probability of obtaining outcome $s \in \{0, 1\}^n$ upon measurement of the qubits when the true outcome is $t \in \{0, 1\}^n$. Then \mathbf{c} and the ideal counts $\tilde{\mathbf{c}}$ that would hypothetically be observed without readout errors are related by

$$\mathbf{c} = \left(\bigotimes_{l=1}^L M[\mathcal{I}_l] \right) \tilde{\mathbf{c}} \iff \tilde{\mathbf{c}} = \left(\bigotimes_{l=1}^L M[\mathcal{I}_l]^{-1} \right) \mathbf{c}, \quad (25)$$

where $M[\mathcal{I}_l]$ is M with support retained over the qubits \mathcal{I}_l of layer l but marginalized over the remaining qubits, that is,

$$M[\mathcal{I}_l]_{st} = \frac{1}{2^{n-p_l}} \sum_{\substack{s' \in \{0, 1\}^n \\ s'[\mathcal{I}_l] = s}} \sum_{\substack{t' \in \{0, 1\}^n \\ t'[\mathcal{I}_l] = t}} M_{s't'}, \quad (26)$$

where $s[\mathcal{I}_l]$ denotes the substring formed by entries of a bitstring s at qubit indices \mathcal{I}_l . Thus Eq. (25) enables the recovery of ideal counts $\tilde{\mathbf{c}}$ from raw counts \mathbf{c} . To ensure that the mitigated counts $\tilde{\mathbf{c}}$ are physical, we employed an additional step of projecting $\tilde{\mathbf{c}}$ onto the nearest non-negative probability distribution (in l_2 -norm) [[116](#)].

The matrix M can be characterized by running calibration circuits, which prepare the n qubits in state $|t\rangle$ for every $t \in \{0, 1\}^n$ and record probabilities of observing each outcome $s \in \{0, 1\}^n$ upon measurement. However, this direct method requires 2^n calibration circuits and is prohibitively costly for large n . We instead employed a tensored approach [[43–45](#)], which splits the n qubits into sub-registers containing $\{n_g\}_g$ qubits and assumes that readout errors are uncorrelated between sub-registers. The calibration is performed for each sub-register, producing matrices $\{M^{(g)}\}_g$, and the overall $M = \bigotimes_g M^{(g)} \iff M^{-1} = \bigotimes_g M^{(g)-1}$. Then, performing

linear inversion as in Eq. (25), each $M^{(g)-1}$ can act sector-wise on \mathbf{c} , avoiding the cost of assembling the entire M^{-1} . Moreover, the calibration circuits for different sub-registers can be merged as they act on disjoint sets of qubits; thus this approach requires $2^{\max_g n_g} \ll 2^n$ calibration circuits. We chose sub-registers such that $n_g \leq 5$ in our experiments.

While the employed readout error mitigation addresses errors in the measurement outcome statistics, it does not address errors occurring in feedforward—for example, a faulty mid-circuit measurement outcome on an ancillary qubit in our circuits can cause an incorrect reset (see [above](#)). A recent work by several of the authors presented a protocol that overcomes this limitation [117] but some experiments in this study predate this development; we do not use this protocol here.

Dynamical decoupling. Idle periods on qubits are invariably present in our experiment circuits, as a qubit may need to wait for gates to complete on other qubits before being involved in 2-qubit operations with them. During idle periods, qubits are still subject to decoherence (*e.g.* dephasing noise and thermal relaxation). Dynamical decoupling [118], which runs through alternating basis changes that multiply to the identity, can be used to suppress the effects of such decoherence. At a basic level, dynamical decoupling refocuses the dephasing experienced by the qubits such that the accumulated noise contributions cancel to a certain order.

We employed the common XY4 pulse sequence [118, 119] for dynamical decoupling in our experiments. The sequence is inserted for idle periods not exceeding the equivalent of 2 CX gate durations (~ 800 – 1000 ns); for longer idle durations repetitions of the sequence are inserted. While there exist more sophisticated dynamical decoupling sequences that cancel noise to higher orders [120, 121], empirical results [122] suggest that simple sequences (*e.g.* XY4) can be more performant in practice, due to the presence of errors on the gates introduced by the sequence and differences between hardware noise backgrounds and theoretical assumptions.

Pauli twirling. We applied randomized twirling of CXs on each experiment circuit. Each CX gate in the circuit is replaced by $P_1(\text{CX})P_2$, where (P_1, P_2) are randomly drawn Paulis such that the action of the twirled CX remains invariant. See Supplementary Table S5 for a complete list of (P_1, P_2) pairs used. In general, the twirling of gates in circuits, also referred to as randomized compiling in literature [123, 124], has the effect of converting coherent and non-Markovian error sources into stochastic errors which can be averaged over in an experiment. Pauli twirling, in particular, converts error processes into diagonal Pauli channels [125]. We used Pauli twirling in conjunction with zero-noise extrapolation.

Zero-noise extrapolation. A general method for mitigating inaccuracy of expectation values due to hardware noise is zero-noise extrapolation (ZNE), which functions by collecting additional data at amplified noise levels and then extrapolating into the zero-noise limit [40, 125–128]. We employ a gate-level implementation of ZNE in our experiments; alternative pulse-level methods have been explored in the literature [112, 129]. Our procedure was as follows. For an experiment measuring a set of observables $\{O_k\}_k$, we perform repetitions at noise amplification factors $1 = \lambda_1 < \lambda_2 < \dots < \lambda_r$, where $\lambda = 1$ corresponds to the unmodified experiment. Noise in an experiment is amplified by randomized local gate folding [127], that is, each gate G in each circuit is probabilistically replaced by $GG^\dagger G$, such that the total number of 1- and

2-qubit gates in the circuit is each increased by factor $\lambda > 1$. Note that G^\dagger is known for all basis gates (*e.g.* the Paulis and CX are involutory), so compilation of the folded circuits is straightforward. To illustrate, $\lambda = 3$ folds every gate in each circuit, $1 < \lambda < 3$ contains a mixture of folded and unfolded gates, and $\lambda > 3$ can be reached by repeated folding.

Let $\langle O_k^{(\lambda)} \rangle$ denote $\langle O_k \rangle$ measured on hardware at noise amplification factor λ . We assume an affine relation between $\langle O_k^{(\lambda)} \rangle$ and λ , that is, $\langle O_k^{(\lambda)} \rangle \approx m_k \lambda + c_k$ for gradient m_k and zero-noise intercept c_k , which enables a simple formulation of the extrapolation problem. This linearization is valid for λ not too large, such that hardware noise does not saturate measured observables. We treat the least-squares regression

$$(\mathbf{m}^*, \mathbf{c}^*) = \underset{\mathbf{m}, \mathbf{c}}{\operatorname{argmin}} \sum_k \sum_{\gamma=1}^r \left(m_k \lambda_\gamma + c_k - \langle O_k^{(\lambda_\gamma)} \rangle \right)^2, \quad (27)$$

and the zero-noise estimates $\{\langle O_k^{(0)} \rangle\}_k$ are then given by the intercepts $\{c_k^*\}_k$. We additionally impose constraints on (\mathbf{m}, \mathbf{c}) based on $\{O_k\}_k$ to ensure physicality of regression results. In particular, for experiments in the p -particle Fock sector measuring site-resolved occupancies, that is $\{O_k\}_k = \{n_{x\ell}\}_{x\ell}$, we imposed number conservation and hardcore bosonic statistics, such that $0 \leq \langle n_{x\ell} \rangle \leq 1$ for all sites and the sum of occupancies equaled p , at all noise levels on the regression lines. For experiments measuring the imaginary energy in the p -particle sector, that is $\{O_k\}_k = \{\mathcal{H}_A^{\text{eb}}\}$, we imposed $\langle \mathcal{H}_A^{\text{eb}} \rangle \leq 0$ as \mathcal{H}^{eb} is lossy and $-p\gamma \leq \langle \mathcal{H}_A^{\text{eb}} \rangle$ by the variational principle. These constraints translate into conditions on (\mathbf{m}, \mathbf{c}) —see Supplementary Note 3.

The constrained regression is convex and can be solved using standard techniques with guaranteed optimal solutions [130]. In our experiments, we chose $(\lambda_1, \dots, \lambda_r) = (1, 1.25, 1.5, 1.75, 2)$ and used the general-purpose operator-splitting quadratic program (OSQP) solver [131] to perform the constrained regressions. For each experiment circuit at each λ , we produced 16 gate-folded circuits, each further compiled with an independent instance of randomized Pauli twirling (see [above](#)). Each set of 16 circuits were executed on hardware and their results averaged, to produce the $\langle O_k^{(\lambda)} \rangle$ expectation value for regression. See Supplementary Note 3 for further technical details and discussion.

Qubit selection. The quantum devices we utilized have more qubits than needed for our experiments, and there is variation in qubit error rates on each device (see Supplementary Table S4 for device performance characteristics). We hence used a search procedure to select qubits of the lowest estimated error to use in our simulations, following the demonstrated methods in Refs. [32, 43–45, 132, 133]. Given an experiment circuit \mathcal{C} requiring n qubits and the connectivity graph of 2-qubit couplings (CX, ECR, or CZ) on the device, we identified all distinct qubit chains \mathcal{X} of length n on the device, and for each chain $x \in \mathcal{X}$ computed an estimated circuit error $\mathcal{E}_x[\mathcal{C}]$ by summing the calibrated gate errors of each gate in \mathcal{C} . We selected the qubit chain x that minimized $\mathcal{E}_x[\mathcal{C}]$. This selection procedure is approximate, as the gate error rates are obtained from routine (\sim daily) calibration of the quantum devices and are subject to drift over time, and the circuit error estimation $\mathcal{E}_x[\mathcal{C}]$ is not exact.

Interacting Non-Hermitian Edge and Cluster Bursts on a Digital Quantum Processor (Supplementary Information)

Jin Ming Koh ^{1,2} Wen-Tan Xue ³ Tommy Tai ⁴ Dax Enshan Koh ^{2,5,6} and Ching Hua Lee ^{3,*}

¹*Department of Physics, Harvard University, Cambridge, Massachusetts 02138, USA*

²*Quantum Innovation Centre (Q.InC), Agency for Science, Technology and Research (A*STAR),
2 Fusionopolis Way, Innovis #08-03, Singapore 138634, Republic of Singapore*

³*Department of Physics, National University of Singapore, Singapore 117542, Republic of Singapore*

⁴*Department of Physics, Massachusetts Institute of Technology, Cambridge, Massachusetts 02142, USA*

⁵*Institute of High Performance Computing (IHPC), Agency for Science, Technology and Research (A*STAR),
1 Fusionopolis Way, #16-16 Connexis, Singapore 138632, Republic of Singapore*

⁶*Science, Mathematics and Technology Cluster, Singapore University of Technology and Design,
8 Somapah Road, Singapore 487372, Republic of Singapore*

CONTENTS

List of Figures	1
List of Tables	2
1. Further details on model and time-dynamics	6
A. Symmetries and equivalences of the quantum ladder Hamiltonian	6
B. Speed limit on energy variation during non-Hermitian time-evolution	6
2. Further details on quantum simulation methods	8
A. Implementation of uncontrolled and coherently controlled multi-qubit Pauli rotations	8
B. Implementation of \mathcal{M}_A map and time steps	9
a. An effective square root of \mathcal{H}_A is known or efficiently computable	9
b. Circuit depth reduction by merging pairs of time steps	10
c. Higher-order implementations of \mathcal{M}_A via many-term LCUs	11
d. An effective square root of \mathcal{H}_A is not known	11
3. Further details on error suppression and mitigation methods	15
A. Zero-noise extrapolation with physicality constraints	15
a. Amplifying noise through local gate folding	16
b. Randomizing coherent errors through Pauli twirling	16
4. Additional Results	17
A. Additional experiment results on the canonical edge burst	17
B. Spatially extended edge bursts with multiple interacting particles	20
C. Alternative recovery of quantum state norm from algorithm success probability	22
References	23

LIST OF FIGURES

S1 Detailed quantum simulation circuit structures and components	14
S2 Canonical edge burst on $N = 8$ quantum ladder with different initial particle localization	18
S3 Canonical edge burst on a smaller $N = 4$ quantum ladder	19
S4 Additional results with two interacting particles	20

* phylch@nus.edu.sg

S5	Spatially extended and ordered edge bursts with three interacting particles	21
S6	Comparison between quantum state norm recovery methods	22

LIST OF TABLES

S1	Pauli decompositions of $\mathcal{H}_0^{\text{eb}}$ Hamiltonian	3
S2	Hamiltonian \mathcal{H}^{eb} parameter values used in experiments and other specifications	3
S3	Superconducting quantum devices used in experiments.	4
S4	Performance characteristics of quantum devices used in experiments	4
S5	Operator pairs P_1 and P_2 used for Pauli twirling	5
S6	Higher-order linear combination of unitaries expansions for \mathcal{M}_A	11

$N = 4$			$N = 8$		
Component	Pauli String	Coefficient	Component	Pauli String	Coefficient
\mathcal{H}_H	IIX	v_1	\mathcal{H}_H	IIIX	v_1
	IXX	$v_2/2$		IIXX	$v_2/2$
	IYZ	$v_2/2$		IIYZ	$v_2/2$
	XXX	$v_2/4$		IXXX	$v_2/4$
	XYZ	$-v_2/4$		IXYZ	$-v_2/4$
	YYZ	$v_2/4$		IYXZ	$v_2/4$
\mathcal{H}_A	YYX	$v_2/4$		IYYX	$v_2/4$
	III	$\gamma/2$		XXXX	$v_2/8$
\mathcal{H}_A	IIZ	$-\gamma/2$		XXYZ	$-v_2/8$
				XYXZ	$-v_2/8$
			YYXZ	$-v_2/8$	
			YXXZ	$v_2/8$	
			YXYX	$v_2/8$	
			YYXX	$v_2/8$	
			YYYZ	$-v_2/8$	
			\mathcal{H}_A	IIII	$\gamma/2$
				IIIZ	$-\gamma/2$

Supplementary Table S1. Explicit Pauli decompositions of $\mathcal{H}_0^{\text{eb}}$ Hamiltonian in the single-particle ($p = 1$) sector at $N = 4$ and $N = 8$ unit cells, given for illustration. Above v_1, v_2 are tight-binding hopping coefficients and γ is an on-site loss rate—see Eq. (1) of main text or Eq. (7) of Methods. The general forms of Pauli decompositions of \mathcal{H}_H and \mathcal{H}_A components are written in Eq. (13) of Methods and used consistently thereafter in the description of our algorithms.

Experiment	N	p	Regime	v_1	v_2	γ	U_r	Init. Locs. $\{x_0\}$
Supplementary Figure S3a–S3d	4	1	Edge burst	0.4	0.5	0.5	-	{3}
Supplementary Figure S3e	4	1	Trivial	1	0.5	0.5	-	{3}
Main Figure 2a–d	8	1	Edge burst	0.4	0.5	0.5	-	{6}
Main Figure 2e	8	1	Trivial	1	0.5	0.5	-	{6}
Supplementary Figure S2a–S2d	8	1	Edge burst	0.4	0.5	0.5	-	{4}
Supplementary Figure S2e	8	1	Edge burst	1	0.5	0.5	-	{4}
Main Figure 3a, 3c	64	1	Edge burst	0.4	0.5	1	-	{51}
Main Figure 3b, 3c	64	1	Trivial	1	0.5	1	-	{51}
Main Figure 4b	16	1	Variable	[0, 1]	0.5	0.5	-	$\beta = 0$ Gibbs
Main Figure 5a	12	2	Edge burst*	0.4	0.5	1	$U_r = 3 \forall r \in [1]$	{10, 12}
Main Figure 5b	12	2	Trivial	0.7	0.5	1	$U_r = 3 \forall r \in [1]$	{10, 12}
Main Figure 5c, Supplementary Figure S6a	14	2	Edge burst*	0.4	0.5	1	$U_r = 3 \forall r \in [3]$	{11, 14}
Supplementary Figure S4a, S6b	14	2	Trivial*	0.7	0.5	1	$U_r = 3 \forall r \in [3]$	{11, 14}
Main Figure 5d	14	2	Edge burst*	0.4	0.5	1	$U_r = 3 \forall r \in [5]$	{10, 14}
Supplementary Figure S4b	14	2	Trivial*	0.7	0.5	1	$U_r = 3 \forall r \in [5]$	{10, 14}
Main Figure 6a	14	2	Edge burst*	0.4	0.5	1	$U_r = 2 \forall r \in [1]$	{8, 9}
Main Figure 6b	14	2	Trivial*	0.7	0.5	1	$U_r = 2 \forall r \in [1]$	{8, 9}
Main Figure 6c	14	2	Edge burst*	0.4	0.5	1	$U_r = 2 \forall r \in [3]$	{8, 9}
Main Figure 6d	14	2	Trivial*	0.7	0.5	1	$U_r = 2 \forall r \in [3]$	{8, 9}
Supplementary Figure S5a	13	3	Edge burst*	0.375	0.5	1	$U_r = 5 \forall r \in [1]$	{9, 11, 13}
Supplementary Figure S5b	13	3	Trivial*	0.6	0.5	1	$U_r = 5 \forall r \in [1]$	{9, 11, 13}
Supplementary Figure S5c	17	3	Edge burst*	0.375	0.5	1	$U_r = 5 \forall r \in [3]$	{11, 14, 17}
Supplementary Figure S5d	17	3	Trivial*	0.6	0.5	1	$U_r = 5 \forall r \in [3]$	{11, 14, 17}
Supplementary Figure S5e	20	3	Edge burst*	0.375	0.5	1	$U_r = 5 \forall r \in [5]$	{12, 16, 20}
Supplementary Figure S5f	20	3	Trivial*	0.6	0.5	1	$U_r = 5 \forall r \in [5]$	{12, 16, 20}

Supplementary Table S2. Values of hopping coefficients v_1, v_2 , on-site loss rate γ , and interaction amplitudes U_r parametrizing the non-Hermitian Hamiltonian \mathcal{H}^{eb} used in experiments. Also listed are the number of unit cells N (the number of sites on the ladder is accordingly $2N$), number of bosons p , and initial boson localization used in the experiments. For ease of interpretation we label regimes canonically supporting the non-Hermitian edge burst as “Edge burst” ($v_1/v_2 \leq 1$) and regimes that do not as “Trivial” ($v_1/v_2 > 1$). The * mark denotes that the experiment involves multiple interacting bosons and is beyond the canonical setting of the non-Hermitian edge burst (*i.e.* single-particle non-interacting).

Experiment	Devices Used
Supplementary Figure S3	<i>ibm_hanoi</i>
Main Figure 2a–e, Supplementary Figure S2	<i>ibm_hanoi, ibmq_mumbai</i>
Main Figure 3a–c	<i>ibm_sherbrooke, ibm_osaka, ibm_kyoto</i>
Main Figure 4b	<i>ibm_hanoi, ibmq_mumbai, ibm_osaka</i>
Main Figure 5a–d, Supplementary Figure S4, S6	<i>ibm_osaka, ibm_kyoto, ibm_nazca</i>
Main Figure 6a–d	<i>ibm_torino, ibm_osaka, ibm_kyoto, ibm_nazca</i>
Supplementary Figure S5	<i>ibm_sherbrooke, ibm_osaka, ibm_kyoto, ibm_nazca</i>

Supplementary Table S3. Superconducting quantum devices used in experiments.

Device	Qubits	2Q Gate	1Q Gate Error ($\times 10^{-4}$)			2Q Gate Error ($\times 10^{-3}$)			Readout Error ($\times 10^{-2}$)		
			10%	90%	Med.	10%	90%	Med.	10%	90%	Med.
<i>ibm_torino</i>	133	CZ	1.77	9.50	3.06	2.44	13.5	4.62	0.89	5.84	2.01
<i>ibm_sherbrooke</i>	127	ECR	1.39	6.24	2.25	4.55	15.0	7.42	0.51	5.01	1.15
<i>ibm_osaka</i>	127	ECR	1.23	12.5	2.41	4.03	19.3	7.15	0.65	8.94	1.99
<i>ibm_kyoto</i>	127	ECR	1.46	10.5	2.68	4.56	19.4	8.01	0.61	8.15	1.51
<i>ibm_nazca</i>	127	ECR	1.90	8.74	3.15	6.00	24.2	10.7	0.87	7.65	2.67
<i>ibm_hanoi</i>	27	CX	1.55	6.02	2.18	4.40	16.1	7.60	0.67	3.19	1.09
<i>ibmq_mumbai</i>	27	CX	1.58	3.75	2.08	5.66	11.5	7.52	1.24	5.87	1.70

Device	1Q Gate Time (ns)	Readout Time (ns)	2Q Gate Times (ns)			T_1 (μ s)			T_2 (μ s)		
			10%	90%	Med.	10%	90%	Med.	10%	90%	Med.
<i>ibm_torino</i>		1560	84.0	124	84.0	62.3	250	171	42.5	220	125
<i>ibm_sherbrooke</i>	56.9	1244	533	533	533	157	379	273	48.7	321	183
<i>ibm_osaka</i>	60.0	1400	660	660	660	127	396	275	19.8	322	151
<i>ibm_kyoto</i>	60.0	1400	660	660	660	124	320	223	28.2	237	115
<i>ibm_nazca</i>	60.0	4000	660	660	660	115	286	194	32.8	239	136
<i>ibm_hanoi</i>	32.0	818	242	576	348	68.8	194	142	25.1	284	132
<i>ibmq_mumbai</i>	35.6	3513	277	640	405	54.6	130	108	58.4	251	149

Supplementary Table S4. Performance characteristics of quantum devices used in experiments. For quantities that vary between qubits on the same device, we provide 10th and 90th percentile and median values evaluated over all qubits on the device. Characteristics summarized here are based on routine (\sim daily) calibration data of the machines, retrieved over a duration of four weeks in the middle of experiments.

P_1	P_2
II	II
IX	IX
IY	ZY
IZ	ZZ
XI	XX
XX	XI
XY	YZ
XZ	YY
YI	YX
YX	YI
YY	XZ
YZ	XY
ZI	ZI
ZX	ZX
ZY	IY
ZZ	IZ

Supplementary Table S5. List of operator pairs P_1 and P_2 used for Pauli twirling. Each CX gate in an experiment circuit to be twirled is replaced by $P_1(\text{CX})P_2$ for (P_1, P_2) randomly drawn from the list above, such that the action of the twirled CX remains invariant. See [Methods](#) for methodological details.

Supplementary Note 1: Further details on model and time-dynamics

A. Symmetries and equivalences of the quantum ladder Hamiltonian

The quantum ladder model examined in our study, which we described in Eqs. (1)–(2) of the main text and Eq. (7) of [Methods](#), possesses a U(1) number-conserving symmetry in the hardcore boson species. Explicitly, the Hamiltonian \mathcal{H}^{eb} is invariant under the rotation $c_{x\ell} \rightarrow e^{i\phi} c_{x\ell}$ and $c_{x\ell}^\dagger \rightarrow e^{-i\phi} c_{x\ell}^\dagger$ for any $\phi \in \mathbb{R}$ across all unit cells $x \in [1, N]$ and sublattice $\ell \in \{a, b\}$ on the ladder. This implies that the total particle number is a conserved quantity under time-evolution (*i.e.* is a constant of motion). This number conservation is discussed and made use of in numerous places, for example as a physical constraint for error mitigation, as described in the main text and [Methods](#).

The non-interacting $\mathcal{H}_0^{\text{eb}}$ possesses additional symmetries that constrain its complex spectrum. Here, it is most convenient to consider the Bloch Hamiltonian without the imaginary loss term, $\overline{\mathcal{H}}_0^{\text{eb}}(k) = \mathcal{H}_0^{\text{eb}}(k) + i\gamma\mathbb{I}/2$, where the Bloch Hamiltonian $\mathcal{H}_0^{\text{eb}}(k)$ was given in Eq. (1) of the main text. Then we note the following symmetries,

- Chiral symmetry characterized by $\tau^y \overline{\mathcal{H}}_0^{\text{eb}}(k) \tau^y = -\overline{\mathcal{H}}_0^{\text{eb}}(k)$, which implies that the spectrum of $\overline{\mathcal{H}}_0^{\text{eb}}$ is inversion-symmetric, that is, eigenenergies come in pairs $(+E, -E)$.
- Time-reversal symmetry characterized by $\tau^x \overline{\mathcal{H}}_0^{\text{eb}}(-k) \tau^x = -\overline{\mathcal{H}}_0^{\text{eb}}(k)^\dagger$, which implies that the spectrum of $\overline{\mathcal{H}}_0^{\text{eb}}$ is reflection-symmetric about the real axis, that is, eigenenergies come in pairs (E, E^*) .

Above, τ^x, τ^y, τ^z are Pauli operators acting in the sublattice pseudospin space. Together, these constrain the complex spectrum of $\mathcal{H}_0^{\text{eb}}$ to be reflection-symmetric about both the $\text{Re}(E) = 0$ and $\text{Im}(E) = -\gamma/2$ lines, as observed in [Figures 4b–c](#) of the main text.

Lastly, as mentioned in the main text, the non-interacting quantum ladder model $\mathcal{H}_0^{\text{eb}}$ is unitarily equivalent to the non-Hermitian Su–Schrieffer–Heeger (SSH) model [[1](#), [2](#)] with left-right asymmetric hoppings. Explicitly, the transformation $R_{\text{SSH}}^\dagger \mathcal{H}_0^{\text{eb}}(k) R_{\text{SSH}}$ with the unitary pseudospin rotation $R_{\text{SSH}} = e^{-i\pi\sigma^x/4}$ maps $\mathcal{H}_0^{\text{eb}}(k)$ onto the canonical non-Hermitian SSH model [[3](#)] with intercell hopping v_2 and asymmetric intracell hoppings $v_1 \pm \gamma/2$. This equivalence immediately establishes the presence of the non-Hermitian skin effect (NHSE) on the quantum ladder model. A non-unitary similarity transformation involving site-dependent rescaling can map the quantum ladder model onto the Hermitian SSH model [[2](#)].

B. Speed limit on energy variation during non-Hermitian time-evolution

As mentioned in the discussion of [Section II G](#) of the main text, while a time-independent non-Hermitian Hamiltonian is not energy-conserving in the same sense as a time-independent (and therefore continuously time-translation symmetric) Hermitian Hamiltonian of a closed quantum system is, it can nonetheless be shown that energy variations during time-evolution under a time-independent non-Hermitian Hamiltonian are bounded by a fixed limit. This speed limit is determined by the magnitude (*i.e.* norm) of the anti-Hermitian part of the Hamiltonian, relative to the Hermitian part.

Concretely, consider an arbitrary non-Hermitian Hamiltonian $\mathcal{H} = \mathcal{H}_H - i\mathcal{H}_A$, where \mathcal{H}_H and $-i\mathcal{H}_A$ are its Hermitian and anti-Hermitian parts respectively. Without loss of generality, the Hamiltonian can be rescaled such that $\|\mathcal{H}_H\|_2 = 1$, where here $\|\cdot\|_2$ denotes the spectral norm. Starting from an initial normalized quantum state ω_0 , the state after evolution by time t is

$$\omega_t = e^{-i\mathcal{H}t} \omega_0 e^{+i\mathcal{H}^\dagger t}. \quad (\text{S1.1})$$

We evaluate the speed of change of energy of the state,

$$\begin{aligned} \left| \frac{d}{dt} E_t \right| &= \left| \frac{d}{dt} \langle \mathcal{H} \rangle_{\omega_t} \right| = \left| \frac{d}{dt} \text{tr}(\mathcal{H} \omega_t) \right| = \left| \frac{d}{dt} \text{tr} \left(\mathcal{H} e^{-i\mathcal{H}t} \omega_0 e^{+i\mathcal{H}^\dagger t} \right) \right| \\ &= \left| \text{tr} \left[\mathcal{H} \left(\frac{d}{dt} e^{-i\mathcal{H}t} \right) \omega_0 e^{+i\mathcal{H}^\dagger t} + \mathcal{H} e^{-i\mathcal{H}t} \omega_0 \left(\frac{d}{dt} e^{+i\mathcal{H}^\dagger t} \right) \right] \right| \\ &= \left| \text{tr} \left[\mathcal{H} (-i\mathcal{H}) e^{-i\mathcal{H}t} \omega_0 e^{+i\mathcal{H}^\dagger t} + \mathcal{H} e^{-i\mathcal{H}t} \omega_0 (+i\mathcal{H}^\dagger) e^{+i\mathcal{H}^\dagger t} \right] \right| \\ &= \left| \text{tr} [(\mathcal{H}^\dagger - \mathcal{H}) \mathcal{H} \omega_t] \right| \\ &= 2 |\text{tr}(\mathcal{H}_A \mathcal{H} \omega_t)|, \end{aligned} \quad (\text{S1.2})$$

where we have used the cyclic property of the trace. Then, noting that ω_t is a quantum state and is positive semidefinite, Hölder's inequality for inner product spaces implies

$$\left| \frac{d}{dt} E_t \right| \leq 2 \|\mathcal{H}_A \mathcal{H}\|_2 \text{tr}(\omega_t). \quad (\text{S1.3})$$

Lastly, noting that the spectral norm is sub-multiplicative and using the triangle inequality, we have

$$\begin{aligned} \left| \frac{d}{dt} E_t \right| &\leq 2 \|\mathcal{H}_A\|_2 \|\mathcal{H}\|_2 \text{tr}(\omega_t) \\ &\leq 2 \|\mathcal{H}_A\|_2 (\|\mathcal{H}_H\|_2 + \|\mathcal{H}_A\|_2) \text{tr}(\omega_t) \\ &\leq 2 \|\mathcal{H}_A\|_2 (1 + \|\mathcal{H}_A\|_2) \text{tr}(\omega_t), \end{aligned} \quad (\text{S1.4})$$

which is the speed limit we alluded to. Observe that for Hermitian Hamiltonians, for which $\mathcal{H}_A = 0$, this bound reproduces energy conservation,

$$\left| \frac{d}{dt} E_t \right| \leq 0 \implies \frac{d}{dt} E_t = 0. \quad (\text{S1.5})$$

In the analysis above, the energy of the state E_t is defined with respect to ω_t with no further normalization considerations. However, in the non-Hermitian setting, state normalization is not generically preserved—*i.e.* $\text{tr}(\omega_t) \neq \text{tr}(\omega_0) = 1$. Then there is no physical reason to forbid scalar rescaling of quantum states as in conventional Hermitian systems, that is, one can envision mathematical transformations $\omega_t \mapsto \alpha \omega_t$ for any $\alpha > 0$ to be allowed. Manifestly E_t and $(d/dt)E_t$ as analyzed above are not invariant to such rescalings. To enforce invariance, we may consider E_t and $(d/dt)E_t$ normalized by the quantum state norm $\text{tr}(\omega_t)$. Then we have the compact result

$$\frac{1}{\text{tr}(\omega_t)} \left| \frac{d}{dt} E_t \right| \leq 2 \|\mathcal{H}_A\|_2 (1 + \|\mathcal{H}_A\|_2). \quad (\text{S1.6})$$

Supplementary Note 2: Further details on quantum simulation methods

A. Implementation of uncontrolled and coherently controlled multi-qubit Pauli rotations

An exponentiated Pauli string $e^{-i\theta\sigma}$ for a coefficient $\theta \in \mathbb{R}$ and Pauli string σ acting on n qubits, also referred to as a multi-qubit Pauli rotation, can be implemented on a quantum circuit with the following standard construction [4],

$$e^{-i\theta\sigma} = B^\dagger E^\dagger R_1^z(2\theta)EB, \quad B = \bigotimes_{j=1}^n B_j, \quad E^\dagger = \prod_{\substack{j=2 \\ \sigma_j \neq \mathbb{I}}}^n CX_{j1}, \quad B_j = \begin{cases} \mathbb{I} & \sigma_j \in \{\mathbb{I}, Z\} \\ H & \sigma_j = X \\ HS^\dagger & \sigma_j = Y, \end{cases} \quad (\text{S2.1})$$

where we have written $\sigma = \bigotimes_{j=1}^n \sigma_j$ for single-qubit Pauli operators $\sigma_j \in \{\mathbb{I}, X, Y, Z\}$, and we assume the first and last Paulis are non-trivial, $\sigma_1 \neq \mathbb{I}$ and $\sigma_n \neq \mathbb{I}$, without loss of generality. Here B is a layer of Clifford single-qubit rotations acting as a basis transformation, E is an entangler that connects qubits in the support of the Pauli string, $CX_{jj'}$ is a CX gate with control and target on qubits j and j' respectively, and H and S are the Hadamard and phase gates respectively. The R^z rotation gate in the middle of the construction acts only on a single qubit. See Supplementary Figure S1a for a circuit diagram.

The structure of the entangler E above requires numerous long-range CX gates. In particular, CX gates connecting the n^{th} qubit and the first qubit are needed, amongst others. This is problematic on devices with effectively linear nearest-neighbor (LNN) qubit connectivity, where qubits are connected only to adjacent ones in a one-dimensional chain. While in principle a long-range CX can be decomposed into nearest-neighbor CXs through the insertion of SWAP gates, which exchange the states of neighboring qubits and in turn can be implemented with 3 nearest-neighbor CXs, or a bridge gate construction [5] (see Supplementary Figures S1c and S1e for circuit illustrations), these decompositions are hugely expensive in the circuit depth and gate counts incurred.

An alternative implementation of the entangler E uses a ladder of CX gates that span qubits in the support $\Lambda(\sigma)$ of σ , and reduces both the number of non-nearest-neighbor CX gates and their average range:

$$E^\dagger = \prod_{j=2}^{|\Lambda(\sigma)|} CX_{\Lambda(\sigma)_j \Lambda(\sigma)_{j-1}}, \quad \Lambda(\sigma) = (j = 1, 2, \dots, n : \sigma_j \neq \mathbb{I}), \quad (\text{S2.2})$$

which is illustrated in Supplementary Figure S1b. This implementation requires non-nearest-neighbor CX gates only to connect across qubits not in the support of σ . It is thus advantageous to use this structure on LNN qubit connectivity topologies, as is the case in our experiments.

The controlled versions of the exponentiated Pauli string $e^{-i\theta\sigma}$ are written

$$\begin{aligned} C[e^{-i\theta\sigma}] &= |0\rangle\langle 0| \otimes \mathbb{I} + |1\rangle\langle 1| \otimes e^{-i\theta\sigma}, \\ \bar{C}[e^{-i\theta\sigma}] &= |1\rangle\langle 1| \otimes \mathbb{I} + |0\rangle\langle 0| \otimes e^{-i\theta\sigma} = (X \otimes \mathbb{I})C[e^{-i\theta\sigma}](X \otimes \mathbb{I}), \end{aligned} \quad (\text{S2.3})$$

where we have introduced an additional qubit to act as the control, and C and \bar{C} denote coherent control by the $|0\rangle$ and $|1\rangle$ states of the control qubit respectively. That is, $C[e^{-i\theta\sigma}]$ acts as the identity and as $e^{-i\theta\sigma}$ on the n system qubits when the control qubit is in the $|0\rangle$ and $|1\rangle$ states respectively. The $\bar{C}[e^{-i\theta\sigma}]$ gate is identical to $C[e^{-i\theta\sigma}]$ but with the control states flipped, and can be implemented as $C[e^{-i\theta\sigma}]$ sandwiched by X gates on the control qubit.

A straightforward but naïve circuit construction for $C[e^{-i\theta\sigma}]$ follows by adding controls to every gate in the circuit for $e^{-i\theta\sigma}$ as written in Eqs. (S2.1) and (S2.2) above. This turns the single-qubit Clifford gates in the B layers into controlled Cliffords, the CX gates in E into Toffoli gates (double-controlled X gates), and the single-qubit R^z rotation into a controlled R^z rotation. Using the CX ladder implementation in Eq. (S2.2), we have explicitly

$$C[e^{i\theta\sigma}] = CB^\dagger CE^\dagger CR_1^z(2\theta)CECB, \quad CB = \bigotimes_{j=1}^n CB_j, \quad CE^\dagger = \prod_{j=2}^{|\Lambda(\sigma)|} CCX_{\Lambda(\sigma)_j \Lambda(\sigma)_{j-1}}, \quad (\text{S2.4})$$

where $CCX_{jj'} = C[CX_{jj'}]$ is the Toffoli gate with the control ancillary qubit and qubit j as controls, and qubit j' as the target. But this construction is stupendously expensive, as controlled gates are deep when decomposed into 1- and 2-qubit basis gates satisfying qubit connectivities. For example, a Toffoli gate decomposes into 6 CXs disregarding connectivity [4, 6]; satisfying connectivity further increases this overhead as gates have to be introduced to bridge between non-adjacent qubits.

A much more efficient construction for $C[e^{-i\theta\sigma}]$ arises by noting that the circuits in Eqs. (S2.1) and (S2.2) are symmetric, $E^\dagger E = \mathbb{I}$ and $B^\dagger B = \mathbb{I}$, and so without the R^z in the middle the circuit collapses into the identity. Then

$$C[e^{i\theta\sigma}] = B^\dagger E^\dagger C R_1^z(2\theta) E B \quad (\text{S2.5})$$

and the CR^z gate decomposes compactly into a pair of CX gates and a pair of single-qubit R^z rotations. See Supplementary Figures S1f and S1g for circuit diagrams. This construction for $C[e^{-i\theta\sigma}]$ is only slightly more expensive than the uncontrolled $e^{-i\theta\sigma}$ itself, incurring a pair of CXs to connect to the control qubit and an additional single-qubit R^z rotation. We use this implementation in our experiments.

B. Implementation of \mathcal{M}_A map and time steps

We reproduce the defining requirement of the map \mathcal{M}_A as written in Eq. (12) of [Methods](#) here,

$$\mathcal{M}_A(\rho) = \mathcal{N} [e^{-\mathcal{H}_A \Delta t} \rho e^{-\mathcal{H}_A \Delta t}] + \mathcal{O}\left(\frac{1}{m^2}\right), \quad (\text{S2.6})$$

for a Hermitian Hamiltonian \mathcal{H}_A , any arbitrary state ρ , and simulation time step $\Delta t = t/m$ for a number of time steps m . In the context of our present work, \mathcal{H}_A originates from a parent Hamiltonian $\mathcal{H} = \mathcal{H}_H - i\mathcal{H}_A$ which need not be Hermitian, where \mathcal{H}_H and $-i\mathcal{H}_A$ are the Hermitian and anti-Hermitian components of the Hamiltonian respectively. As written above, the action of \mathcal{M}_A is to implement normalized imaginary time-evolution under \mathcal{H}_A .

a. An effective square root of \mathcal{H}_A is known or efficiently computable

In the case that a Hermitian auxiliary Hamiltonian \mathcal{R} is known or efficiently computable such that $\mathcal{R}^2 = \mathcal{H}_A$, a linear combination of unitaries (LCU) construction implementing an action $W \propto U_+ + U_-$ with U_\pm approximating forward and backward time-evolution by \mathcal{R} can be used to realize the \mathcal{M}_A map, as described in [Methods](#). That is, supposing that we have circuit components U_\pm such that

$$U_\pm = e^{\pm i\mathcal{R}\sqrt{2\Delta t}} + \mathcal{O}(\Delta t^2), \quad (\text{S2.7})$$

we can then assemble via LCU

$$\begin{aligned} W = \frac{1}{2}(U_+ + U_-) &= \frac{1}{2} \left(e^{+i\mathcal{R}\sqrt{2\Delta t}} + e^{-i\mathcal{R}\sqrt{2\Delta t}} + \mathcal{O}(\Delta t^2) \right) = 1 - \mathcal{R}^2 \Delta t + \mathcal{O}(\Delta t^2) \\ &= e^{-\mathcal{H}_A \Delta t} + \mathcal{O}(\Delta t^2), \end{aligned} \quad (\text{S2.8})$$

and accordingly

$$\begin{aligned} \mathcal{M}_A(\rho) = \mathcal{N} [W\rho W^\dagger] &= \mathcal{N} \left\{ \left[e^{-\mathcal{H}_A \Delta t} + \mathcal{O}(\Delta t^2) \right] \rho \left[e^{-\mathcal{H}_A \Delta t} + \mathcal{O}(\Delta t^2) \right] \right\} \\ &= \mathcal{N} [e^{-\mathcal{H}_A \Delta t} \rho e^{-\mathcal{H}_A \Delta t}] + \mathcal{O}\left(\frac{1}{m^2}\right), \end{aligned} \quad (\text{S2.9})$$

as desired. As introduced in [Methods](#), the LCU construction implementing W straightforwardly requires a single ancillary qubit prepared in the $|+\rangle$ state, which coherently controls U_+ and U_- on the system register conditioned on its $|0\rangle$ and $|1\rangle$ states interchangeably, followed by a measurement in the σ^x -basis, equivalent to a Hadamard gate followed by a computational basis (σ^z -basis) measurement. The implementation succeeds when a $|0\rangle$ -outcome is reported and fails otherwise. The ancillary qubit can be re-used through mid-circuit qubit reset before the next time step begins. Figure 1d in the main text illustrates the general LCU circuit structure, and Figures 1c and 1e illustrate the structure of time-evolution circuits assembled using this approach.

The square root \mathcal{R} can be obtained from algebraic manipulation of \mathcal{H}_A in certain problems. Constraints on the symmetries and properties of the system can oftentimes also be exploited. There is broad literature on, for example, the roots of topological insulators and superconductors [7–10] and generalized classes of symmetry-protected topological or topologically ordered systems [11–16]. In situations where \mathcal{R} is difficult to obtain, an alternative approach that requires only knowledge of \mathcal{H}_A , albeit incurring higher overhead, can be used, which we detail in Supplementary Note 2 B d.

The coherently controlled forward and backward time-evolution blocks U_+ and U_- in the LCU can be implemented by trotterization, as we mention in [Methods](#). For this, we require the Pauli decomposition of \mathcal{R} , which then lends a standard implementation of U_{\pm} through, for example, the first-order Trotter-Lie product formula,

$$\mathcal{R} = \sum_{k=1}^{K_R} \gamma_k \eta^k, \quad U_{\pm} = \prod_{k=1}^{K_R} e^{\pm i \gamma_k \eta^k \sqrt{2\Delta t}}, \quad CU_{\pm} = \prod_{k=1}^{K_R} C \left[e^{\pm i \gamma_k \eta^k \sqrt{2\Delta t}} \right] \quad (\text{S2.10})$$

where coefficients $\gamma_k \in \mathbb{R}$ and η^k are Pauli strings. That is, the time-evolution circuits for U_{\pm} comprise layers of multi-qubit Pauli rotations (*i.e.* exponentiated Pauli strings), and accordingly CU_{\pm} can be implemented as layers of coherently controlled multi-qubit Pauli rotations. We discussed in Supplementary Note [2A](#) the efficient implementation of controlled multi-qubit Pauli rotations at the gate level on hardware.

A relevant question concerns the conditions under which \mathcal{R} exists. A positive semidefinite Hermitian \mathcal{H}_A always possesses a square root \mathcal{R} that is positive semidefinite and Hermitian. In the case that \mathcal{H}_A is not positive semidefinite, one can trivially introduce an energy offset to make it so, $\mathcal{H}_A \rightarrow \mathcal{H}_A + \lambda \mathbb{I}$, for any $\lambda \geq |\lambda_{\min}|$ where λ_{\min} is the smallest eigenenergy of \mathcal{H}_A . Such an energy offset is inconsequential to the normalized time-evolution, as

$$\mathcal{N} \left[e^{-(\mathcal{H}_A + \lambda \mathbb{I}) \Delta t} \rho e^{-(\mathcal{H}_A + \lambda \mathbb{I}) \Delta t} \right] = \mathcal{N} \left[e^{-2\lambda \Delta t} e^{-\mathcal{H}_A \Delta t} \rho e^{-\mathcal{H}_A \Delta t} \right] = \mathcal{N} \left[e^{-\mathcal{H}_A \Delta t} \rho e^{-\mathcal{H}_A \Delta t} \right], \quad (\text{S2.11})$$

and therefore works as a trick of convenience to realize well-defined choices of \mathcal{R} . Here, on grounds of physicality of the system of interest, we assume that the spectrum of \mathcal{H}_A is bounded from below, such that λ_{\min} is finite. The minimum eigenenergy λ_{\min} can be estimated from the algebraic structure of \mathcal{H}_A or numerically. Alternatively, without additional calculation, a simple conservative, but typically much excessive, choice is $\lambda = \sum_{k=1}^{K_A} |\beta_k|$, where β_k are the coefficients of the Pauli decomposition of \mathcal{H}_A as written in Eq. [\(13\)](#) of [Methods](#).

In the present context of the edge burst, it was not necessary to invoke this energy shift as $\mathcal{H}_A^{\text{eb}}$ is positive semidefinite, as can be seen from Eq. [\(8\)](#) of [Methods](#). In fact, by leveraging the on-site structure of $\mathcal{H}_A^{\text{eb}}$, we were able to obtain a Hermitian auxiliary Hamiltonian $\mathcal{H}_{\text{aux}}^{\text{eb}}$ taking the role of \mathcal{R} , such that the normalized superposition of its forward and backward time-evolutions via LCU implements the $e^{-\mathcal{H}_A^{\text{eb}} \Delta t}$ evolution of \mathcal{M}_A exactly, instead of to $\mathcal{O}(1/m^2)$ error as demanded generally here. We detailed this optimization in [Methods](#). The implementation of the forward and backward time-evolutions via first-order trotterization, however, re-introduces $\mathcal{O}(1/m^2)$ approximation error, so the reduction in error from this optimization is sub-dominant. On general \mathcal{H}_A with complicated, possibly interacting, structure, we expect that such modifications to achieve errorless LCUs would be difficult; but we re-iterate that they are unnecessary for the simulation methodology to work.

b. Circuit depth reduction by merging pairs of time steps

We remark that a general circuit optimization trick can be invoked for every pair of time steps, that roughly halves the circuit depth. We perform a re-ordering of \mathcal{M}_H and \mathcal{M}_A in the second time step,

$$(\mathcal{M}_A \circ \mathcal{M}_H)^2(\rho) = (\mathcal{M}_H \circ \mathcal{M}_A \circ \mathcal{M}_A \circ \mathcal{M}_H)(\rho) + \mathcal{O}\left(\frac{1}{m^2}\right), \quad (\text{S2.12})$$

as the commutator of \mathcal{M}_H and \mathcal{M}_A acting on ρ is of order $\mathcal{O}(\Delta t^2)$, and considering the middle consecutive $\mathcal{M}_A \circ \mathcal{M}_A$, one observes

$$\begin{aligned} W^2 \propto (U_+ + U_-)^2 &= \left(e^{+i\mathcal{R}\sqrt{2\Delta t}} + e^{-i\mathcal{R}\sqrt{2\Delta t}} + \mathcal{O}(\Delta t^2) \right)^2 \\ &= \left(\mathbb{I} + e^{-2i\mathcal{R}\sqrt{2\Delta t}} + \mathcal{O}(\Delta t^2) \right) \left(\mathbb{I} + e^{+2i\mathcal{R}\sqrt{2\Delta t}} + \mathcal{O}(\Delta t^2) \right), \end{aligned} \quad (\text{S2.13})$$

which informs us that the same action across two time steps can be realized to the same $\mathcal{O}(1/m^2)$ error but restructured in the following way,

$$(\mathcal{M}_A \circ \mathcal{M}_H)^2(\rho) = (\mathcal{M}_H \circ \mathcal{M}_{A-} \circ \mathcal{M}_{A+} \circ \mathcal{M}_H)(\rho) + \mathcal{O}\left(\frac{1}{m^2}\right), \quad (\text{S2.14})$$

where

$$\mathcal{M}_{A\pm}(\rho) = \mathcal{N} \left[\left(\mathbb{I} + e^{\mp 2i\mathcal{R}\sqrt{2\Delta t}} \right) \rho \left(\mathbb{I} + e^{\pm 2i\mathcal{R}\sqrt{2\Delta t}} \right) \right] + \mathcal{O}\left(\frac{1}{m^2}\right). \quad (\text{S2.15})$$

That is, the first map \mathcal{M}_{A+} requires an LCU that superposes the unitaries \mathbb{I} and forward time-evolution by $2\mathcal{R}$, and the second map \mathcal{M}_{A-} requires an LCU that superposes the unitaries \mathbb{I} and backward time-evolution by $2\mathcal{R}$. Now, we note that the implementation of the \mathbb{I} unitary portions in the LCU is trivial, as a coherently controlled- \mathbb{I} is simply the identity—*i.e.* no gates at all are required.

Therefore, this optimized implementation of $(\mathcal{M}_A \circ \mathcal{M}_A)^2$ requires only two controlled time-evolution unitaries (forward and backward by $2\mathcal{R}$), compared to the original four (two pairs of forward and backward by \mathcal{R}). We illustrate this circuit transformation in Supplementary Figures S1i and S1j. As the time-evolution unitaries are expensive and account for an overwhelming majority of the depth of the overall quantum simulation circuits, this optimization is hugely beneficial. We employed this technique in all of our experiments,

c. Higher-order implementations of \mathcal{M}_A via many-term LCUs

In the main text, [Methods](#), and Supplementary Note 2Ba, we considered mainly an \mathcal{M}_A that approximates normalized time-evolution by $-i\mathcal{H}_A$ to $\mathcal{O}(1/m^2)$ error, as that is sufficient for our quantum simulation methodology for non-Hermitian Hamiltonian as a whole to work. This defining requirement on \mathcal{M}_A was written in Eq. (12) of [Methods](#) and repeated in Eq. (S2.6). But it can also be of interest to examine more advanced realizations of \mathcal{M}_A that approximates the time-evolution to higher-order error,

$$\mathcal{M}_A(\rho) = \mathcal{N} [e^{-\mathcal{H}_A \Delta t} \rho e^{-\mathcal{H}_A \Delta t}] + \mathcal{O}\left(\frac{1}{m^\kappa}\right), \quad (\text{S2.16})$$

for orders $\kappa \geq 2$. As described in [Methods](#), in particular Eq. (15) and the surrounding discussion, the general strategy to obtain such realizations is to consider LCU expansions of the form

$$A_0 \mathbb{I} + \sum_{b=1}^B A_b (e^{+i\mathcal{R} \Delta \tau_b} + e^{-i\mathcal{R} \Delta \tau_b}) = e^{-\mathcal{H}_A \Delta t} + \mathcal{O}\left(\frac{1}{m^\kappa}\right), \quad (\text{S2.17})$$

for coefficients $A_0, \dots, A_B \geq 0$ and rescaled simulation times $\{\Delta \tau_b\}_b$, and to match their Taylor expansions order-by-order on both sides. This leads to a system of polynomial equations that can then be solved. Generally, for any $\kappa \geq 2$, candidate LCU expansions realizing \mathcal{M}_A can be found this way, and it is generally beneficial to select a solution with a minimal number of term pairs B as this directly reduces circuit depth and the number of ancillary qubits needed to implement the LCU. We provide some examples of higher-order expansions with a minimal number of terms in Supplementary Table S6.

κ	Expansion	# Anc. Qubits
2	$e^{\pm iR\sqrt{2}\Delta t}$	1
3	$4\mathbb{I} + e^{\pm iR\sqrt{6}\Delta t}$	2
4	$(3 - \sqrt{6})e^{\pm iR\sqrt{2(3+\sqrt{6})}\Delta t} + (3 + \sqrt{6})e^{\pm iR\sqrt{2(3-\sqrt{6})}\Delta t}$	2
5	$32\mathbb{I} + (7 - 2\sqrt{10})e^{\pm iR\sqrt{2(5+\sqrt{10})}\Delta t} + (7 + 2\sqrt{10})e^{\pm iR\sqrt{2(5-\sqrt{10})}\Delta t}$	3

Supplementary Table S6. Examples of linear combination of unitaries (LCU) expansions that approximate the non-unitary (imaginary) time-evolution propagator $e^{-\mathcal{H}_A \Delta t}$ for a Hermitian Hamiltonian \mathcal{H}_A to $\mathcal{O}(1/m^\kappa)$ error, and thus can be used to implement the \mathcal{M}_A map used in our time-evolution algorithm for general non-Hermitian Hamiltonians. The $\kappa = 2$ case corresponds to the setting discussed in the main text, [Methods](#), and Supplementary Note 2Ba. Higher κ beyond those presented here can be achieved by using more terms in the LCU expansions. Here \mathcal{R} is any Hermitian Hamiltonian such that $\mathcal{R}^2 = \mathcal{H}_A$, we use the shorthand $e^{\pm iA} = e^{+iA} + e^{-iA}$, and we present the expansions up to overall normalization factors that are omitted.

d. An effective square root of \mathcal{H}_A is not known

In the case that a square root of \mathcal{H}_A is not known or cannot be efficiently found, there is an alternative, more general approach of realizing \mathcal{M}_A , albeit requiring an extra ancillary qubit register in addition to the LCU ancillary qubit(s). Just like the LCU ancillary qubits, this ancillary qubit register can be re-used through mid-circuit qubit reset before the next time step.

Recall that by premise \mathcal{H} is local and thus so is \mathcal{H}_A ; we assume they are l -local, that is, they comprise terms that act on at most $l \in \mathcal{O}(1)$ sites each on the system, independent of the system size. Then we can write

$$\mathcal{H}_A = \sum_{k=1}^{L_A} \kappa_k h_k, \quad (\text{S2.18})$$

for real coefficients $\kappa_k > 0$ and Hermitian h_k that each have support on at most l sites, and a number of terms L_A that is polynomial in the system size. For simplicity, we assume h_k are positive semidefinite; this can always be made the case by adding suitable energy offsets to \mathcal{H}_A , whose spectrum we assume to be lower-bounded on grounds of physicality, or alternatively to each h_k , in a similar fashion as discussed in Supplementary Note 2B a. Then there exist positive semidefinite Hermitian r_k for each h_k such that $r_k^2 = h_k$. Either these are algebraically known from the form of h_k , or they can be efficiently computed, since each h_k acts only on l sites and can each be efficiently processed.

Now we consider the larger Hermitian Hamiltonian

$$\mathcal{L} = \sum_{k=1}^{L_A} \sqrt{\kappa_k} r_k \otimes (|k\rangle_a \langle 0|_a + |0\rangle_a \langle k|_a), \quad (\text{S2.19})$$

where we have introduced an ancillary Hilbert space that is at least $(L_A + 1)$ -dimensional, that is, comprising at least $\lceil \log_2(L_A + 1) \rceil$ qubits, labeled by the subscript ‘a’ above. As defined, \mathcal{L} is Hermitian, and one observes

$$\mathcal{L}^{2p} (|\psi\rangle \otimes |0\rangle_a) = [(\mathcal{H}_A)^p |\psi\rangle] \otimes |0\rangle_a, \quad (\text{S2.20})$$

for any power $p \in \mathbb{N}$ and any system state $|\psi\rangle$. That is, given that the ancillary register starts in state $|0\rangle_a$, the action of \mathcal{L}^{2p} is identical to that of $(\mathcal{H}_A)^p$ on the system qubits. Note that the ancillary register is brought back to $|0\rangle_a$ after being acted upon by \mathcal{L}^{2p} , and indeed is entirely disentangled with the system qubits.

In the same spirit as in Supplementary Note 2B a, we consider an LCU construction implementing $\overline{W} \propto (\overline{U}_+ + \overline{U}_-)$ with \overline{U}_\pm approximating forward and backward time-evolution by \mathcal{L} to $\mathcal{O}(1/m^2)$ error. The difference is that \overline{U}_\pm here act jointly on the system and ancillary qubit register, whereas U_\pm before acted only on the system register with no involvement of any ancillae. Explicitly, supposing that we have circuit components \overline{U}_\pm such that

$$\overline{U}_\pm = e^{\pm i\mathcal{L}\sqrt{2\Delta t}} + \mathcal{O}(\Delta t^2), \quad (\text{S2.21})$$

we find

$$\begin{aligned} \overline{W} (|\psi\rangle \otimes |0\rangle_a) &= \frac{1}{2} (\overline{U}_+ + \overline{U}_-) (|\psi\rangle \otimes |0\rangle_a) = \frac{1}{2} \left(e^{+i\mathcal{L}\sqrt{2\Delta t}} + e^{-i\mathcal{L}\sqrt{2\Delta t}} + \mathcal{O}(\Delta t^2) \right) (|\psi\rangle \otimes |0\rangle_a) \\ &= [\mathbb{I} - \mathcal{L}^2 \Delta t + \mathcal{O}(\Delta t^2)] (|\psi\rangle \otimes |0\rangle_a) \\ &= [(\mathbb{I} - \mathcal{H}_A \Delta t) |\psi\rangle] \otimes |0\rangle_a + \mathcal{O}(\Delta t^2) \\ &= e^{-\mathcal{H}_A \Delta t} |\psi\rangle \otimes |0\rangle_a + \mathcal{O}(\Delta t^2). \end{aligned} \quad (\text{S2.22})$$

Examining the system qubits, we find accordingly that

$$\begin{aligned} \mathcal{M}_A(\rho) &\equiv \mathcal{N} \left\{ \text{tr}_a \left[\overline{W} (\rho \otimes |0\rangle_a \langle 0|_a) \overline{W}^\dagger \right] \right\} = \mathcal{N} \left[e^{-\mathcal{H}_A \Delta t} \rho e^{-\mathcal{H}_A \Delta t} \otimes |0\rangle_a \langle 0|_a \right] + \mathcal{O}\left(\frac{1}{m^2}\right) \\ &= \mathcal{N} \left[e^{-\mathcal{H}_A \Delta t} \rho e^{-\mathcal{H}_A \Delta t} \right] + \mathcal{O}\left(\frac{1}{m^2}\right), \end{aligned} \quad (\text{S2.23})$$

as desired. That is, an LCU construction implementing $\overline{W} \propto (\overline{U}_+ + \overline{U}_-)$ achieves \mathcal{M}_A .

A remaining detail is how the coherently controlled \overline{U}_\pm necessary in the LCU can be implemented. Without loss of generality we can perform processing (*i.e.* perform Pauli-basis decomposition) such that the $\{r_k\}_k$ terms in Eq. (S2.19) are Pauli strings. Likewise, we consider expressing the ancillary portion of each of the terms in \mathcal{L} as Pauli strings. The details of this ancillary Pauli decomposition depends on the mapping chosen between the $(L_A + 1)$ -dimensional Hilbert space considered here and a register of qubits—we discuss this below. The number of terms L_A in the Hamiltonian \mathcal{L} remains polynomial in the system size after this rewriting. Ultimately, once \mathcal{L} has been expressed entirely as Pauli strings, conventional trotterization, such as the first-order Trotter-Lie product formula, can be used to implement forward and backward time-evolution (\overline{U}_\pm) by \mathcal{L} to error $\mathcal{O}(1/m^2)$ or better, in the same fashion as for \mathcal{H}_A originally discussed in the main text, [Methods](#), and Supplementary Note 2B a. Coherently controlling \overline{U}_\pm entails adding controls to the Pauli rotations in the trotterization, and we have discussed an efficient implementation of these operations in Supplementary Note 2A.

Lastly, we revisit the issue of mapping the ancillary space onto qubits. We discuss two natural choices:

- Using the minimum possible $\lceil \log_2(L_A + 1) \rceil$ number of ancillary qubits. Then the states $\{|k\rangle_a\}_k$ can be mapped to the basis states of the ancillary qubits in, for example, binary ascending order,

$$|0\rangle_a \equiv |0\dots 00\rangle, \quad |1\rangle_a \equiv |0\dots 01\rangle, \quad |2\rangle_a \equiv |0\dots 10\rangle, \quad |3\rangle_a \equiv |0\dots 11\rangle, \quad \dots \quad (\text{S2.24})$$

While this is space-efficient (in terms of qubit count), an issue is that $|k\rangle_a \langle 0|_a + |0\rangle_a \langle k|_a$ can be relatively complicated when expressed in the Pauli basis of the qubits, containing a number of Pauli strings polynomial in L_A with weight up to $\lceil \log_2(L_A + 1) \rceil$. Therefore the circuit depth may not be particularly shallow.

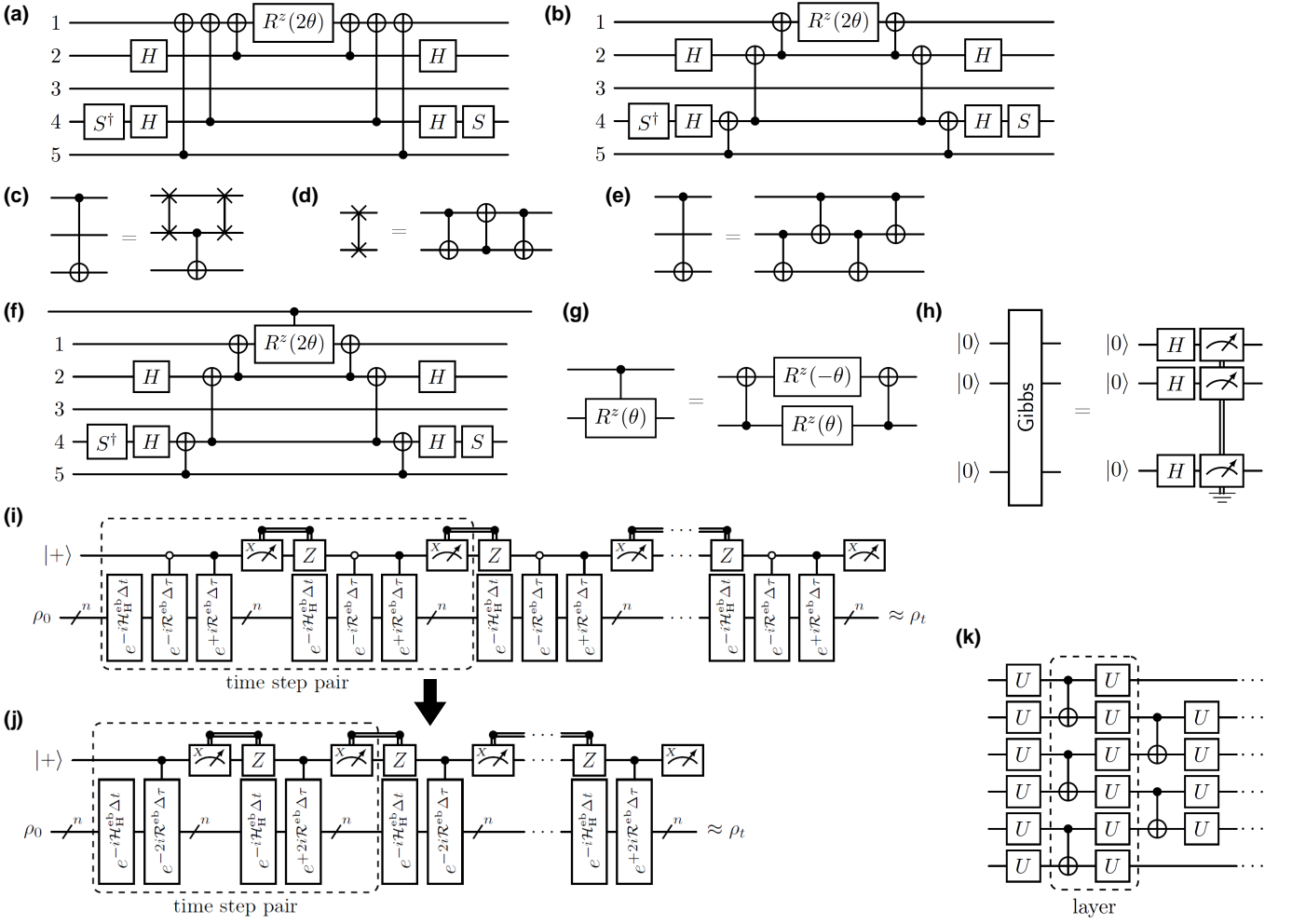
- Choosing to use L_A qubits instead, we enjoy a reduction in circuit depth and complexity, at the expense of using a larger number of ancillary qubits. Here we map the states $\{|k\rangle_a\}_k$ to the basis states of the ancillary qubits via one-hot encoding, for example,

$$|0\rangle_a \equiv |000\dots 0\rangle, \quad |1\rangle_a \equiv |100\dots 0\rangle, \quad |2\rangle_a \equiv |010\dots 0\rangle, \quad |3\rangle_a \equiv |001\dots 0\rangle, \quad \dots \quad (\text{S2.25})$$

That is, $\{|k\rangle_a\}_k$ for $k > 0$ is identified with the ancillary qubit state where the k^{th} qubit is in $|1\rangle$ while all other qubits are in $|0\rangle$. Then straightforwardly,

$$|k\rangle_a \langle 0|_a + |0\rangle_a \langle k|_a \equiv \sigma_k^x, \quad (\text{S2.26})$$

within the subspace of qubit states associated with $\{|k\rangle_a\}_k$, where σ_k^x denotes the single-qubit σ^x Pauli operator acting on the k^{th} ancillary qubit. Thus each $|k\rangle_a \langle 0|_a + |0\rangle_a \langle k|_a$ term maps to only a single-qubit Pauli operator. This is particularly simple to implement.



Supplementary Figure S1. **Detailed quantum simulation circuit structures and components.** (a) Naïve implementation of an exponentiated Pauli string $e^{-i\theta\sigma}$, also referred to as a multi-qubit Pauli rotation, comprising single-qubit Clifford basis changes and an entangler built from CX gates sandwiching a single R^z rotation, as described in Supplementary Note 2 A. The Pauli string illustrated here is $\sigma = \sigma_1^z \sigma_2^x \mathbb{I}_3 \sigma_4^y \sigma_5^z$. (b) Alternative implementation of the same multi-qubit Pauli rotation as in (a) but with the entangler constructed via CX ladders, which reduces the number of long-range CXs and is more suitable for hardware. (c) A non-nearest neighbor CX gate can be reduced to a nearest-neighbor one through insertion of SWAP gates. Longer-range CXs can be decomposed in the same manner recursively. (d) A SWAP gate decomposes into 3 CX gates. (e) Bridge gate construction for non-nearest neighbor CX gates, which is more efficient in CX gate count than the SWAP insertion approach. Likewise, longer-range CXs can be decomposed recursively. (f) A coherently controlled $e^{-i\theta\sigma}$ amounts to inserting a control on the central single-qubit R^z rotation. (g) A controlled- R^z gate decomposes into CX gates and 2 single-qubit R^z rotations. (h) The ∞ -temperature Gibbs state (*i.e.* maximally mixed state) can be prepared by mid-circuit measuring qubits prepared in the $|+\rangle$ product state and discarding the measurement outcomes. (i) Our architecture of time-evolution circuits for non-Hermitian Hamiltonians as described in the main text, [Methods](#) and in Supplementary Note 2 B, comprising time steps of \mathcal{M}_H and \mathcal{M}_A maps approximating evolution by the Hermitian and anti-Hermitian parts of the Hamiltonian respectively. \mathcal{M}_A is achieved through a linear combination of unitaries (LCU) construction, superposing forward and backward time-evolution. A pair of adjacent time steps is highlighted. (j) Merging of a pair of time steps as described in Supplementary Note 2 B b, which halves the circuit depth of \mathcal{M}_A by removing a LCU term from each of the time steps. (k) Ansatz for circuit recompilation, comprising an interleaved brickwork pattern of CX gates and $U(2)$ single-qubit rotations. The angles of the single-qubit rotations are treated as variational parameters.

Supplementary Note 3: Further details on error suppression and mitigation methods

A. Zero-noise extrapolation with physicality constraints

As described in [Methods](#), we employed zero-noise extrapolation (ZNE) as an error mitigation technique [17–21] to reduce the effects of hardware noise (*e.g.* gate errors and decoherence) on our experiment results. To review, we performed repetitions of each experiment circuit at noise amplification factors $1 = \lambda_1 < \lambda_2 < \dots < \lambda_r$, where $\lambda = 1$ corresponds to the unmodified experiment. We assumed an affine relation between $\langle O_k^{(\lambda)} \rangle$ and λ ,

$$\langle O_k^{(\lambda)} \rangle \approx m_k \lambda + c_k, \quad (\text{S3.1})$$

where $\{O_k\}_k$ are the measured observables on the circuit, and $\{m_k\}_k$ and $\{c_k\}_k$ are gradients and zero-noise intercepts respectively. Thus, with $\langle O_k^{(\lambda)} \rangle$ data measured on hardware at $\lambda_1, \dots, \lambda_r$, we perform the least-squares regression

$$(\mathbf{m}^*, \mathbf{c}^*) = \underset{\mathbf{m}, \mathbf{c}}{\operatorname{argmin}} \sum_k \sum_{\gamma=1}^r \left(m_k \lambda_\gamma + c_k - \langle O_k^{(\lambda_\gamma)} \rangle \right)^2, \quad (\text{S3.2})$$

to find best-fit gradients \mathbf{m}^* and intercepts \mathbf{c}^* , as also expressed in Eq. (27) of [Methods](#). On top of this standard ZNE procedure, we imposed physicality constraints on the regression to ensure that our mitigated expectation values (and the regression itself) are physically meaningful. We elaborate on these constraints below.

- *Experiments in p -particle Fock sector measuring site-resolved occupancies, that is, $\{O_k\}_k = \{n_{x\ell}\}_{x\ell}$.* This includes, for example, the experiments shown in Figures 2, 3, 5, 6 of the main text, and Supplementary Figures S2 to S6. For these, we invoked number conservation, which dictates that the number of particles in the system when measured must be p —otherwise an unphysical violation of the number-conserving symmetry of the system has taken place—and hardcore bosonic statistics of the particles in our system, which forbid double occupancy and thus constrains $0 \leq \langle n_{x\ell} \rangle \leq 1$ for all sites. Explicitly, we require

$$\sum_k \langle O_k^{(\lambda)} \rangle = p \quad \wedge \quad 0 \leq \langle O_k^{(\lambda)} \rangle \leq 1, \quad (\text{S3.3})$$

at all noise factors $0 \leq \lambda \leq \lambda_r$, even at intermediary levels not directly measured on hardware but implied by the regression. On the affine relation of Eq. (S3.1), this translates into regression constraints

$$\sum_k m_k = 0 \quad \wedge \quad \sum_k c_k = 1 \quad \wedge \quad \mathbf{0} \leq \mathbf{c} \leq \mathbf{1} \quad \wedge \quad \mathbf{0} \leq \mathbf{m} \lambda_r + \mathbf{c} \leq \mathbf{1}. \quad (\text{S3.4})$$

- *Experiments measuring the imaginary energy in the p -particle sector, that is $\{O_k\}_k = \{\mathcal{H}_A^{\text{eb}}\}$.* This includes, for example, the experiments shown in Figure 4 of the main text. For these we invoked the purely lossy character of \mathcal{H}^{eb} , that is, that $\mathcal{H}_A^{\text{eb}}$ is positive semi-definite, which dictates that $\langle \mathcal{H}_A^{\text{eb}} \rangle \leq 0$. Furthermore, as there are p conserved particles in the quantum system and the smallest eigenenergy of $\mathcal{H}_A^{\text{eb}}$ is $-\gamma$, by the variational principle the imaginary energy of any quantum state must satisfy $-p\gamma \leq \langle \mathcal{H}_A^{\text{eb}} \rangle$. These physicality bounds should hold at all noise factors $0 \leq \lambda \leq \lambda_r$, just as in the case above. On the affine relation of Eq. (S3.1), this translates into regression constraints

$$-p\gamma \leq c \leq 0 \quad \wedge \quad -p\gamma \leq m\lambda_r + c \leq 0, \quad (\text{S3.5})$$

where we have dropped the vector notations for \mathbf{m}, \mathbf{c} as there is only a single measured observable in this context.

We remark that the affine relation in Eq. (S3.1) is not a unique choice and is effectively a linear approximation—the exact variation of $\langle O_k^{(\lambda)} \rangle$ with noise amplification factor λ is in reality an unknown function of the observables, circuit structure, and hardware error characteristics. Prior studies have examined [17–21] other ansatzes, the most common choices other than affine being a quadratic or exponential variation of $\langle O_k^{(\lambda)} \rangle$ with λ . As our circuits are non-Clifford and the hardware noise experienced in experiments is not generally simply a depolarizing channel, there is no strong theoretical justification for any of these other ansatzes, and we did not employ them for simplicity in our work. An additional theoretical challenge is also that these other ansatzes do not, strictly speaking, allow certain physical constraints to hold, unlike the affine relation. For example, as these other regression ansatzes are non-linear, they generally do not support number conservation, as in $\sum_k \langle O_k^{(\lambda)} \rangle = p$ in Eq. (S3.3), across all noise amplification factors $0 \leq \lambda \leq \lambda_r$. Therefore the physical soundness of the regression result using these other ansatzes, in our context, would be unclear.

a. Amplifying noise through local gate folding

To artificially amplify noise to factors $\lambda > 1$, we employed randomized local gate folding (see *e.g.* Ref. [20]), which probabilistically replaces each gate G in the circuit by $GG^\dagger G$, as described in [Methods](#). Amplifying the number of gates in the circuit directly amplifies accumulated noise from gate errors, but also increases circuit depth and thereby amplifies, for example, thermal relaxation and dephasing noise (*i.e.* background decoherence). We comment that we perform folding such that the total number of 1- and 2-qubit gates in the circuit is each increased by factor λ . Merely targeting an increase in the total number of gates in the circuit, irrespective of their type, by λ is insufficient. This is because the error rates of 1- and 2-qubit gates typically differ massively on hardware—indeed, by at least an order of magnitude on the devices used in our experiments—so amplifying the total number of gates by λ without maintaining balance between the number of 1- and 2-qubit gates does not ensure that circuit noise is amplified by λ .

b. Randomizing coherent errors through Pauli twirling

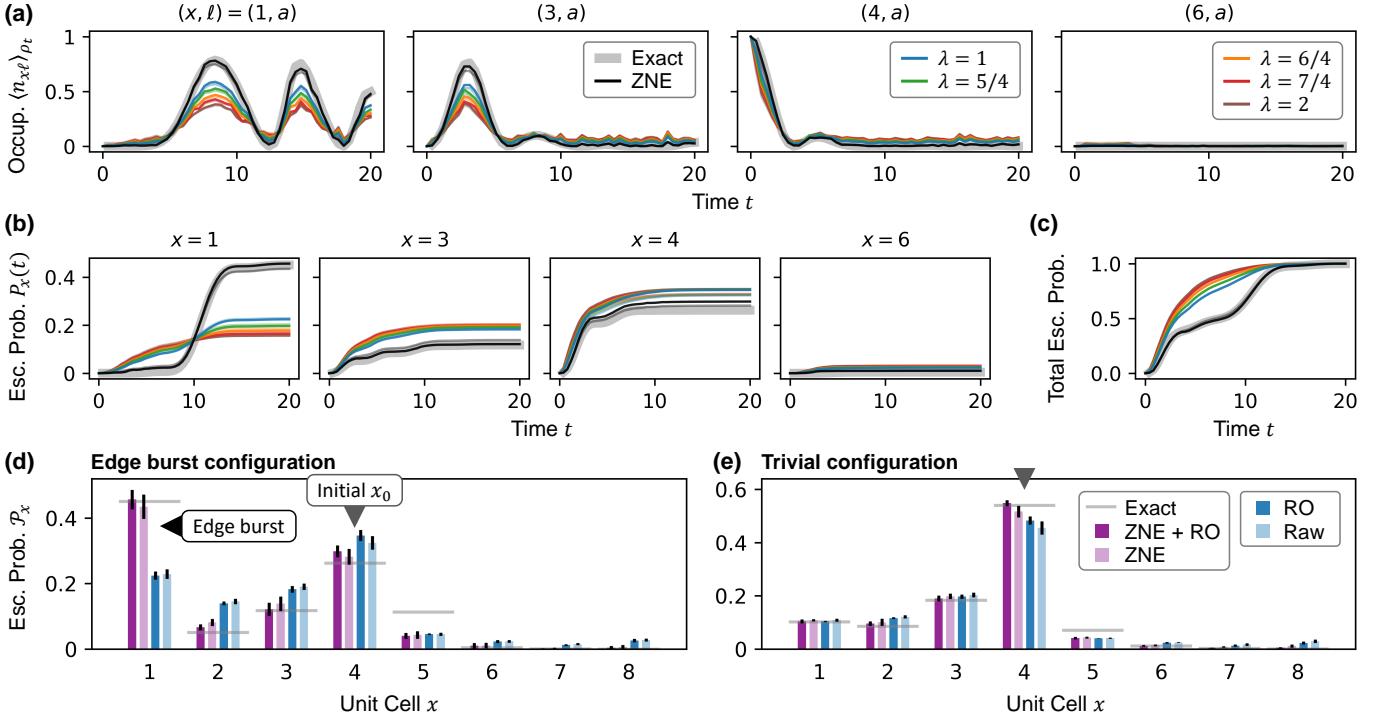
Lastly, we comment on the usage of randomized Pauli twirling [18, 22, 23] in producing circuits for ZNE. As described in [Methods](#), for each experiment circuit at each λ , we produced a set of randomized gate-folded circuits and applied randomized Pauli twirling on those circuits. These circuits were executed on hardware and their results averaged, to produce the $\langle O_k^{(\lambda)} \rangle$ data for regression. The advantage of applying randomized Pauli twirling is that 2-qubit error processes on the circuits, which are the dominant source of noise, are diagonalized into incoherent stochastic (Pauli) noise channels [18, 22, 23], which can be straightforwardly averaged over (across circuit shots and realizations) in experiments. This results in more consistent trends of $\langle O_k^{(\lambda)} \rangle$ against λ , which ZNE relies upon. Without this conversion of noise processes, consistency of $\langle O_k^{(\lambda)} \rangle$ trends is less certain. For example, the coherent composition of coherent error channels (*e.g.* unitary errors arising from gate angle mis-calibration) means that the measured $\langle O_k^{(\lambda)} \rangle$ on a circuit instance can be sensitive to the exact gates selected to be folded.

Supplementary Note 4: Additional Results

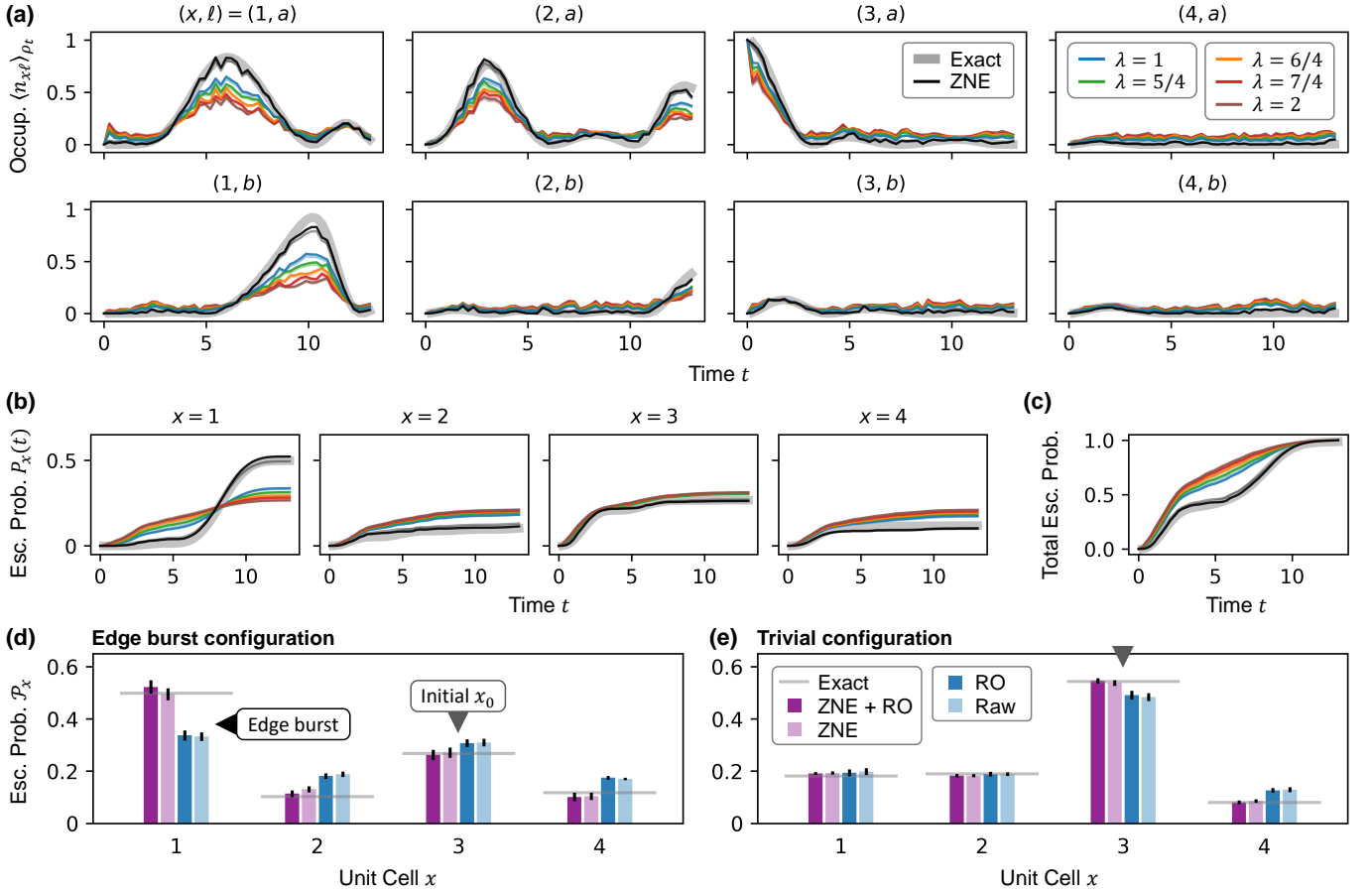
A. Additional experiment results on the canonical edge burst

In Figure 2 and surrounding discussion of the main text, we described hardware results on an $N = 8$ -unit cell quantum ladder in the edge burst and trivial regimes. In Supplementary Figure S2 below, we present an analogous breakdown of results on the same quantum ladder (*i.e.* the same Hamiltonian \mathcal{H}^{eb}) but with different initial particle localizations, here at $x_0 = 4$ instead of $x_0 = 6$ in the main text. Identical to the experiments of Figure 2, we employed trotterization for our quantum simulation circuits without further compression (*e.g.* recompilation) before execution on hardware. The observations and conclusions are qualitatively identical to those in the main text. The real-space signature of the edge burst, a spike in final escape probability \mathcal{P}_x at the $x = 1$ boundary, is clearly observed in the edge burst regime; in contrast in the trivial regime no boundary increase in \mathcal{P}_x appears. Likewise, we observe our error mitigation strategies of zero-noise extrapolation (ZNE) and readout error mitigation (RO) to be of considerable benefit to data quality.

We additionally show a breakdown of experiment results on a smaller $N = 4$ quantum ladder in Supplementary Figure S3, employing likewise trotterization in the quantum simulation methodology. Here, we display a complete dataset of the measured site-resolved occupancy densities $\langle n_{x\ell} \rangle_{\rho_t}$ for all unit cells $x \in [4]$ on the ladder and sublattices $\ell \in \{a, b\}$. The observations are qualitatively similar to those before, namely a spike in \mathcal{P}_x at the $x = 1$ boundary in the edge burst regime and an absence of this signature in the trivial regime.



Supplementary Figure S2. **Canonical edge burst on $N = 8$ quantum ladder with different initial particle localization.** (a) Site-resolved occupancy densities after normalized time-evolution on a 8-unit cell quantum ladder, comparing data measured on quantum hardware at various noise amplification factors λ , after post-processing with zero-noise extrapolation (ZNE), and exact numerics. Solid thin lines are with readout error mitigation (RO) applied; translucent thin lines behind are without. To avoid clutter, only the a sublattice of unit cells $x \in \{1, 3, 4, 6\}$ are shown. (b) Unit-cell-resolved escape probabilities $P_x(t)$ obtained from the data in (a). Time-integration of the occupancy densities first recovers proper wavefunction norm, and a second time-integration produces $P_x(t)$. (c) Total escape probability $P(t)$ summed over all unit cells, which approaches unity as time progresses. (d) Final unit-cell-resolved escape probabilities \mathcal{P}_x in the long-time limit. Data obtained on quantum hardware with and without ZNE and RO, and from exact numerics, are shown. In a parameter regime supporting the edge burst, anomalously high escape probability on the $x = 1$ edge of the ladder is detected; whereas in the trivial regime escape probability is concentrated only near the initial location of the particle (at $x_0 = 4$). Error bars are standard deviations across 8 experiment runs. See Supplementary Tables S1 and S2 for Hamiltonian parameter values and superconducting quantum devices used. The experiments shown here complement Figure 2 of the main text, which reports results on the same quantum ladder but with different initial particle locations (there $x_0 = 6$).

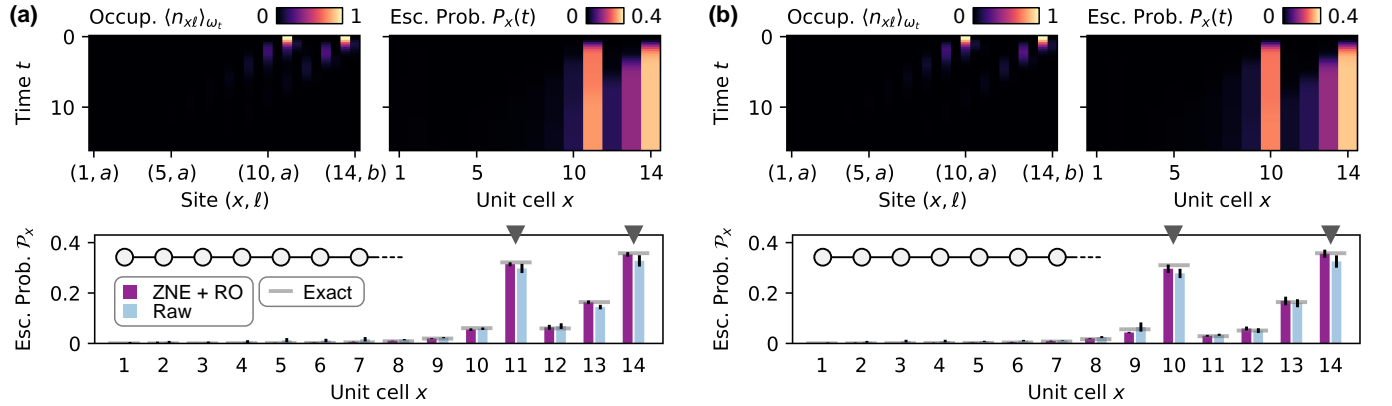


Supplementary Figure S3. **Canonical edge burst on a smaller $N = 4$ quantum ladder.** (a) Site-resolved occupancy densities after normalized time-evolution on a 4-unit cell quantum ladder, comparing data measured on quantum hardware at various noise amplification factors λ , after post-processing with zero-noise extrapolation (ZNE), and exact numerics. Solid thin lines are with readout error mitigation (RO) applied; translucent thin lines behind are without. (b) Unit-cell-resolved escape probabilities $P_x(t)$ obtained from the data in (a). Time-integration of the occupancy densities first recovers proper wavefunction norm, and a second time-integration produces $P_x(t)$. (c) Total escape probability $P(t)$ summed over all unit cells, which approaches unity as time progresses. (d) Final unit-cell-resolved escape probabilities \mathcal{P}_x in the long-time limit. Data obtained on quantum hardware with and without ZNE and RO, and from exact numerics, are shown. In a parameter regime supporting the edge burst, anomalously high escape probability on the $x = 1$ edge of the ladder is detected; whereas in the trivial regime escape probability is concentrated only near the initial location of the particle (at $x_0 = 3$). Error bars are standard deviations across 8 experiment runs. See Supplementary Tables S1 and S2 for Hamiltonian parameter values and superconducting quantum devices used. The experiments shown here complement Figure 2 of the main text and Supplementary Figure S2, which report results on a larger $N = 8$ quantum ladder.

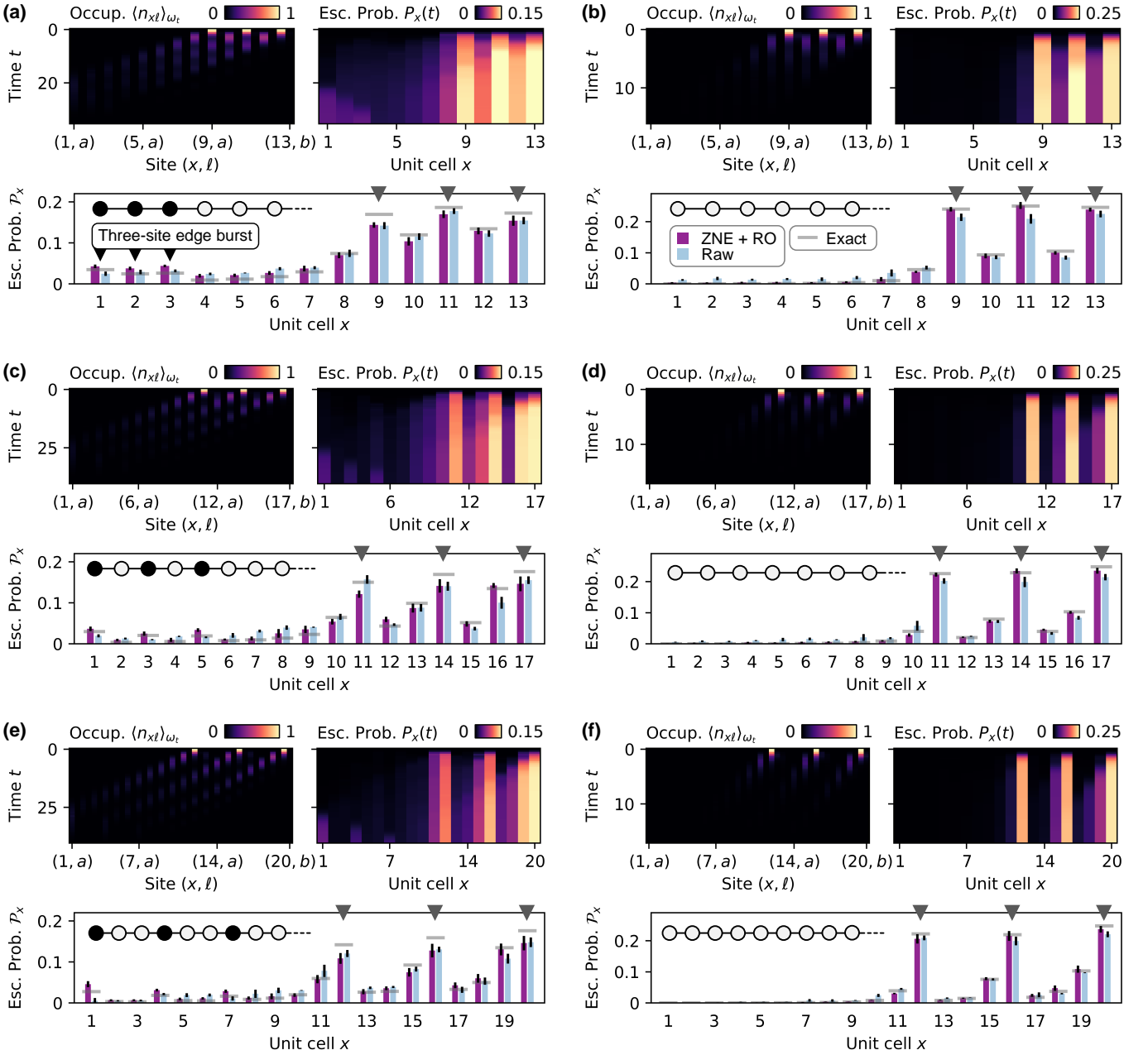
B. Spatially extended edge bursts with multiple interacting particles

In Figure 5 and surrounding discussion of the main text, we described the possibility of obtaining spatially extended edge bursts spanning multiple unit cells, in contrast to the canonical single-particle edge burst that occurs on a single unit cell, and which exhibit spatial ordering, when multiple interacting particles are present on the quantum ladder. There, we began by examining experiments with two interacting particles. Figures 5a, 5c and 5d reported hardware results in the edge burst without ordering and with \mathbb{Z}_2 and \mathbb{Z}_3 ordering respectively, where the occurrence of the edge burst is clearly observed, while Figure 5b reported results without ordering in the trivial regime. As validation that this is indeed an edge burst phenomenon, the spatially ordered edge bursts should vanish in the trivial regime. We verify this in Supplementary Figure S4, which presents hardware results directly analogous to Figures 5c and 5d of the main text but in the trivial regime.

Additionally, as also discussed in the main text, the same phenomenon of spatially extended and ordered edge bursts can be observed with larger numbers of interacting particles. With p particles, it is generically possible to obtain edge bursts extended over p unit cells from the boundary. Here, we report hardware results with three interacting particles in Supplementary Figure S5. A spatially extended edge burst is seen in Supplementary Figure S5a, and edge bursts with \mathbb{Z}_2 and \mathbb{Z}_3 ordering are observed in Supplementary Figure S5c and Supplementary Figure S5e respectively. Supplementary Figures S5b, S5d and S5f show results in the trivial regime, in which no edge burst arises.



Supplementary Figure S4. **Additional results with two interacting particles.** (a) Site-resolved occupancy densities and unit-cell-resolved escape probabilities $P_x(t)$ measured on a 14-unit cell quantum ladder in the trivial regime hosting two interacting particles. The quantum ladder has density-density interactions $U_r > 0$ switched on for $r \leq 3$. Final escape probabilities P_x obtained on hardware with and without zero-noise extrapolation (ZNE) and readout error mitigation (RO), and exact numerics, are shown. Gray arrows denote the initial localization of the particles. (b) Same as (a) but with longer-ranged interactions, $U_r > 0$ switched on for $r \leq 5$, and with correspondingly larger separation in initial localization of the particles. Error bars are standard deviations across 10 experiment runs. See Supplementary Tables S1 and S2 for Hamiltonian parameter values and superconducting quantum devices used. No edge burst is observed in both (a) and (b). Panels (a) and (b) complement Figures 5c and 5d in the main text respectively, which show results in the edge burst regime.



Supplementary Figure S5. **Spatially extended and ordered edge bursts with three interacting particles.** (a) Site-resolved occupancy densities and unit-cell-resolved escape probabilities $P_x(t)$ measured on a 13-unit cell quantum ladder in the edge burst regime hosting three interacting particles. The quantum ladder has density-density interactions $U_r > 0$ switched on for $r = 1$. Final escape probabilities \mathcal{P}_x obtained on hardware with and without zero-noise extrapolation (ZNE) and readout error mitigation (RO), and exact numerics, are shown. Gray arrows denote the initial localization of the particles. (b) Same as (a) but in the trivial regime. (c), (e) Occupancy densities, escape probabilities $P_x(t)$, and final escape probability \mathcal{P}_x on (c) a 17-unit cell ladder with interactions $U_r > 0$ switched on for $r \leq 3$, and a 20-unit cell ladder with interactions $U_r > 0$ for $r \leq 5$, in the edge burst regime. (d), (f) Same as (c) and (e) respectively but in the trivial regime. Spatially extended edge bursts are observed in (a), (c), (e), with \mathbb{Z}_2 and \mathbb{Z}_3 ordering in (c) and (e) respectively. The spatial patterns of edge bursts on unit cells are illustrated as black shading in the cartoon insets. Error bars are standard deviations across 10 experiment runs. See Supplementary Tables S1 and S2 for Hamiltonian parameter values and superconducting quantum devices used. The experiments shown here extend Figure 5 of the main text and Supplementary Figure S4 which were with two interacting particles.

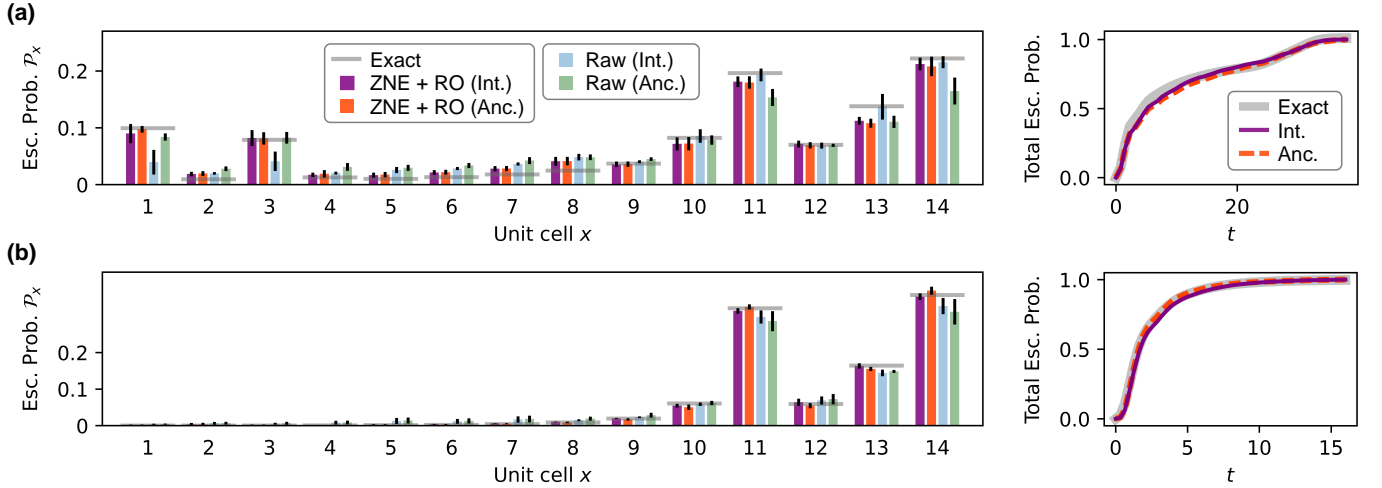
C. Alternative recovery of quantum state norm from algorithm success probability

To review, recall that time-evolution by a non-Hermitian Hamiltonian \mathcal{H} is non-unitary, and the norm of a quantum state is not generically preserved during time-evolution. That is, examining the physical time-evolved state $\omega_t = e^{-i\mathcal{H}t}\omega_0e^{+i\mathcal{H}^\dagger t}$ from an initial state ω_0 , generically $\text{tr}\omega_t \neq \text{tr}\omega_0 = 1$. As mentioned in the main text and [Methods](#), to realize time-evolution on a quantum platform in experiments, we perform normalized time-evolution, $\rho_t = \mathcal{N}[e^{-i\mathcal{H}t}\rho_0e^{+i\mathcal{H}^\dagger t}]$, where $\rho_0 = \omega_0$. The normalized state ρ_t is related to ω_t by a rescaling, $\omega_t = A_t^2\rho_t$. Accordingly, by measuring any observable O on the normalized time-evolved state ρ_t in the experiment, we can rescale the measurement results to be on ω_t , by the relation $\langle O \rangle_{\omega_t} = A_t^2 \langle O \rangle_{\rho_t}$.

The method employed to recover A_t in all our reported experiments is through a double time-integration of measured occupancy density $\langle n_{x\ell} \rangle_{\rho_t}$ data, as was described in detail in the main text and [Methods](#). But as described in [Methods](#), there is an alternative method available. Namely, the quantum simulation algorithm for normalized time-evolution succeeds precisely with a probability S_t directly related to the norm of the time-evolved quantum state. Provided $\text{tr}\omega_0 = \text{tr}\rho_0 = 1$ initially, $A_t^2 \approx S_t$ up to suppressible approximation errors in the time-evolution algorithm and circuit construction. Thus S_t measured in experiments allow recovery of A_t^2 , to then serve the same role in enabling estimation of observable expectation values $\langle O \rangle_{\omega_t}$.

In Supplementary Figure [S6a](#), we show a concrete comparison between the two methods. We examine the same experiment as in Figure [5c](#) of the main text, with two interacting particles on the quantum ladder producing a spatially extended edge burst with \mathbb{Z}_2 ordering. We report the cell-resolved final escape probabilities \mathcal{P}_x obtained via the observed success rate of the time-evolution algorithm (denoted ‘‘Anc.’’ in the figure), and for ease of comparison, include also \mathcal{P}_x obtained through the time-integration method (denoted ‘‘Int.’’) previously shown in Figure [5c](#). We show also a comparison of the total escape probability $P(t)$ summed over all unit cells, obtained through the success rate and time-integration methods. In Supplementary Figure [S6b](#) we present analogous data but in the trivial regime.

Our general observation in experiments is that both methods of recovering the quantum state norm give very similar results after error mitigation. Indeed here, in the example shown in Supplementary Figure [S6](#), the \mathcal{P}_x spatial profiles obtained from the two methods exhibit a quantitative match within error bars. The $P(t)$ time profiles are also similar; the small differences detectable in Supplementary Figure [S6](#) are largely inconsequential to the escape probabilities $P_x(t)$ and \mathcal{P}_x .



Supplementary Figure S6. **Example comparison between quantum state norm recovery methods.** (a) Final cell-resolved escape probabilities \mathcal{P}_x obtained on hardware with and without zero-noise extrapolation (ZNE) and readout error mitigation (RO), and exact numerics, shown on the left. Total escape probability $P(t)$ summed over all unit cells versus time t , shown on the right. (b) Analogous experiment data but in the trivial regime. Data denoted ‘‘Int.’’ were obtained via double time-integration of measured site-resolved occupancy densities for quantum state norm recovery, a method described in the main text and [Methods](#), and were previously shown in Figure [5c](#). Data denoted ‘‘Anc.’’ were obtained by inferring quantum state norm from algorithm success rate. Error bars are standard deviations across 10 experiment runs. See Supplementary Tables [S2](#) and [S3](#) for Hamiltonian parameter values and superconducting quantum devices used.

-
- [1] W.-T. Xue, Y.-M. Hu, F. Song, and Z. Wang, Non-Hermitian edge burst, *Phys. Rev. Lett.* **128**, 120401 (2022).
 - [2] P. Wen, J. Pi, and G.-L. Long, Investigation of a non-Hermitian edge burst with time-dependent perturbation theory, *Phys. Rev. A* **109**, 022236 (2024).
 - [3] S. Yao and Z. Wang, Edge states and topological invariants of non-Hermitian systems, *Phys. Rev. Lett.* **121**, 086803 (2018).
 - [4] M. A. Nielsen and I. L. Chuang, *Quantum computation and quantum information* (Cambridge university press, 2010).
 - [5] T. Itoko, R. Raymond, T. Imamichi, and A. Matsuo, Optimization of quantum circuit mapping using gate transformation and commutation, *Integration* **70**, 43 (2020).
 - [6] J. Welch, A. Bocharov, and K. M. Svore, Efficient approximation of diagonal unitaries over the Clifford+T basis (2015), [arXiv:1412.5608 \[quant-ph\]](https://arxiv.org/abs/1412.5608).
 - [7] M. Ezawa, Systematic construction of square-root topological insulators and superconductors, *Phys. Rev. Res.* **2**, 033397 (2020).
 - [8] A. M. Marques, L. Madail, and R. G. Dias, One-dimensional 2^n -root topological insulators and superconductors, *Phys. Rev. B* **103**, 235425 (2021).
 - [9] M. Kremer, I. Petrides, E. Meyer, M. Heinrich, O. Zilberberg, and A. Szameit, A square-root topological insulator with non-quantized indices realized with photonic Aharonov-Bohm cages, *Nat. Commun.* **11**, 907 (2020).
 - [10] H. Wu, G. Wei, Z. Liu, and J.-J. Xiao, Square-root topological state of coupled plasmonic nanoparticles in a decorated Su-Schrieffer-Heeger lattice, *Opt. Lett.* **46**, 4256 (2021).
 - [11] W. Deng, T. Chen, and X. Zhang, n th power root topological phases in Hermitian and non-Hermitian systems, *Phys. Rev. Res.* **4**, 033109 (2022).
 - [12] L. Song, H. Yang, Y. Cao, and P. Yan, Square-root higher-order Weyl semimetals, *Nat. Commun.* **13**, 5601 (2022).
 - [13] A. M. Marques and R. G. Dias, 2^n -root weak, chern, and higher-order topological insulators, and 2^n -root topological semimetals, *Phys. Rev. B* **104**, 165410 (2021).
 - [14] Z. Lin, S. Ke, X. Zhu, and X. Li, Square-root non-Bloch topological insulators in non-Hermitian ring resonators, *Opt. Express* **29**, 8462 (2021).
 - [15] S. Guo, G. Pan, J. Huang, R. Huang, F. Zhuang, S. Su, Z. Lin, W. Qiu, and Q. Kan, Realization of the square-root higher-order topology in decorated Su-Schrieffer-Heeger electric circuits, *Appl. Phys. Lett.* **123**, 043102 (2023).
 - [16] Z.-G. Geng, Y.-X. Shen, Z. Xiong, L. Duan, Z. Chen, and X.-F. Zhu, Quartic-root higher-order topological insulators on decorated three-dimensional sonic crystals, *APL Mater.* **12**, 021108 (2024).
 - [17] Y. Kim, A. Eddins, S. Anand, K. X. Wei, E. Van Den Berg, S. Rosenblatt, H. Nayfeh, Y. Wu, M. Zaletel, K. Temme, *et al.*, Evidence for the utility of quantum computing before fault tolerance, *Nature* **618**, 500 (2023).
 - [18] Y. Kim, C. J. Wood, T. J. Yoder, S. T. Merkel, J. M. Gambetta, K. Temme, and A. Kandala, Scalable error mitigation for noisy quantum circuits produces competitive expectation values, *Nat. Phys.* **19**, 752 (2023).
 - [19] R. Majumdar, P. Rivero, F. Metz, A. Hasan, and D. S. Wang, Best practices for quantum error mitigation with digital zero-noise extrapolation, in *2023 IEEE International Conference on Quantum Computing and Engineering (QCE)*, Vol. 1 (IEEE, 2023) pp. 881–887.
 - [20] T. Giurgica-Tiron, Y. Hindy, R. LaRose, A. Mari, and W. J. Zeng, Digital zero noise extrapolation for quantum error mitigation, in *2020 IEEE International Conference on Quantum Computing and Engineering (QCE)* (IEEE, 2020) pp. 306–316.
 - [21] K. Temme, S. Bravyi, and J. M. Gambetta, Error mitigation for short-depth quantum circuits, *Phys. Rev. Lett.* **119**, 180509 (2017).
 - [22] A. Hashim, R. K. Naik, A. Morvan, J.-L. Ville, B. Mitchell, J. M. Kreikebaum, M. Davis, E. Smith, C. Iancu, K. P. O’Brien, I. Hincks, J. J. Wallman, J. Emerson, and I. Siddiqi, Randomized compiling for scalable quantum computing on a noisy superconducting quantum processor, *Phys. Rev. X* **11**, 041039 (2021).
 - [23] J. J. Wallman and J. Emerson, Noise tailoring for scalable quantum computation via randomized compiling, *Phys. Rev. A* **94**, 052325 (2016).